COO-2888-3
NASA CR135419

Dist. Category UC-94a

MOLTEN SALT
THERMAL ENERGY STORAGE SYSTEMS

(NASA-CR-135419) MOLTEN SALT THERMAL ENERGY STORAGE SYSTEMS Final Report (Institute of Gas Technology) 129 p HC A07/MF A01 CSCL 10C
N78-24618
Unclas
G3/44 16812

Project 8981 Final Report

Hansraj C. Maru, John F. Dullea
Alan Kardas, and Larry Paul

Contributors
Leonard G. Marianowski
Estela Ong
Viji Sampath
Vincent M. Huang
Jerome C. Wolak

Prepared by
Institute of Gas Technology
IIT Center, 3424 S. State Street
Chicago, Illinois 60616

Date Published — March 1978

Prepared for the
UNITED STATES DEPARTMENT OF ENERGY
Under Contract No. EY-76-C-02-2888

COO-2888-3
NASA CR135419

Dist. Category UC-94a

MOLTEN SALT THERMAL ENERGY STORAGE SYSTEMS

Project 8981 Final Report

Hansraj C. Maru, John F. Dullea
Alan Kardas, and Larry Paul

Contributors
Leonard G. Marianowski
Estela Ong
Viji Sampath
Vincent M. Huang
Jerome C. Wolak

Prepared by
Institute of Gas Technology
IIT Center, 3424 S. State Street
Chicago, Illinois 60616

Date Published — March 1978

Prepared for the

UNITED STATES DEPARTMENT OF ENERGY

Under Contract No. EY-76-C-02-2888

TABLE OF CONTENTS

Page

ABSTRACT 1

SUMMARY 2

DETAILED DESCRIPTION OF TECHNICAL PROGRESS 4

Task 1. Salt Selection 4

Introduction 4

Selection Criteria 6

Thermal Properties 6

Physical Properties 7

Cost, Containment, Safety, and Stability 7

Eutectic Vs. Noneutectic Mixtures 8

Change in Melting Point as a Function of Composition 8

Compatibility With Volume-Change Additives and Conductivity Promoters 9

Candidate Salts 9

Task 2. Heat-Transfer Analysis and System Design 12

Introduction 12

Background and Past Work 14

Basic Equations in Phase-Change Heat Transfer 14

Transient Solutions 16

Periodic Solutions 19

Temperature Response of a Storage Unit 20

Experimental Verification of Simplifying Assumptions 22

The No-Thermal-Gradient Assumption: First Part of the Cooling Half-Cycle (Cooling the Liquid) 22

Use of an "Apparent" c_p: Second Part of the Cooling Half-Cycle (The Phase Change) 27

Third Part of the Cooling Half-Cycle (Cooling the Solid Phase) 27

TABLE OF CONTENTS, Cont.

Page

Design of the Engineering-Scale (8-kWhr$_{th}$) Experimental Storage Unit 27

Verification of Thermophysical Properties of $LiKCO_3$ 31

Investigation of Conductivity Enhancement and Volume-Change Control Additives 32

- Investigation of Conductivity-Promoter Additives 35
- Investigation of Volume-Change Control Additives 40

Construction Materials 46

- Corrosion Data 46
- Corrosion Mechanisms and Thermodynamics 49
- Experimental Observations 49

Task 3. Construct, Operate, and Evaluate the Performance of the Engineering-Scale (8-kWhr$_{th}$) System 52

System Construction 52

System Operation and Data Collection 52

Performance Evaluation 56

- Criteria for Performance Evaluation 56
- Evaluation of $LiKCO_3$ Without Conductivity Enhancement 57
  - Unit 1 Performance — Heat Flux and Efficiency 59
  - Unit 1 Stability and Cyclability 75
  - Unit 2 Performance — Heat Flux and Efficiency 77
  - Unit 2 Stability and Cyclability 83
- Evaluation of $LiKCO_3$ With a Finned Tube 86
  - Unit 3 Operation — Finned-Tube Heat Exchanger Design 86
  - Unit 3 Performance — Heat Flux and Efficiency 88
  - Unit 3 Stability and Cyclability 94

TABLE OF CONTENTS, Cont.

Page

Task 4. Compare Experimental Performance of Engineering-Scale System With Its Predicted Performance 98

Introduction 98

Solidification of LiKCO$_3$ Alone; Movement of the Solid-Liquid Interface During System Discharge 98

Use of the Heat-Transfer Model in Large-Scale System Design 105

Introduction 105

TES System for Steam Upgrading 106

Task 5. Summary, Conclusions, and Recommendations 112

Conclusions 112

Recommendations for Further Research 112

NOMENCLATURE 115

REFERENCES CITED 118

LIST OF FIGURES

Figure No.		Page
1	Thermal Storage System for Shaft Power Application	4
2	Work Efficiency Using Heat Available at Temperature T and Rejecting Heat at 100°F	5
3	Cost Vs. Volume for Storage of 10^6 Btu	11
4	Thermal Conductivity Vs. Heat Capacity for Chloride and Carbonate Salt Mixtures	13
5	Advance of the Freezing Front at $x = a$	16
6	Solidification of a Cylindrical Melt From Within	18
7	Schematic of Laboratory TES Setup	23
8	Dimensions and Thermocouple Locations in Laboratory TES Unit	24
9	Cooling Rates in a Laboratory TES Unit	25
10	Engineering-Scale Thermal Energy Storage Unit	29
11	DTA Traces of Mechanical and Fused Mixtures of $LiKCO_3$	33
12	DTA Traces of Thermally Cycled $LiKCO_3$	34
13	Effect of Thermal Conductivity Enhancers	39
14	Capacity Variation With Composition of $LiKCO_3$-$LiAlO_2$ Composite Storage Medium	42
15	Calculated Settling Rate of $LiAlO_2$ in Molten $LiKCO_3$ at 525°C	44
16	Observed Sedimentation of $LiAlO_2$ in Molten $LiKCO_3$ at 530°C	45
17	Metallograph of Type 304 SS in the Meniscus Region Exposed at 530°C for 1250 hours	50
18	Engineering-Scale Unit Mounted in Testing Station	53
19	Schematic Diagram of the Engineering-Scale Thermal Energy Storage System	54
20	Solidified Salt Surface of TES Container No. 1 After 10 Cycles	60

LIST OF FIGURES, Cont.

Figure No.		Page
21	Temperature Profile in the Salt at Half Depth During the First Cycle	61
22	Temperature Profile in the Salt at Half Depth During the Tenth Cycle	63
23	Temperature Profile in the Salt at Half Depth During the Twentieth Cycle	64
24	Schematic Energy Input Profile During Charging and Holding of an Engineering-Scale TES System	67
25	Heat Loss During a 24-hour Operating Period for Larger TES Units	69
26	Performance of Unit 1	71
27	Influence of Salt Thickness on Heat Flux	73
28	Operation at and Above Design Temperature	74
29	Unit 1 Stabilization	76
30	Performance Comparison Between Units 1 and 2; Air Temperatures Measured at A and A'	79
31	Effect of Undercharge on Heat Flux	81
32	Salt Response During Charging	84
33	Vertical Temperature Profile as a Function of Time at a Midradial Plane	85
34	Unit 2 Stability With Cycling	87
35	Finned-Tube Heat Exchanger Located in the Engineering-Scale TES Unit	88
36	Effect of Fins on Temperature at the Salt-Side Heat-Transfer Surface	89
37	Salt Temperature Profile at Half Depth During Discharging With a Finned-Tube Heat Exchanger	91
38	Salt Temperature Profile at Half Depth During Discharging; $LiKCO_3$ Alone	92
39	Effect of Fins on Solidification Rate	93

ORIGINAL PAGE IS
OF POOR QUALITY

LIST OF FIGURES, Cont.

Figure No.		Page
40	Effect of Fins on Heat Flux	95
41	Salt Response During Charging With Finned-Tube Heat Exchanger	96
42	Cycle Stability of Unit 3	97
43	Typical Temperature Response at Various Locations in the Engineering-Scale Units During Discharging	99
44	Comparison of Solidification Profiles	103
45	Megerlin Plots to Determine Solidified PCM Thickness	107
46	Graphic Solution for Number of Pipes and Their Length	110

LIST OF TABLES

Table No.		Page
1	Weight and Volume of Medium Required for Storage of 10^6 Btu Thermal Energy	6
2	Properties of Selected Salts	10
3	Properties of Materials Considered as Conductivity Promoters	36
4	Comparison of Heat-Transfer Rates to Cooling Air From $LiKCO_3$ With or Without Additives	37
5	Corrosion Rates Observed by Various Investigators	47
6	Representative Thermal Performance of TES Unit 1	65
7	Summary of Cooling Behavior at Locations 2, 3, and 7 During Run 1-20	70
8	"Apparent" Thermal Performance of TES Unit 2	78
9	Representative Thermal Performance of TES Unit 2	80
10	Representative Thermal Performance of TES Unit 3	90
11	Performance Changes Resulting From Engineering-Scale Operation With Heat-Transfer Enhancement	90
12	Interfacial Movement in Engineering-Scale Unit 2	100
13	Comparison of Theoretical and Observed Solidification Behavior	102
14	Comparison of Megerlin Solution and Physical Model	104
15	Design Parameters for Steam Upgrading, With $N_{ph} = 2$, $N_{Fo} = 15.9$, $r_o = 1.25$ in., and $\dot{m} = 5 \times 10^5$ lb/hr, Using $LiKCO_3$ as the PCM	109

CONVERSION FACTORS

Non-SI Unit	Operation	SI Unit
Btu	X 1055.06	J
Btu/lb	X 2326.00	J/kg
Btu/lb-°F	X 4186.80	J/kg-K
Btu/hr-ft-°F	X 1.731	W/m-K
Btu/hr-ft^2-°F	X 5.678	W/m^2-K
Btu/hr-ft^2	X 3.154	W/m^2
°C	+ 273.15	K
cP	X 0.001	Pa-s
°F	(5/9)(°F + 459.67)	K
ft	X 0.3048	m
ft^2	X 0.0929	m^2
ft^2/hr	X 0.0000258	m^2/s
ft^3	X 0.0283	m^3
in.	X 0.0254	m
in.^{2}	X 0.0006451	m^2
lb	X 0.4536	kg
lb/ft^3	X 16.018	kg/m^3
lbm/ft^2-s	X 4.883	kg/m^2-s
mil	X 0.0000254	m
psi	X 6894.8	Pa

ABSTRACT

The feasibility of storing thermal energy at temperatures of 450° to 535°C (850° to 1000°F) in the form of latent heat of fusion has been examined for over 30 inorganic salts and salt mixtures. Alkali carbonate mixtures are attractive as phase-change storage materials in this temperature range because of their relatively high storage capacity and thermal conductivity, moderate cost, low volumetric expansion upon melting, low corrosivity, and good chemical stability. An equimolar mixture of Li_2CO_3 and K_2CO_3, which melts at 505°C with a latent heat of 148 Btu/lb, was chosen for experimental study. The cyclic charge/discharge behavior of laboratory- and engineering-scale systems was determined and compared with predictions based on a mathematical heat-transfer model that was developed during this program. The thermal performance of one engineering-scale unit remained very stable during 1400 hours of cyclic operation. Several means of improving heat conduction through the solid salt were explored. Areas requiring further investigation have been identified.

SUMMARY

A research program directed toward evaluating and demonstrating the technical feasibility of a molten salt thermal energy storage system has been completed. This final report describes the work performed under these titles: Task 1 — Salt Selection, Task 2 — Heat-Transfer Analysis and System Design, Task 3 — Construction, Operation, and Performance Evaluation of Engineering-Scale Systems, Task 4 — Comparison of Experimental System Performance to Predicted Performance, and Task 5 — Summary, Conclusions, and Recommendations.

A total of [illegible]1 inorganic salts and salt mixtures, including nine alkali and alkaline earth carbonate mixtures, were evaluated for their suitability as heat-of-fusion thermal energy storage materials at temperatures of 450° to 535°C. Thermophysical properties, safety hazards, corrosion, and cost of these salts were compared on a common basis. Alkali carbonates were found to be attractive as heat-of-fusion storage materials in this temperature range because of their relatively high storage capacity and thermal conductivity, moderate cost, low volumetric expansion upon melting, low corrosivity, and good chemical stability. A 35 weight percent Li_2CO_3 – 65 weight percent K_2CO_3 mixture was selected as a model system for experimental work. This mixture forms an intermediate compound $LiKCO_3$, which melts congruently at 505°C with a heat of fusion of 148 Btu/lb.

A mathematical model was developed to evaluate the problem of heat transfer from a moving solid/liquid interface to an internal concentric heat-exchanger tube. This model was used to design laboratory- and engineering-scale storage units and to evaluate their thermal performance during cycling. The engineering-scale units were 1 foot in OD and 1.5 feet high with a 2-in.-diameter heat exchanger tube; the laboratory-scale units were 3 in. in OD and 5 inches high with a 0.5-in.-diameter internal tube.

Thermal performance of the engineering-scale systems was determined during charge/discharge cycles; high-velocity ambient air was the discharge working fluid. At the air flow rates investigated, the rate of discharge was limited by heat conduction through the growing layer of solid salt on the heat exchanger surface. Enhancement of heat conduction was accomplished by randomly dispersing metal wools in the carbonate salt phase and by adding metal fins to the heat exchanger. No significant losses of system performance, salt instabilities, or metallic corrosion were observed after 1400 hours of operation. The thermal

response of the experimental storage units agreed very well with the predictions of the heat-transfer model.

It is recommended that future investigations focus on the areas of optimization of salt composition, heat-transfer modeling studies, heat-conduction enhancement, long-term testing of larger units, and integrated systems design.

ORIGINAL PAGE IS
OF POOR QUALITY

DETAILED DESCRIPTION OF TECHNICAL PROGRESS

Task 1. Salt Selection

Introduction

Storage of thermal energy at temperatures above 315°C (600°F) may be desirable for a number of applications, such as —

a. Conventional base-load power plants

b. Solar Thermal Power Systems

c. Cyclic- or batch-type industrial processes

d. Vehicular propulsion using heat engines.

Generally shaft power from a thermal engine and/or thermal energy itself can be produced by heat exchange with the thermal-storage media (Figure 1).

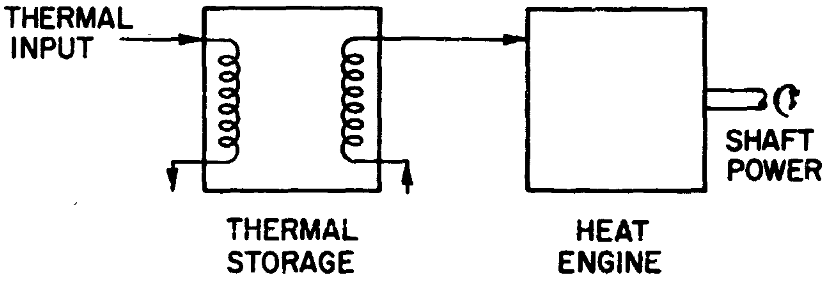

A76030596

Figure 1. THERMAL STORAGE SYSTEM FOR SHAFT POWER APPLICATION

Consideration of the temperature of the thermal input, thermal stability, compatability of the storage media with their means of containment and heat exchange, and of the desired end product (shaft power or thermal energy) generally sets the choice of storage temperature. For example, in the case in which the thermal input to the storage media comes from either application a or b above, a useful temperature range of the storage media is expected to be 450° to 535°C (850° to 1000°F). The production of shaft power is the highest quality use of such stored thermal energy; therefore, maximizing the storage capacity within a narrow temperature band in this range is thermodynamically desirable because thermal engine efficiency is a function of the temperature of the input energy (Figure 2). If the quality (temperature) of the thermal input to the heat engine is allowed to vary, costly enginegeneration control equipment would be required to maintain a constant power output from the plant and the overall plant efficiency would suffer. The temperature of the thermal input to the heat engine should remain constant to maximize its efficiency.

Table 1 shows some choices for thermal storage media in the 450° to 535°C (850° to 1000°F) temperature range. The higher storage capacity of a phase-change material (PCM) for which the latent heat provides the major share of the total capacity is readily seen. From the table we observe that large storage volume will be required if sensible heat is stored in high-pressure steam. A typical refractory material such as MgO will require 3 times the volume and 4 times the weight of a typical PCM.

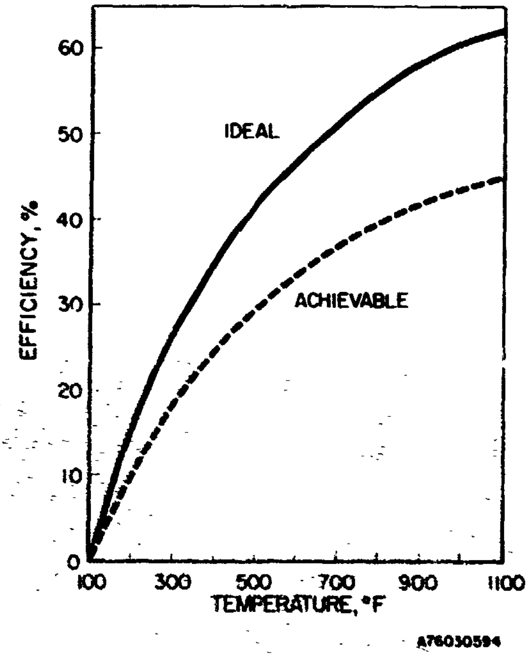

Figure 2. WORK EFFICIENCY USING HEAT AVAILABLE AT TEMPERATURE T AND REJECTING HEAT AT 100°F (Adapted From Hausz and Meyer[10])

Compared with the other media, molten carbonate salt PCM have the following potential advantages:

a. The melting points are in the desired temperature range (450° to 535°C). This means that the relatively high latent heats of melting >135 Btu/lb (>350 J/g) can be utilized, leading to compact system sizes, and that the heat is available at a constant temperature (at the melting point), thus providing good quality input into a thermal engine.

b. Their good thermal conductivities relative to other salts result in efficient heat transfer and thermal management.

c. Their low vapor pressures result in low-pressure design and potentially long usable lifetimes.

Table 1. WEIGHT AND VOLUME OF MEDIUM REQUIRED FOR STORAGE OF 10^6 Btu THERMAL ENERGY [Storage Medium Operating Between 450° and 535°C (850° and 1000°F)]

	Pressure	Weight, lb/10^6 Btu	Volume, $ft^3/10^6$ Btu
Molten Salts (Carbonates)	Atmospheric	7500	53
Steam	100 psia	850	7,000
MgO	Atmospheric	22,000	100

High-temperature, molten salt TES systems have received limited attention, and data on their heat transfer characteristics, cycle life, corrosion, and salt stability are lacking. The program at the Institute of Gas Technology (IGT) is directed at obtaining some of this information for carbonate salt mixtures suitable for use at temperatures ranging from 450° to 535°C (850° to 1000°F). The purpose of the salt selection task (Task 1) was twofold:

1. To identify promising salt systems by comparing thermophysical and cost characteristics of salt mixtures, which have a melting point between 450° and 535°C (850° and 1000°F).
2. To select a model salt system for initial experimental work. The methodology and data generated for this model system can then be easily extended to other systems.

Selection Criteria

Numerous salts and mixtures of salts can be considered for thermal energy storage in the 450° to 535°C (850° to 1000°F) temperature range. If cost, availability, stability, nontoxicity, and corrosiveness are the prime salt selection criteria, then the available choices are limited to chlorides, bromides, hydroxides, fluorides, and carbonates. In further comparing the inorganic salts, numerous other factors must also be considered.[2] These include the following characteristics.

Thermal Properties

The important thermal properties of storage materials include the heat of fusion, thermal conductivity, and heat capacity. These factors determine the suitability of a material for heat-of-fusion thermal energy storage on the basis of its storage capacity and heat-transfer characteristics. The heat of fusion determines the storage capacity of a material. The thermal conductivity of its liquid and solid phases will determine the charging and discharging rates obtainable, and will affect the complexity (and cost) of the heat-exchanger design. Materials with high heats of fusion and thermal conductivities will be desirable as they represent high-capacity systems that can be charged and discharged rapidly without the need for complex and costly heat-exchange systems. High heat capacities, although of secondary importance, are also desirable because they are indicative of storage capacity above the heat-of-fusion and reserve capabilities of the system.

Physical Properties

Storage-material physical properties of interest are density, volume change with temperature (volumetric expansion), volume change on fusion, viscosity of the liquid phase, and vapor pressure. Density and heat of fusion determine the energy storage density. Volumetric thermal expansion must be considered when designing the container to compensate for the storage-material volume change in heating from ambient to the operating temperature range. Most materials increase in volume upon fusion. If these volume changes are large, difficulties in containment may arise or voids may form in the storage material during solidification. This can have detrimental effects on the conducting properties, causing losses in efficiency, charging rates, and possibly capacity. Viscosity of the liquid phase near the melting temperature is important because of its effect on convective currents. These currents, brought about by temperature variations in the PCM, aid in heat transfer and in the homogenization of the storage material. The vapor pressure reflects the stability of the storage material and affects the design of the containment vessel as well as the losses that might result from a leak in the vessel. Ideally, the heat-of-fusion storage material will have a high energy density, little volumetric thermal expansion or volume change when fused, and low viscosity and vapor pressure in the working temperature range.

Cost, Containment, Safety, and Stability

The storage material cost, although only a small part of the overall system cost, must be considered because of its effect on the economic feasibility of a system. The toxicity and compatibility of the storage material with the heat-transfer medium must also be considered because possible system failures may release storage materials into surrounding areas or bring storage and heat-transfer materials into contact. Toxic fumes or violent chemical reactions resulting from such system failures can produce harmful effects on life and the environment. Containment of storage materials becomes a problem because of the possible corrosiveness of molten storage materials and the volume changes accompanying temperature changes and fusion. If any of these characteristics occur to a great extent, complex containment designs may be required. Storage materials that show little corrosive activity when used with low-cost containment materials are desirable to maximize the life of a storage system. Lifetimes of 20 to 30 years will be required if storage systems are to function economically in commercial systems. This lifetime requirement necessitates good stability of thermal and physical properties in a storage material.

Eutectic Vs. Noneutectic Mixtures

Noneutectic compositions melt incongruently, i.e., the solid forms a liquid and another solid of a different composition. This effect may be advantageous in that the second solid phase formed in the liquid could act as a nucleating agent during solidification of the liquid, preventing supercooling effects. However, because of different compositions, the solid and liquid will also have different densities; this may result in separation by settling of the solid, producing a wide composition variation throughout the storage medium. This problem could be alleviated by some type of agitation, but that would only lead to increased system costs. Eutectic compositions melt congruently, and consequently, this problem would not be encountered if one were used.

Change in Melting Point as a Function of Composition

A change in the melting temperature of a salt mixture as a function of its composition within the system is also of primary importance. Compositions within a storage-material system may vary as a result of corrosion reactions or selective vaporization losses. If the melting temperature increases sufficiently, fusion may not be obtainable with the heat source for which the storage system was designed to operate. In this case, storage capacity would be decreased significantly, and the system would actually be converted to a sensible-heat storage system.

Compatibility With Volume-Change Additives and Conductivity Promoters

Thermal conductivities and volume changes occurring during operation are important considerations in determining the practicality of using a salt as a PCM. Although these properties are characteristic of the salts, they may be modified in the storage system by the addition of inert materials to the salts. Because metals have relatively high thermal conductivities, the addition of metallic screens, wires, rods, or tubes to the salt could enhance its overall heat-transfer properties, although some of its capacity would be lost. The volume change that occurs when the total storage medium is fused may be controlled by the addition of a volume-change control additive to the salt. Compatibility of the PCM with such additives should also be considered when selecting the heat-of-fusion storage materials.

Candidate Salts

Mixtures of 31 candidate salts are presented in Table 2 with the experimental or estimated values of properties relevant to their applicability as heat-of-fusion TES materials. These salts were selected for consideration because their melting points fall in or near the 450° to 535°C (850° to 1000°F) range and they do not display any particular difficulties in handling, containment, stability, or availability. Some salts that can be used for thermal energy storage at temperatures either well below or above the range of primary interest have also been included for comparative purposes. The materials under consideration include single salts and binary and ternary salt mixtures of both eutectic and noneutectic compositions. Quaternary systems were not investigated due to the lack of pertinent thermal behavior data and suitable procedures for estimating the properties needed for evaluation.

Cost ($\$/10^6$ Btu) as a function of volume ($ft^3/10^6$ Btu) of the salts presented in Table 2 is shown graphically in Figure 3. The practicality of using very high-capacity, high-cost salts for large-scale applications is questionable because of the importance of salt cost in determining the degree to which a TES system can be economically competitive with alternative energy storage systems. The highest cost salts are composed of bromides, fluorides, hydroxides, or some chlorides (mixtures 1, 2, 15, 18, 21, and 25). The lowest cost salts are composed entirely of mixtures of alkali and alkaline earth chloride salts (mixtures 6 through 9, 19, 20, 22, and 23), whereas moderate-to-high cost salts are composed of carbonate salt mixtures (nos. 11 through 14, 24, 28, 29, and 30), mixtures of carbonates, and some chloride and fluoride

ORIGINAL PAGE IS OF POOR QUALITY

Table 2. PROPERTIES OF SELECTED SALTS[a]

Mixture No.	Salt[b]	Melting Point, °F	ΔH_f, Btu/lb	Heat Capacity at Melting Point C_p (s)	Heat Capacity at Melting Point C_p (l)	Thermal Conductivity at Melting Point k (s)	Thermal Conductivity at Melting Point k (l)	Viscosity, cP At Melting Point	Viscosity, cP Melting Point + 50°F	Density at 25°C, lb/ft³	Volume Change On Fusion at m.p., %	Safety Hazard[d] Inhalation	Containment Material	Salt Cost $/lb	Capacity Cost $/10⁶ Btu	Specific Capacity[h] (Based on ΔH_f), Btu/ft³	Comments	Composition
				Btu/lb-°F		Btu/hr-ft-°F												
1	LiOH	864	376	0.59	0.94					91.1		2	Mild Steel[g]	1.37	5,260	34,255		1
2	LiBr	1017	88	0.26	0.19		0.83	1.8	1.7	216.0		2[e]	SS	3.00	34,090	19,010		2
3	NaOH	606	69	0.48	0.51		0.53	4.3	4.0	133.0		2[f]	Mild Steel[g]	0.12	1,740	9,177	Comstock Wescott System[1,9]	3
4	B₂O₃	842	142	0.41	0.44	0.90	0.58			115.5		1	SS	0.16	1,140	16,400		4
5	58KCl-42ZnCl₂	810	44	0.16	0.21		0.48	4.5	2.8	150.5	17.4[c]	2[e]	SS	0.27	2,070	6,650		5
6	61KCl-39MgCl₂	815	156	0.19	0.23		0.47			131.7	21.4[c]	2[e]	SS	0.06	395	20,840		6
7	48NaCl-52MgCl₂	842	185	0.22	0.24		0.55			135.1	23.6[c]	2	SS	0.08	430	25,115		7
8	36KCl-64MgCl₂	878	167	0.20	0.23		0.48			137.3	26.2[c]	2[e]	SS	0.09	540	22,910		8
9	33NaCl-67CaCl₂	932	121	0.20	0.24		0.59	[illegible]	1.1	134.8	14.5[c]	1	SS	0.03	250	16,310		9
10	37MgCl₂-63SrCl₂	995	103	0.16	0.19		0.61			173.6	16.3[c]	2	SS	0.33	3,205	17,880		10
11	47Li₂CO₃-53K₂CO₃	910	147	0.26	0.32		1.15	21	17	137.3	9.5	2	SS	0.47	3,200	20,185		11
12	44Li₂CO₃-56Na₂CO₃	925	159	0.43	0.50		1.21	25	16	148.8	11.5	2	SS	0.35	2,201	23,125		12
13	28Li₂CO₃-72K₂CO₃	928	113	0.38	0.43		1.17	1	15	143.8	[illegible]	2	SS	0.36	3,185	16,801		13
14	51K₂CO₃-49Na₂CO₃	1310	70	0.40	0.37		1.0[illegible]	5.4	4.2	143.9		2	Protected [illegible]	0.11	1,570	10,465		14
15	33LiF-67KF	918	266	0.32	0.39	2.4-4.8	2.10			157.3		1[e]	[illegible][g]	1.21	4,550	42,000		15
16	67NaF-33MgF₂	1530	265	0.34	0.33	2.4-4.8	0.65			155.1	22.4	1[e]	[illegible]	0.57	2,150	55,405	Philips System[11,1?]	16
17	45NaBr-55MgBr	800	91	0.12	0.14		0.52			217.9		2[e]	[illegible]	1.62	17,400	19,813		17
18	20LiF-80LiOH	799	374	0.21	0.24					91.3		1	[illegible]	2.04	5,515	37,165		18
19	25KCl-27CaCl₂-48MgCl₂	909	167	0.19	0.22		0.41			157.4	20.5[c]	2[e]	SS	0.08	515	26,210		19
20	5KCl-29NaCl-66CaCl₂	939	120	0.20	0.24		0.58	1.7	1.5	134.2	12.2[c]	2[e]	SS	0.03	250	16,105		20
21	13KCl-19NaCl-68SrCl₂	939	96	0.16	0.20		0.61	1.98	22	171.7	12.1[c]	2[e]	SS	1.37	14,270	16,485		21
22	28KCl-19NaCl-53BaCl₂	1009	95	0.15	0.19		0.50	[illegible]	71	180.7		2[e]	SS	0.03	315	17,175		22
23	24KCl-47BaCl₂-29CaCl₂	1024	94	0.15	0.20		0.55	[illegible]	[illegible]	182		2[e]	S	0.03	300	17,197		23
24	32Li₂CO₃-35K₂CO₃-33Na₂CO₃	747	119	0.40	0.39		1.17	171	[illegible]	143.1		2	SS	0.51	4,285	17,035		24
25	12NaF-59KF-29LiF	849	257	0.32	0.38	2.4-4.8	2.60			158.3		1[e]	[illegible]	1.11	4,320	40,580		25
26	60KCl-23KF-17K₂CO₃	982	122	0.24	0.30		0.69			142.5		1[e]	SS	0.23	1,885	17,385		26
27	17NaF-21KCl-62K₂CO₃	968	118	0.28	0.33		0.87			148.9		1[e]	SS	0.18	1,525	17,570		27
28	35Li₂CO₃-65K₂CO₃	941	148	0.32	0.42		1.09	18	15	141.5	9.6	2	SS	0.40	2,705	20,940	Eutectoid	28
29	30Li₂CO₃-40Na₂CO₃-29K₂CO₃	1022	132	0.38	0.45		1.09	4.1	1.7	148.6		2	SS	0.21	1,740	19,110	Non-Eutectic	29
30	22Li₂CO₃-16Na₂CO₃-62K₂CO₃	1022	124	0.41	0.50		1.13	3.2	1.5	146.3		2	SS	0.30	2,420	18,140	Non-Eutectic	30
31	68K₂CO₃-32MgCO₃	860	--					--		--	--				--		Phase diagram determined at high pressure only.	31

[a] Values underscored are experimental. Other values are estimates

[b] Mixture composition on weight basis

[c] Estimated from experimental values of single salts

[d] Toxic hazard rating code, 0: None, 1: slight, 2: moderate, 3: high, U: unknown

[e] When strongly heated, they emit highly toxic fumes

[f] Will react with water or steam to produce heat and will attack living tissue

[g] Suggested material if suitable corrosion inhibitors are used

[h] Based on ΔH_f value only

B77061345

ORIGINAL PAGE IS
OF POOR QUALITY

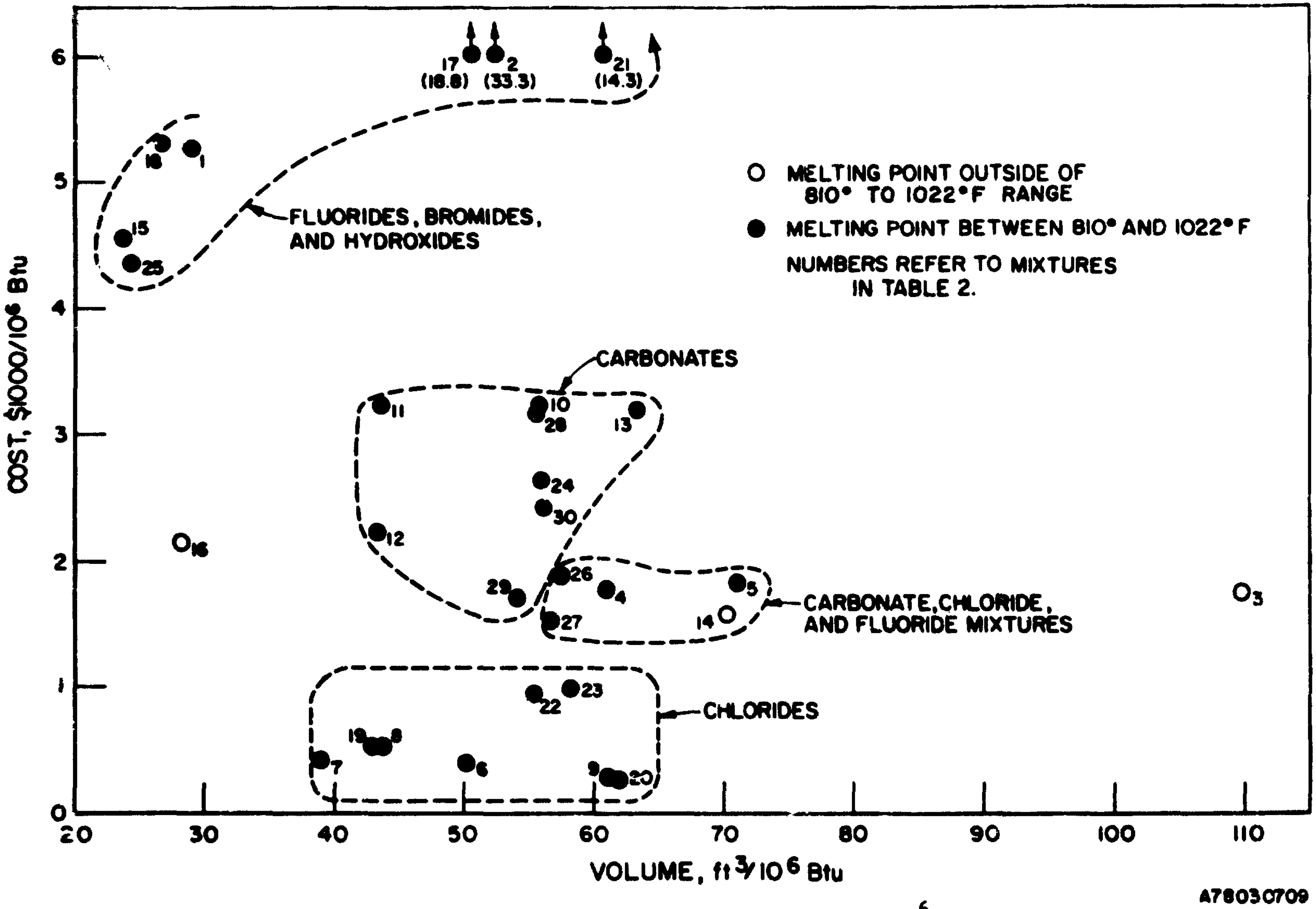

Figure 3. COST VS. VOLUME FOR STORAGE OF 10^6 Btu

salts (mixtures 5, 10, 26, and 27). Several of these low-to-moderate cost salts emit highly toxic fumes when heated (mixtures 5, 6, 8, 19, 20, 22, 23, 26, and 27), presenting potential safety hazards that would restrict their use and increase the cost of containment to prevent leakage.

The heat capacity of the solid phase, reflective of sensible-heat storage capacity, and the thermal conductivity of the liquid phase, indicative of heat transfer rates, are plotted in Figure 4 for chloride and carbonate salt compositions. Carbonate salt mixtures are superior to chlorides in both of these properties by a factor of 2 in each case.

Mixtures of lithium, potassium, and sodium carbonates or of sodium, calcium, and magnesium chlorides are the most practical salts for use as PCM. However, the thermal properties of mixtures of carbonate salts, particularly their superior thermal conductivities compared with those of other salts and their smaller volume changes on fusion, make them best suited as model storage materials in the 450° to 535°C (850° to 1000°F) range. Mixture 28, a 35 weight percent Li_2CO_3-65 weight percent K_2CO_3 (50 mole percent Li_2CO_3-50 mole percent K_2CO_3) mixture, was selected as a model system for experimental work. This is a congruently melting mixture having a heat of fusion of 148 Btu/lb (345 J/g), that forms an intermediate compound, $LiKCO_3$. Because experimental values of the thermophysical properties of the Li_2CO_3-K_2CO_3 mixture are well-characterized (compared with, for example, mixtures 12 and 29, which are less expensive) and because the change in melting point as a function of composition is very small, this mixture is ideally suited as a model system. This mixture will, therefore, be used to define heat-transfer characteristics and potential problems and also to provide the first-cut engineering data required for large-scale system design.

Task 2. Heat-Transfer Analysis and System Design

Introduction

Heat-transfer analysis of TES systems using PCM is necessary to determine the interrelationships among the various factors affecting energy storage, to estimate the relative magnitudes of various heat-transfer resistances and the overall heat-transfer flux, and to develop the mathematics and methodology required to aid in the design of phase-change TES systems. After such an analysis is developed and is proven workable in the laboratory, accurate design and cost estimates can be made to determine the feasibility of storing thermal energy in PCM.

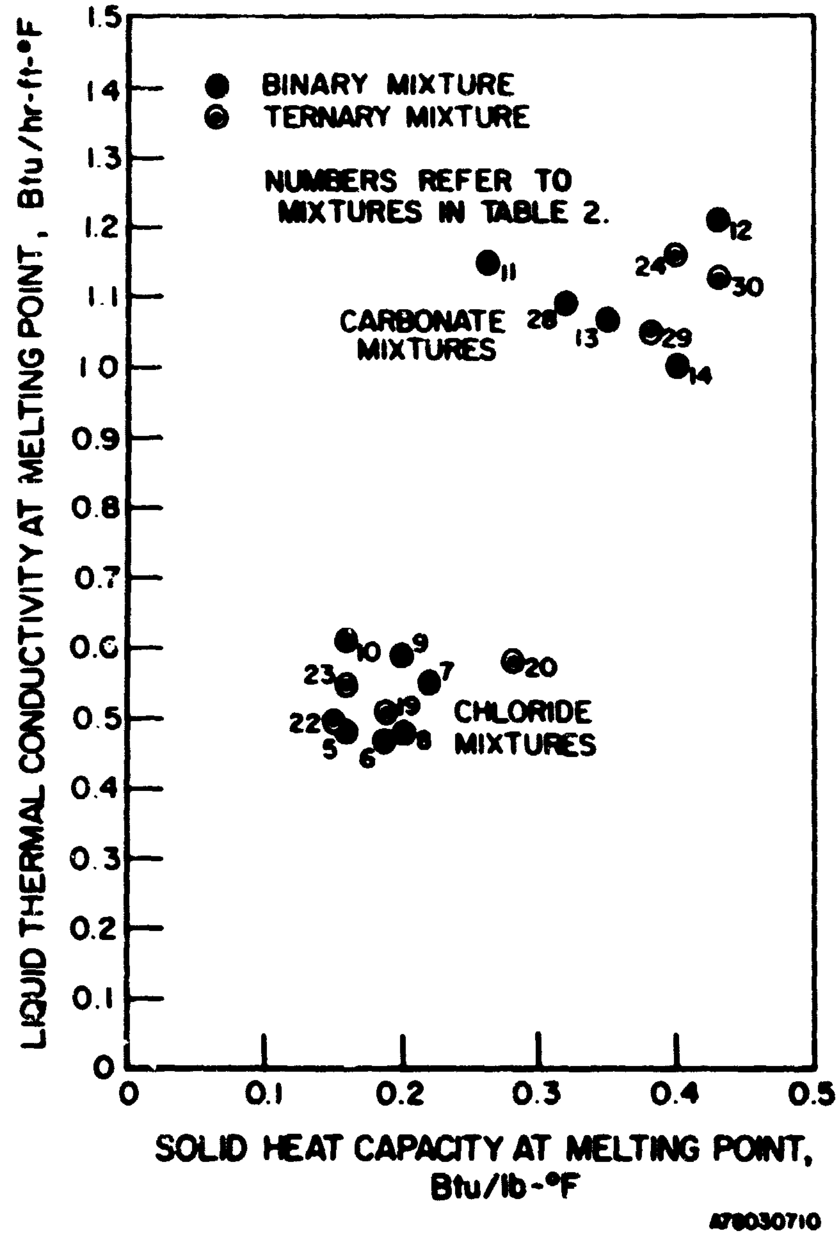

Figure 4. THERMAL CONDUCTIVITY VS. HEAT CAPACITY FOR CHLORIDE AND CARBONATE SALT MIXTURES

A heat-transfer analysis of a PCM storage system presents two major complexities. First, heat is stored in a PCM in both its latent and sensible forms, and the solid-liquid interface moves during the transfer of heat. Secondly, because of the regenerative nature of the storage system, a cyclic solution has to be considered. Due to these complexities, only a limited number of approximate solutions have been obtained in the past. We have used these solutions, with suitable modifications, to develop a heat-transfer model. In the following sections, we will discuss a) the background and a brief review of past work, b) observed interrelationships among variables of interest, c) experimental verification of some approximations, and d) the design of an experimental unit using the approximate solutions and the heat-transfer model developed from them.

Background and Past Work

Basic Equations in Phase-Change Heat Transfer

A regenerative heat-storage and retrieval system is comprised of a finite mass of storage material and possibly two working fluids. One of these fluids supplies some of its heat content to storage, and the other fluid transfers the stored thermal energy from the TES system. In our case, the storage material undergoes a phase change, so that both the liquid and solid phases are present in the unit and the solid-liquid interface moves during heat transfer. Because the heat capacities and conductivities of the two phases are different and the boundary between the two phases is not fixed in space, the mathematical analysis of heat transfer requires simultaneous consideration of both phases with an appropriate boundary condition. Thus, heat flow in the solid phase follows Fourier's law of heat conduction -

$$\frac{1}{\alpha_s} \frac{\partial t_s}{\partial \tau} = \text{div grad } t_s \qquad (1)$$

In the absence of convective currents, heat flow in the liquid phase can be described by -

$$\frac{1}{\alpha_\ell} \frac{\partial t_\ell}{\partial \tau} = \text{div grad } t_\ell \qquad (2)$$

At the moving interface, the heat is absorbed or released in the form of latent heat of fusion, so that -

$$k_s \text{ grad } t_s - k_\ell \text{ grad } t_\ell = \rho \Delta H_f \frac{\partial X}{\partial \tau} \qquad (3)$$

and

$$t_s = t_i = t_m \qquad (4)$$

The heat transferred to the working fluid is given by —

$$(c_p)_f \, \rho_f \, \frac{Dt_f}{D\tau} = -U\left(\frac{A}{V}\right) (t_f - t_w) \qquad (5)$$

which is coupled by the relation —

$$k \text{ grad } t = U \, (t_w - t_f) \qquad (6)$$

at the wall of the heat-transfer conduit. Solutions of the system of Equations 1, 2, and 6 exist only for a few selected geometries, with additional simplifications introduced to make the solution process tractable.

Additional complexities are involved because of the periodic nature of the storage-retrieval cycle. If the same fluid is used in the heating and cooling half-cycles, the inlet temperature, $t_{f,\,in}$, can be represented by a periodic function, such as —

$$t_{f,\,in} = 1/2 \, [t_{hot} + t_{cold} + (t_{hot} - t_{cold}) \cos \omega\tau] \qquad (7)$$

where —

t_{hot} = maximum temperature of the hot stream

t_{cold} = minimum temperature of the cold stream

ω = frequency.

For a more general case, a Fourier series summing the individual harmonics of Equation 7 can be used to construct the actual temperature variation in $t_{f,\,in}$.

The available analytical solutions can be classified in two categories: 1) transient (noncyclic) solutions that assume an initially uniform temperature profile and 2) cyclic solutions that account for the regenerative nature of the storage system.

The transient solutions are useful for experimental studies because a) the heat-transfer coefficients can be determined or verified by recording the time-dependent temperature behavior of the working fluids and b) heating the energy-storage materials past the phase change into the liquid phase results in starting the solidification half-cycles at approximately uniform temperatures. We have found experimentally, and the hydrodynamic stability theory also suggests, that a temperature gradient in the liquid phase of the reference salt cannot be maintained in a layer that is more than a fraction of an inch thick. This means that the solidification half-cycle can be studied analytically using transient solutions for several geometrical configurations.

Periodic solutions are important for storage system design, but solutions involving phase changes are unknown in the literature. Useful information can be obtained, however, using the available solutions for regenerative heat transfer in sensible-heat storage materials.

Transient Solutions

An approximate solution to two-phase heat transfer can be obtained if sensible heat is assumed to be negligible compared with latent heat and if perfect contact is assumed between the coolant and the solid storage material. For a flat-plate geometry (Figure 5), approximating grad t by $(t_a - t_m)/a$, we have –

$$\rho \Delta H_f \, v d\tau = \rho \Delta H_f \, da = k(t_m - t_a) \, \delta\tau / a \tag{8}$$

and, upon integrating –

$$0.5 \, a^2 = \frac{k\tau(t_m - t_a)}{\rho \Delta H_f} \tag{9}$$

or in dimensionless form –

$$N_{Fo} = 0.5 \, N_{ph} \tag{10}$$

where –

N_{Fo} = Fourier number = $\frac{k}{c_p \rho} \frac{\tau}{a^2}$

N_{ph} = phase-change number = $\frac{\Delta H_f}{c_p(t_m - t_a)}$

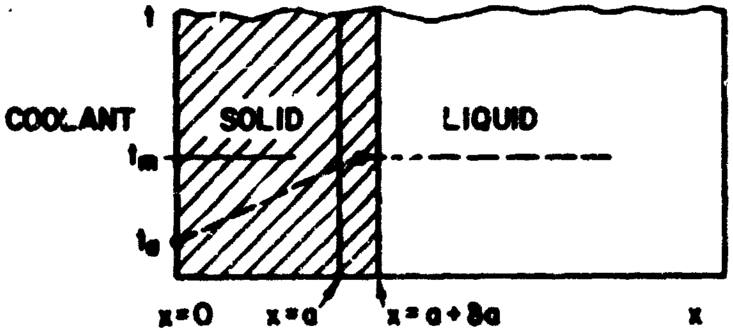

A77020498

Figure 5. ADVANCE OF THE FREEZING FRONT AT x = a

In a hollow cylinder with $R = r/r_o$, where r_o is the radius of the cooling tube, a similar analysis leads to —

$$N_{Fo} = 0.5\, N_{ph} \left(R^2 \ln R + \frac{1 - R^2}{2}\right) \quad (11)$$

$R \leq 1$ in cooling from outside; $R \geq 1$ in cooling from inside. Bramlette et al.[2] used these approximate solutions to compare heat fluxes among different containment configurations and inferred that an annular arrangement (working fluid inside) would provide the best heat fluxes. The assumptions involved in the heat balance, namely $c_p \to 0$ and $U \to \infty$ are not general. A check against a solution (to be discussed below) that does not resort to these assumptions showed that N_{Fo}, as calculated from Equation 11, was off by a factor of 2 to 3 for values of N_{ph} between 0.5 and 10, using $N_{Bi} = Ur_o/k_s = 1$. We do not recommend using these approximations in designing the storage unit.

An analytical solution for finite heat capacity, c_p, and ΔH with a flat-plate geometry was presented by Neumann,[4] who assumed that a) the PCM was initially at the melting point, t_m, b) there was no temperature gradient in the liquid phase; and c) the surface at $x = 0$ was subsequently held at $t_a < t_m$. A more realistic model must include a finite heat-transfer coefficient, h, at the boundary and conductance, k, across the wall; that is, $U = \left(\frac{1}{h} + \frac{d}{k}\right)^{-1}$. No assumptions should be made on the nature of the temperature profile in the solid phase; i.e., a finite sensible heat of the solid phase should be included. Such an analysis was performed by Megerlin.[22] In his solution, the time-dependent trial functions appear as coefficients in a power series expansion of the depth coordinate.

Equation 12 gives the dimensionless time needed to solidify the molten material from $r^* = 1$ to $r^* = R$:

$$N_{Fo} = \int_1^R \frac{r^* \ln r^* (N_{Bi} \ln r^* + 2)\, dr^*}{\sqrt{(N_{Bi} \ln r^* + 1)^2 + 2\frac{N_{Bi}}{N_{ph}} \ln r^* (N_{Bi} \ln r^* + 2)} - (N_{Bi} \ln r^* + 1)} \quad (12)$$

Solved for the solidified layer thickness R, which is measured in terms of the internal radius r_o, Equation 12 yields the thickness of the solid-phase layer as a function of time. Two illustrative results obtained by numerical evaluation of the integral in Equation 12 are shown in Figure 6. The family of curves with phase number $N_{ph} = 0.57$ describes the solid-layer thickness of

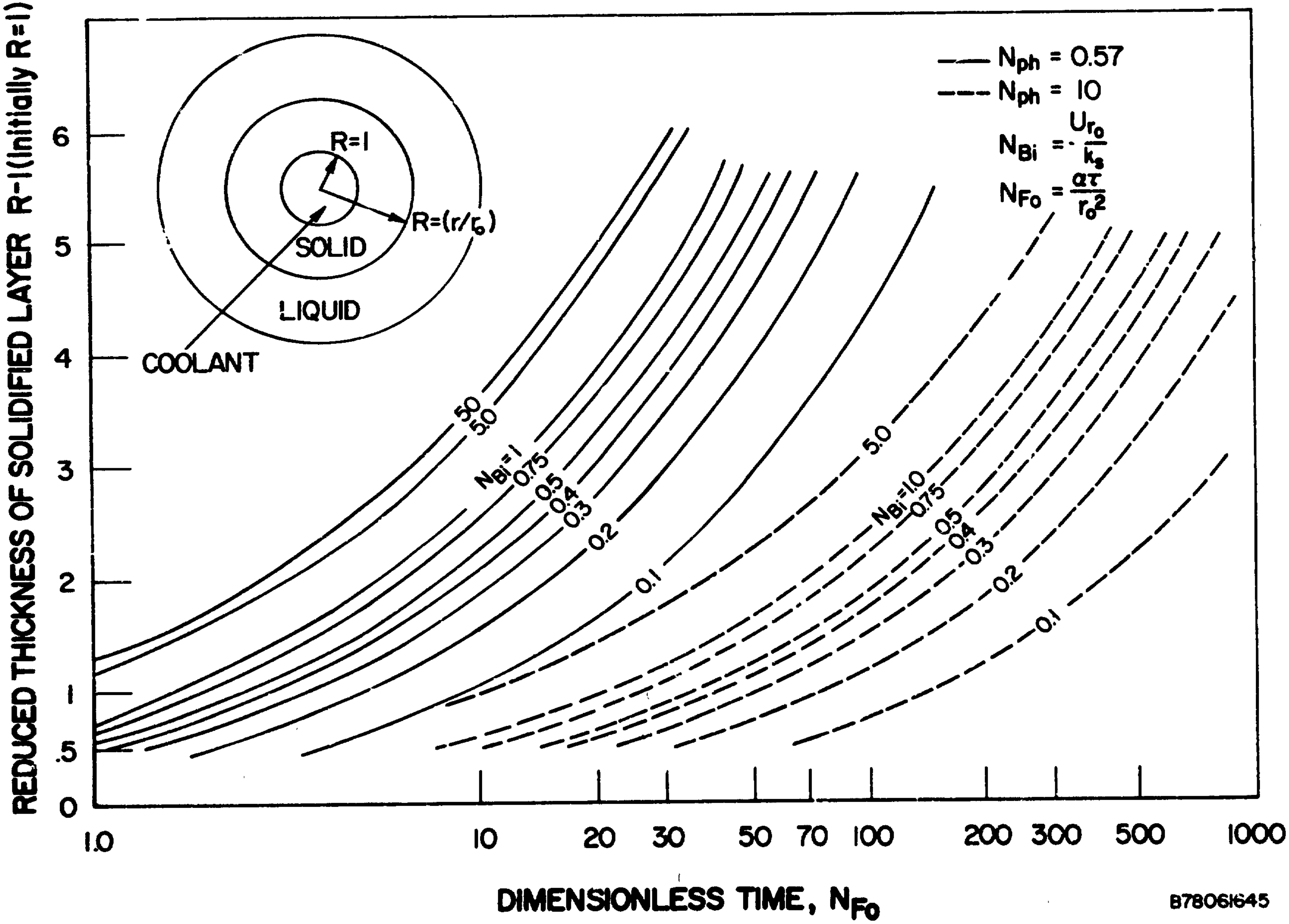

Figure 6. SOLIDIFICATION OF A CYLINDRICAL MELT FROM WITHIN

the reference material cooled with room-temperature air.† Phase-change number N_{ph} = 10 refers to the same material, except that the coolant runs about 25°C colder than the melting temperature of the salt.

These curves can be used to calculate various parameters, such as time required to solidify a given core of PCM, effect of heat-transfer coefficient, coolant temperature, and conductivity promoters. For example, if the coolant air is only approximately 25°C cooler than the melting point of the PCM (N_{ph} = 10), the time required for solidifying a given layer of salt would be approximately 10 times longer than that required if room-temperature air were used (N_{ph} = 0.57). On the other hand if time is kept fixed at N_{Fo} = 10 for example, the thickness of the layer r* should be reduced by half. Similarly, the effect of the relative resistance of heat transfer on the heat-transfer-fluid side and the storage-medium side can be determined by observing the effect of the Biot number ($N_{Bi} = Ur_o/k_s$) on the thickness of the solidified layer. As can be observed from Figure 6 for N_{ph} = 10 and a fixed thickness of a given PCM, an increase in N_{Bi} from 0.5 to 5 results in a twofold decrease in the time required, τ. This suggests that the heat-transfer resistance in the solid storage material is limiting for $N_{Bi} > 5$. For $N_{Bi} \cong 0.5$ (the value expected in our engineering-scale unit), the heat-transfer resistance in the PCM still appears to be the major factor, although the contribution of heat transfer on the heat-transfer-medium side is also significant. If the conductivity, k, of the PCM is doubled, that is, if N_{Bi} = 0.25, the value of τ required to solidify a layer of R = 6 decreases to 75% of the original value.

Periodic Solutions

As mentioned earlier, no periodic solutions are available for phase-change heat transfer. Therefore, we can consider a simple periodic solution

---

†For illustrative purposes, we used properties of the salt system $LiKCO_3$ selected for our experimental work. Relevant thermophysical properties of this system are:[8] —

Melting point: 505°C

Heat of Fusion (ΔH_f): 148 Btu/lb

Heat capacity at melting point: $(c_p)_s$ = 0.32 Btu/lb-°F
$(c_p)_\ell$ = 0.42 Btu/lb-°F

Thermal conductivity at melting point: k_s = 1.30 Btu/hr-°F-ft
k_ℓ = 1.09 Btu/hr-°F-ft

Viscosity at melting point plus 25°C: μ = 15 cP

Density at 298°K: ρ = 141.5 lb/ft³

Density at melting point: ρ_ℓ = 125.5 lb/ft³

ORIGINAL PAGE IS OF POOR QUALITY

for a flat-plate, sensible-heat system, and then introduce a concept of "apparent sensible heat" to account for latent heat and sensible heat simultaneously.

For flat-plate geometry, Equation 1 can be written as —

$$\frac{\partial t}{\partial \tau} = \alpha \frac{\partial^2 t}{\partial x^2} \qquad (13)$$

For a cyclic variation in the working-fluid temperature, the temperature in the PCM is given as —

$$t(x, \tau) = A_o \exp [-x(1 + i) K] \exp (i\omega\tau) \qquad (14)$$

The thermal diffusivity $\alpha = k/c_p\rho$ can be modified by assuming the apparent c_p of a fictitious solid, which can be obtained as follows:

Heat released per unit mass, Q, by a PCM between temperatures t_m and t_a, having a heat capacity $(c_p)_s$, and latent heat ΔH_f, is given as —

$$Q = (c_p)_s (t_m - t_a) + \Delta H_f \qquad (15)$$

and for the fictitious solid with heat capacity $(c_p)_{app}$, Q is given as —

$$Q = (c_p)_{app} (t_m - t_a) \qquad (16)$$

From these two equations —

$$(c_p)_{app} = (c_p)_s \left[1 + \frac{\Delta H_f}{(c_p)_s (t_m - t_a)} \right] \qquad (17)$$

or, in terms of N_{ph} —

$$(c_p)_{app} = (c_p)_s (1 + N_{ph}) \qquad (18)$$

Note that the value of $(c_p)_{app}$ is dependent on $\Delta t = t_m - t_a$ and is not purely a property of the PCM. Also, because during cooldown the entire mass of PCM does not attain temperature t_a, either an average temperature or the temperature of the working fluid can be used. When $N_{ph} >> 1$ —

$$(c_p)_{app} \approx (c_p)_s \cdot N_{ph} = \frac{\Delta H_f}{t_m - t_a} \qquad (19)$$

Temperature Response of a Storage Unit

To estimate the temperature response of a storage unit undergoing cyclic operation, we used the periodic solution of Equation 14. The following values are calculated for our storage system:

$(c_p)_{app}$ = 0.60 Btu/lb-°F (assumed; based on comparison with Neumann's solution)

τ_o = total period = 24 hours for a daily cycle

α_{app} = 0.0153 ft^2/hr

K = 3 ft^{-1}

λ = 2.1 ft

Phase velocity = $\lambda\upsilon$ = 0.0875 ft/hr = 1 in./hr

This means that, in terms of order of magnitude only, the designer of a periodic energy storage system (daily cycle) utilizing $LiKCO_3$ as a storage material and operating between the melting point (505°C) and ambient temperature (22°C) should think in terms of 2-foot-long temperature waves penetrating the material with the speed of about 1 in./hr. Note, however, that for any harmonic oscillation (for example, a sine-wave input), the amplitude of the incoming wave will be damped by exp (-2π) = 0.0019 over a single wavelength. With such damping, choosing the thickness of the material as great as a whole wavelength would appear to represent underutilization and therefore waste. Thus, we would like to determine an optimum thickness or distance between the heat-exchange surfaces.

In working with a slab of finite thickness 2a, it is convenient to define a dimensionless frequency M —

$$M = \sqrt{\frac{\pi a^2}{\alpha \tau_o}} \tag{20}$$

M can also be expressed in terms of a Fourier number based on the slab half-thickness, a, and the total period τ_o —

$$N^\circ_{Fo} = \frac{\alpha \tau}{r_o^2} \tag{21}$$

Therefore, $M = \sqrt{\frac{\pi}{N^\circ_{Fo}}}$. (22)

The temperature response of a slab to a cyclic heat input is usually expressed in terms of the parameter M. The relevant solutions are available in literature, but their numerical evaluation is laborious[4,16]. Relevant solutions for the temperature response of a storage medium under periodic variation in a heat-transfer fluid are presented elsewhere,[20] but an interesting observation can be made regarding the optimum thickness for maximum storage. Although very little heat can be stored in a thin slab ("a" or M small for a fixed period, τ_o), a semi-infinite body with its surface temperature varying harmonically can store, at most, $2/\pi$ (or 0.798) of the maximum. Groeber[8] observed that the heat stored during a half-cycle goes through a maximum of 0.911 at $M = 1.2$ and decreases for $M > 1.2$ until the limit of 0.798 is reached for practically all values of $M > 3$. This suggests that, in the absence of other overriding considerations, the designer of a storage device with a flat-plate matrix might start at $M = 1.2$. However, tradeoffs between various competing parameters and economics should be considered.

Experimental Verification of Simplifying Assumptions

A 5-in.-tall, 3-in.-diam laboratory model with a 1/2-in.-OD interior well was used to study solidification half-cycles with the model salt. For exact dimensions, constructions details, and thermocouple placement, see Figures 7 and 8. This study confirmed two assumptions developed and used in the analytical treatment of the heat storage problem with a phase change: 1) Assume that there is no thermal gradient in the liquid phase, so that in a cyclic operation the solidification half-cycle always begins with a uniform temperature distribution, permitting the use of transient ("single blow") solutions, and 2) use an "apparent" c_p for system design. Both assumptions appear to be confirmed by the test results shown in Figure 9.

The No-Thermal-Gradient Assumption: First Part of the Cooling Half-Cycle (Cooling the Liquid)

The model system ($LiKCO_3$) was heated to about 50°C above the melting point. Cooling begins with the liquid phase uniformly at 550°C. The cooling was provided by 22°C air passing through the 0.43-in.-ID internal well at 50 ft/s. Use of the Dittus-Boelter equation[17] for turbulent forced convection inside tubes in the form

$$h = 0.20\ (125)\ G^{0.8}\ (0.43/12)^{-0.2} \tag{23}$$

where G is the mass velocity, $G = \rho v = 0.0742\ (50) = 3.71\ \text{lbm/ft}^2\text{-s}$, and constant 125 is a temperature-dependent factor involving air conductivity and viscosity $(k/\mu^{0.8})$, gives a value for the heat-transfer coefficient of 13.9 $\text{Btu/hr-ft}^2\text{-°F}$. Several trial-and-error calculations of the exit air temperatures based on the relationship between the increase of the enthalpy of air and the heat transferred from the hot charge along the interior well length z,

$$c_p \dot{m} \frac{dt}{dz} = hp\ (\bar{t}_w - t) \tag{24}$$

or, integrated,

$$\frac{t_{exit} - t_w}{t_a - t_w} = \exp\left[- \frac{hp\ z}{c_p \dot{m}} \right] \tag{25}$$

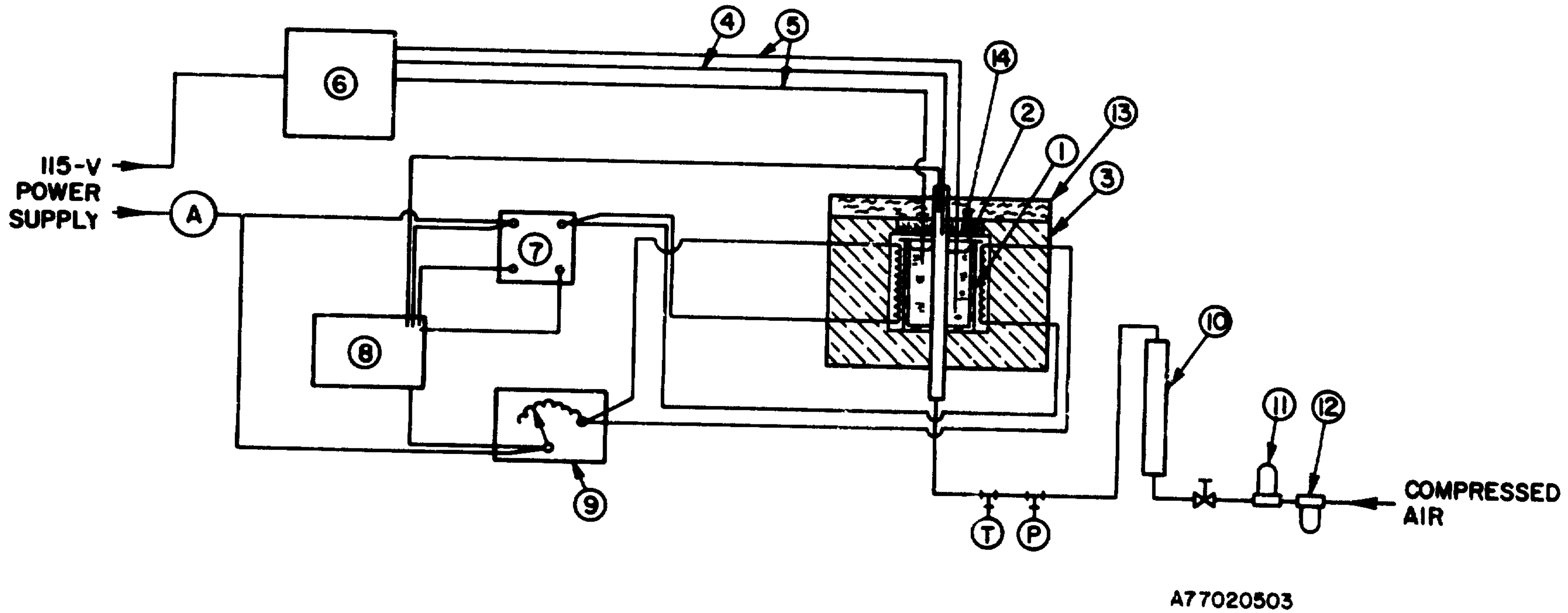

LEGEND

Item No.	Description	Item No.	Description
1	Laboratory TES Container	9	Variable Transformer
2	Aluminum Sheet	10	Flowmeter
3	Electrical Furnace	11	Air Pressure Regulator
4	Thermocouple (Exit Air Temp)	12	Air Filter
5	Thermocouples (Salt Temp)	13	Insulation Wool
6	Temperature Recorder	14	Brick Cap
7	Switch Relay		
8	Temperature Controller		

Figure 7. SCHEMATIC OF LABORATORY TES SETUP

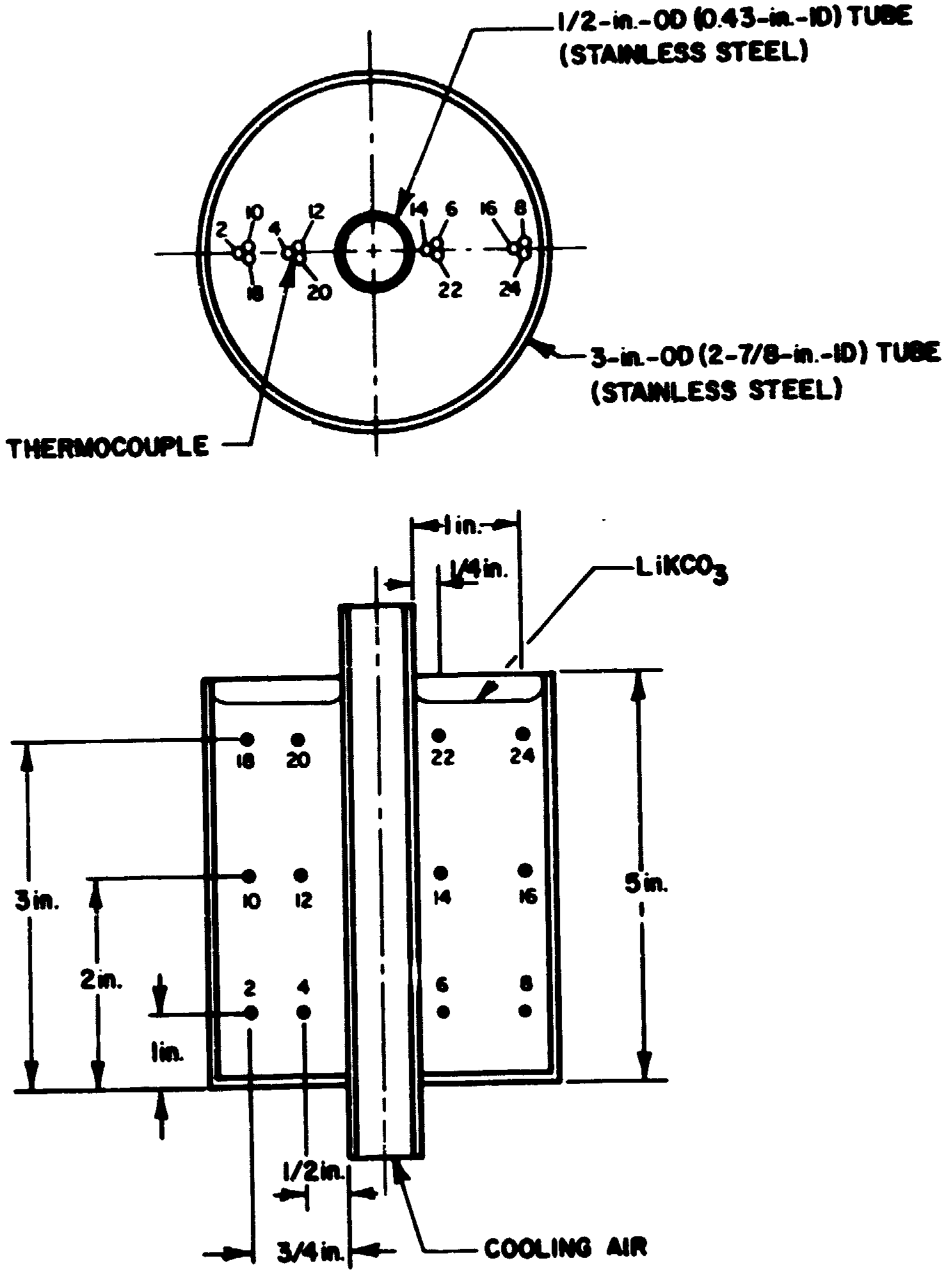

A78030705

Figure 8. DIMENSIONS AND THERMOCOUPLE LOCATIONS IN LABORATORY TES UNIT

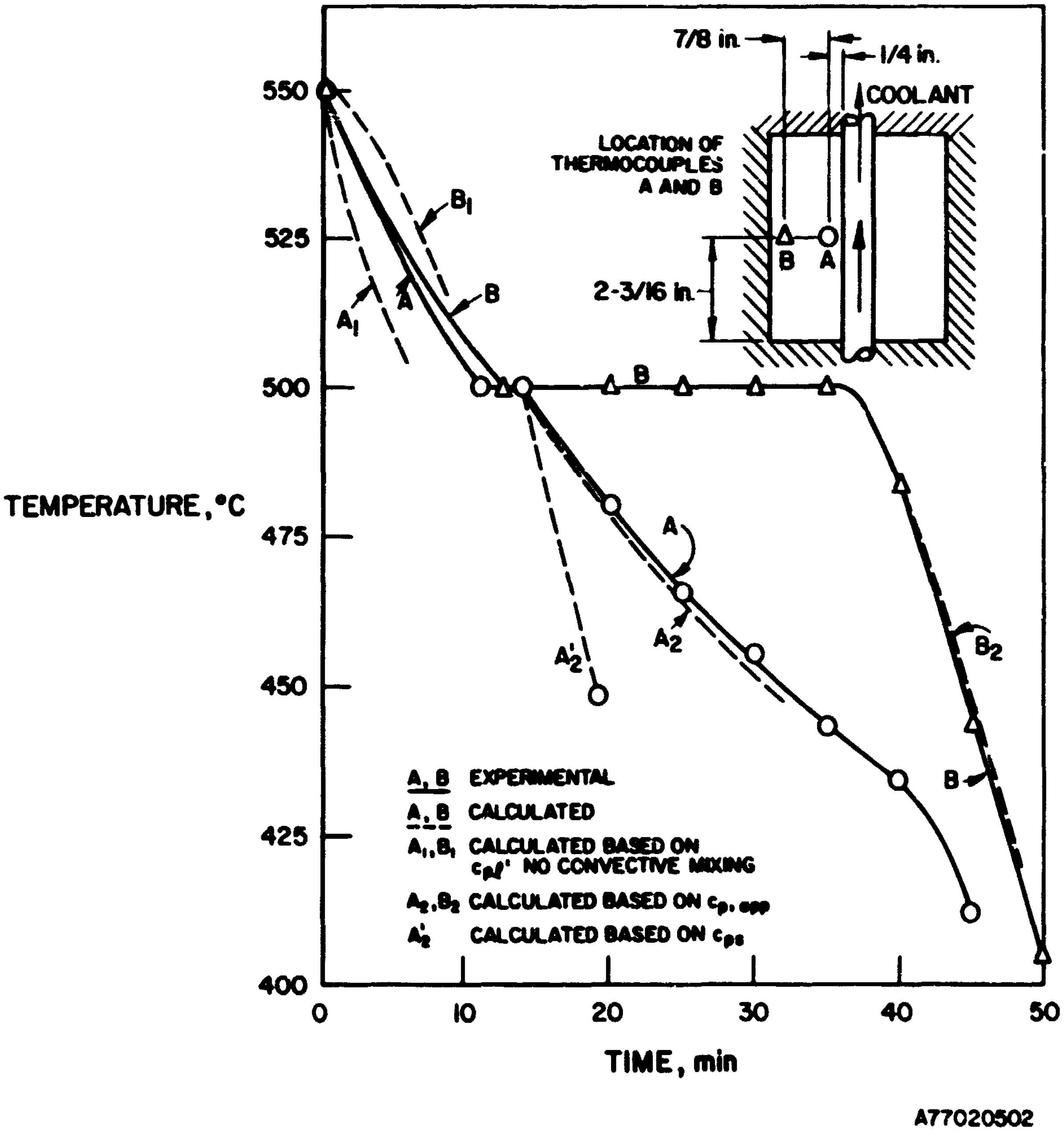

$$c_{p,\,app} = c_{ps}\left[1 + \frac{\Delta H_f}{c_{ps}\,(t_m - t_a)}\right]$$

Figure 9. COOLING RATES IN A LABORATORY TES UNIT

lead to corrected values of $h = 13$ for the heat-transfer coefficient and 65.6°C (150°F) $\equiv \bar{t}_{air}$ for the bulk air temperature. The knowledge of $\bar{t}_{air}$ and of the surface coefficient, h, allows us to calculate the temperature in the liquid phase using standard solutions for conduction heat transfer with boundary conditions of the third kind. A solution[9] of these equations for hollow cylinders assuming a finite conductivity of the material (i.e., no mixing) yields curves (A_1 and B_1, Figure 9) that fail to reproduce the experimental results (curves A, B).

The assumption of perfect internal mixing and no temperature gradient leads to a cooling rate of

$$-\frac{dt}{d\tau} = -\frac{hpz\ (\bar{t} - 150)}{60\ c_p\ m} \doteq -8°\text{F/min} \ (\cong 5°\text{C/min}) \qquad (26)$$

which reproduces the experimental cooling rate of about 5°C/min, and, on integration to $t = 150 + 872\ \exp(-0.0116\ \tau)$, where τ is in minutes, matches the experimental time-temperature curves A and B quite accurately. This suggests vigorous convective (buoyancy driven) mixing in the liquid phase in a cell of the size used here.

In fact, the Rayleigh number $N_{Ra} = \frac{g\beta\Delta TL^3}{\alpha\nu}$ measures the ratio of buoyant to thermal forces in a fluid. With the kinematic viscosity of the liquid estimated at $\nu = 0.17$ ft^2/hr and the thermal diffusivity $\alpha_\ell = 0.0183$ ft^2/hr, the Prandtl number $\nu/\alpha \cong 9$ (comparable to that of water at room temperature). Taking $\Delta t \sim 50$°C (=90°F), the coefficient of volume expansion,

$$\beta = \frac{\rho_\infty - \rho}{\rho\Delta t} \cong 1.4 \times 10^{-4}\,°R^{-1} \qquad (27)$$

Since the significant dimension $L \cong 1/12$, the Rayleigh number is then of the order of 10^6. This is several orders of magnitude higher than the stability criterion ($N_{Ra} \sim 10^3$).[5]

To approach the condition of stability, the width of the liquid-filled gap would have to be reduced by a factor of 10, to about 1/10 inch. Subsequent experiments on solidifying the model storage system ($LiKCO_3$) in a honeycomb matrix of about 1/4-in. mesh showed some temperature gradient between thermocouples A and B but not to the extent predicted by the nonconvection solution curves A_1 and B_1.

ORIGINAL PAGE IS
OF POOR QUALITY

Use of an "Apparent" c_p: Second Part of the Cooling Half-Cycle (The Phase Change)

Figure 9 shows a brief (about 2.5-min) isothermal time lag at 500°C for thermocouple A and a 22-min time lag for thermocouple B. Megerlin's solution (Equation 12, Figure 5) for $N_{ph} = 0.57$ and $N_{Bi} = 0.2$ predicts longer solidification times, 4.7 and 28 min, respectively. This solution, however, is written for an infinitely long cylinder with the heat sink at the interior well only. When heat losses from the outer lateral surface and from the top and bottom are added to the central well loss and the cooling rates are recalculated on that basis, the isothermal lag times become 2.7 min for thermocouple A and 20 min for thermocouple B.

Third Part of the Cooling Half-Cycle (Cooling the Solid Phase)

Thermocouple A begins to indicate solid phase at its location after 12.5 minutes of cooling (Figure 9). The apparent c_p over a temperature range of 505° to 445°C (941° to 833°F) is $0.32 + 148/108 = 1.69$. Used in the analytical solution for the hollow cylinder, it results in the curve A_2, which closely follows the experimental curve A over this range. The use of $c_p = 0.32$, i.e., of the sensible heat alone, results in Curve A'_2, which does not agree with the experimental data.

Thermocouple B is so close to the outer wall that by the time its position has changed from the liquid to the solid phase, the whole mass is solid; there is no evolution of the latent heat, and $c_{ps} = 0.32$ used in the analytical solution adequately describes the behavior of thermocouple B (curve branch B_2, Figure 9).

Design of the Engineering-Scale (8-kWhr$_{th}$) Experimental Storage Unit

The engineering-scale units were designed with the overall goals of the work in mind: 1) to verify the PCM cooling behavior predicted by the analytical solutions, particularly the movement of the solid-liquid interface as a function of discharge time, because of the commercial TES design parameters that can be determined from it (such as heat exchanger spacing), and 2) to accurately determine energy discharge rates, their improvement, and system efficiencies, all of which play a significant role in determining the feasibility of storing thermal energy in PCM.

Based on the considerations discussed in the previous sections, particularly the results of Bramlette et al.,[2] and the experimental results from the laboratory unit, we have selected an annular arrangement for the experimental storage unit. This arrangement can be scaled up. A commercial sized unit with a multihexagonal cell arrangement can be visualized. In addition, this arrangement is the simplest experimentally. The final unit design is shown in Figure 10. The internal radius of the central well used for charging and discharging was chosen to be 1 inch so that the well could accommodate an electric heating element large enough to sustain the power levels and temperatures required to charge the unit in a reasonable time period (10-14 hours at $\tilde{-}$ 1 kWe) while maintaining an annular area large enough to generate a fully developed turbulent flow of the coolant air without requiring high pressures. This radius is also convenient for comparing observed performance to predicted performance ($r_o = 1$).
Electric heating was selected because it allows easy recording of the charging energy and, therefore, accurate determination of the storage efficiency.

The diameter of the heating rod used is 0.75 in., leaving an annular cross-sectional area in the well of 2.7 in.^{2} (0.0187 ft^2). Fans were selected to move the coolant air at the rate of 4600 ft^3/hr, representing a velocity of (4600 ft^3/hr) (0.0187 ft^2)$^{-1}$ (3600 s/hr)$^{-1}$ = 70 ft/s. The corresponding Reynolds number is —

$$N_{Re} = \frac{vd}{\nu} = \frac{(70)(1.25)}{(12)(16.36 \text{ X } 10^{-5})} = 44{,}570 \qquad (28)$$

indicating fully turbulent flow. The heat-transfer coefficient under these conditions can be determined by calculating the Nusselt number:

$$N_{Nu} = \frac{hd}{k_f} = 0.023 \; N_{Re}^{0.8} = 120.5 \qquad (29)$$

Therefore —

$$\begin{aligned} h &= (N_{Nu})(k_f)/d \\ &= (120.5)(0.015)/(1.83/12) \qquad (30) \\ &= 11.9 \text{ Btu/hr-ft}^2\text{-}^\circ\text{F} \end{aligned}$$

The corresponding Biot number is —

$$N_{Bi} = \frac{hr_o}{k_s} = \frac{(11.9)}{(12)(1.3)} = 0.75 \qquad (31)$$

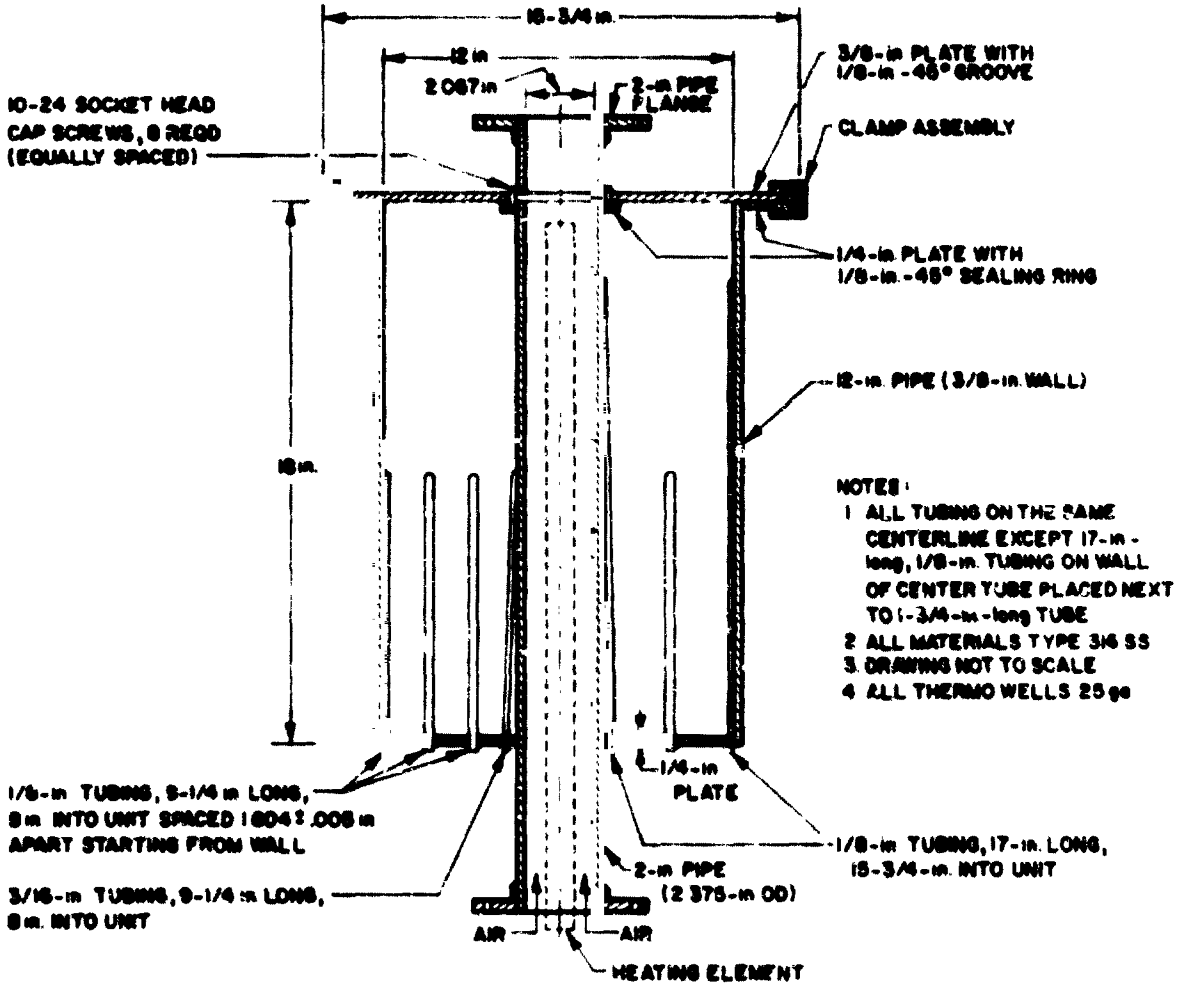

NOTES:
1. ALL TUBING ON THE SAME CENTERLINE EXCEPT 17-in-long, 1/8-in. TUBING ON WALL OF CENTER TUBE PLACED NEXT TO 1-3/4-in-long TUBE
2. ALL MATERIALS TYPE 316 SS
3. DRAWING NOT TO SCALE
4. ALL THERMO WELLS 25 ga

A78030698

Figure 10. ENGINEERING-SCALE THERMAL ENERGY STORAGE UNIT

The analytical solution for a phase-change number = 0.57 (calculated from the properties of the model salt); and an N_{Bi} = 0.75 (Figure 6) was used to determine the container outer radius, allowing complete solidification in a 6 to 8-hour period. A 6-hour discharge period represents a Fourier number of —

$$N_{Fo} = \frac{\alpha \tau}{r_o^2} = \frac{(0.0287)(6)}{(1/12)^2} = 25 \qquad (32)$$

From Figure 6 for N_{Fo} = 25, N_{Bi} = 0.75, and N_{ph} = 0.57, a layer of salt approximately 4.2 in. thick (R-1) can be solidified in a 6-hour period. This represents an outer container radius of 4.2 + 1 = 5.2 in. Similarly, an 8-hour discharge time represents a Fourier number of 33, a salt thickness of 4.7 in., and a container outer radius of 5.7 in. (11.5-in. diam). On the basis of these values and the availability of construction materials, a 12-in. container diameter was selected (Schedule 40 12-in.-diam pipe). It was desired to have 1 ft^3 of salt in the container at room temperature, which would then fill the container to a height of 15.9 in. Allowing a 10% salt volume increase with temperature rise to 941°F (discussed in the next section), the molten salt would fill the container to a height of 17.5 in. (disregarding the expansion of the container). Therefore, a container height of 18 in. (at room temperature) was selected.

Ten thermocouples were located in the salt by inserting 1/8-in. stainless steel tubing (closed at one end) through the container bottom. Eight of the thermocouples were located in the same radial plane, five of these thermocouples at half depth (≈8 in. from the container bottom), one located at the heat-transfer surface, and one each at radial positions (R-1) of 1.6, 2.4, 3.2, and 4.8 in. These thermocouples were used to determine the movement of the solid-liquid interface with time for comparison with the interface movement predicted by the analytical solutions. The three other thermocouples were used to study axial temperature response and edge effects not considered in the analytical solutions. Two other thermocouples located in a perpendicular radial plane at (R-1) positions of 2.4 in. (one on each side of the heat exchanger) and at varying levels throughout the entire salt depth were used to study the axial temperature response in detail. The temperature information generated by the thermocouples was used to approximat the shape of the interface as the salt solidified. The containers were also equipped to measure the height of the molten salt while in operation.

The insulation was selected from the following considerations. Under steady-state conditions the temperature distribution in a cylinder is given by —

$$\frac{d}{dr}\left(r\,\frac{dt}{dr}\right) = 0 \qquad (33)$$

Integrating twice and using the condition at the insulation boundary

$$-k\,\frac{dt}{dr} = h_2(t_2 - t_a) \qquad (34)$$

leads to

$$\frac{t_1 - t_2}{t_2 - t_a} = \frac{h_2 r_2}{k_{ins}} \ln \frac{r_2}{r_1} \qquad (35)$$

where the subscripts denote —

1 = outside radius, storage unit

2 = outside radius, insulation

a = ambient

ins = insulation

It is desired, for safety reasons, and to keep heat losses low, to keep the outside insulation face at 54°C (130°F) or below; then t_1 = 505°C (941°F), t_2 = 54°C (130°F), t_a = 22°C (72°F), h = 1.5 Btu/hr-ft^2-°F (combined radiation and free convection), and k_{ins} = 0.08 Btu/hr-ft-°F (mineral wool) leads to an r_2 of about 12.5 in., or an insulation thickness (r_2 - r_1) of 6.5 in.

Verification of Thermophysical Properties of $LiKCO_3$

The purpose of this task was to determine or verify certain thermophysical properties of $LiKCO_3$ critical to the performance of this salt as a PCM for thermal energy storage. Values for the melting point and heat of fusion have been reported in the literature and verified by DTA, DSC, and electrical conductivity measurements as a function of temperature. The melting point was found to be 505°C (reported value[13] of 504.5 ± 1°C), with a heat of fusion of 151.5 Btu/lb (reported value[13] of 148 Btu/lb). The volume change on fusion was determined from measured thermal expansion coefficients between room temperature and 475°C (887°F). A volumetric expansion of 4.5% was calculated from the expansion coefficients, representing a solid density of 2.13 g/cm^3 at 505°C. The density of liquid $LiKCO_3$ at 505°C was estimated from data of Spedding[26] to be 2.01 g/cm^3, and a volume change on fusion was determined from these density differences to be 6%. Therefore, a 10.5% volume change should be allowed for in containment design.

Supercooling (common in low-temperature systems) was not observed at cooling rates above 5°C/min, and thermal cycling (in the laboratory unit) and corrosion products contained in the salt did not alter the fusion-solidification characteristics. It was also found that thermal cycling had a stabilizing effect on the $LiKCO_3$. When the initial salt was examined by DTA, two endothermic peaks were observed that represent the 485°C eutectic temperature and the melting point of $LiKCO_3$ (Figure 11), indicating a composition slightly rich in Li_2CO_3. After thermal cycling (12 cycles), DTA studies could only detect the fusion of $LiKCO_3$ at $\simeq$ 505°C (Figure 12), indicating that the excess Li_2CO_3 was selectively lost by vaporization, corrosive reactions with the container, or some other mechanism.

Investigation of Conductivity Enhancement and Volume-Change Control Additives

Alkali metal carbonates have relatively higher thermal conductivities (~1 Btu/hr-ft-°F) than the various inorganic salts considered. However, noting that the heat-transfer area required for a given quantity of heat depends strongly on thermal conductivity (particularly in the solid region of the salt), the heat-transfer area and the resulting cost of the storage system can be minimized if the conductivity of the salt medium can be improved. We therefore investigated the use of high-conductivity materials as conductivity promoters. Considerations for the selection of suitable conductivity promoters include —

1. Thermal conductivity and heat capacity
2. Compatibility with carbonates
3. Availability
4. Suitability of fabrication in desirable forms
5. Cost.

ORIGINAL PAGE IS
OF POOR QUALITY

After the initial considerations, different materials in various shapes were experimentally tested in our laboratory TES (3-in.-diam container) unit.

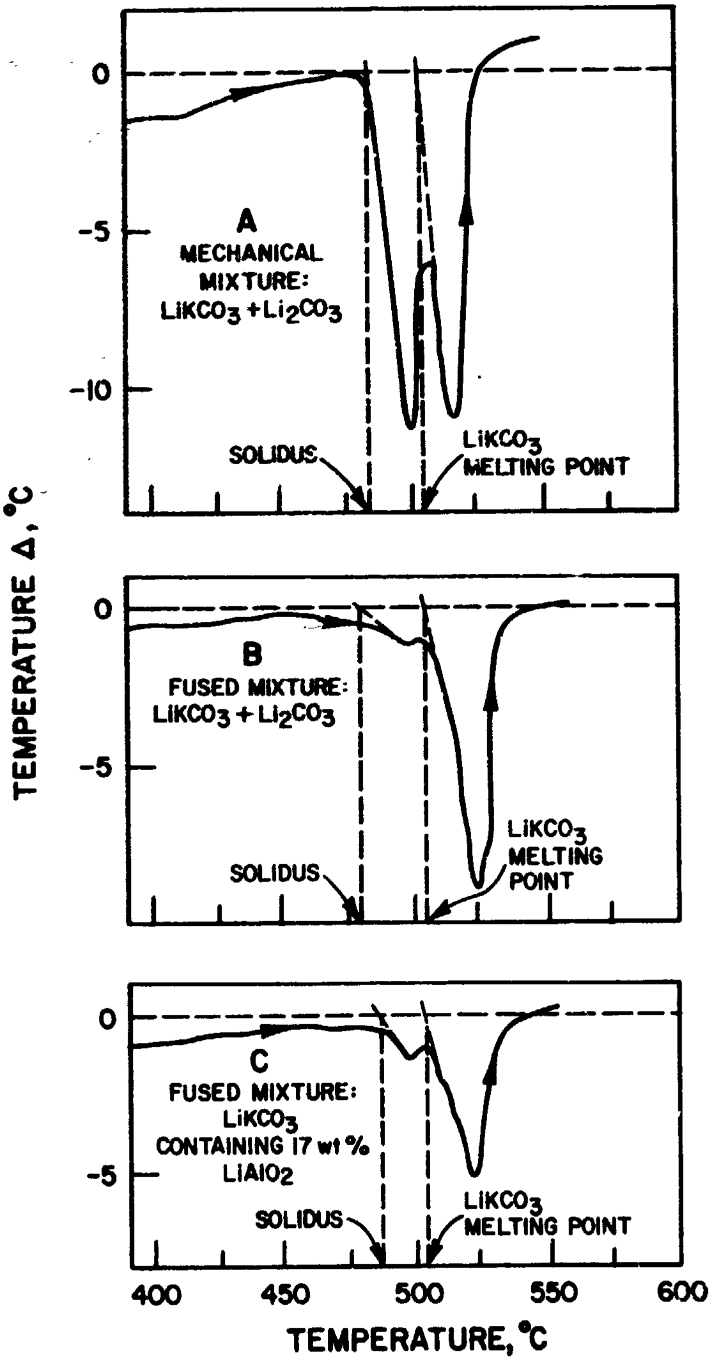

A77020501

Figure 11. DTA TRACES OF MECHANICAL AND FUSED MIXTURES OF $LiKCO_3$

ORIGINAL PAGE IS OF POOR QUALITY

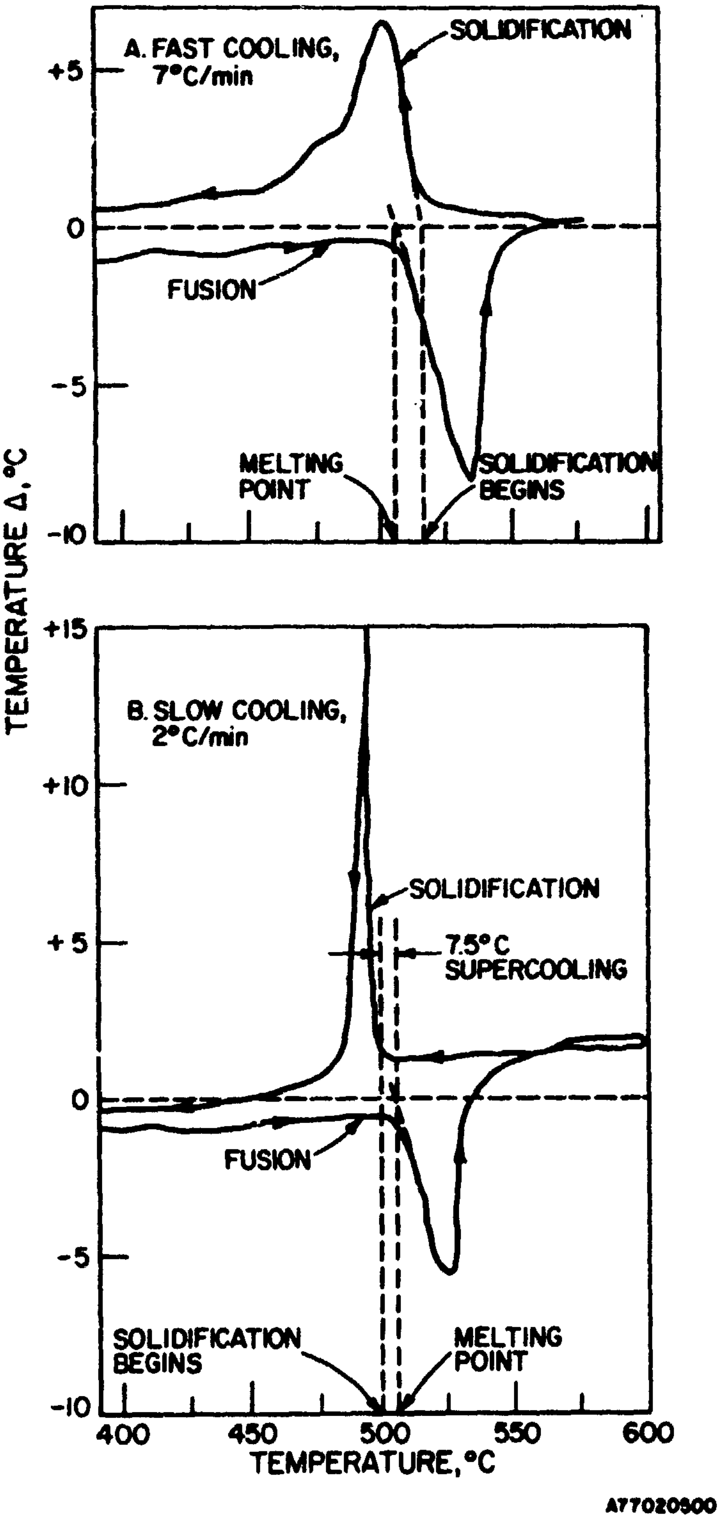

Figure 12. DTA TRACES OF THERMALLY CYCLED $LiKCO_3$

The feasibility of using $LiAlO_2$ as a volume-control material to randomly distribute voids resulting from volume changes as the $LiKCO_3$ solidifies was assessed by examining the storage capacity sacrificed by the addition of $LiAlO_2$, determining the rate at which the $LiAlO_2$ particles settle from the carbonate-aluminate paste, and examining the influence of $LiAlO_2$ on the discharge heat flux and system efficiency. The results of these studies are discussed below.

Investigation of Conductivity-Promoter Additives

As previously discussed under "Transient Solutions," the heat-transfer resistance in the PCM appears to be the major TES performance-limiting factor. This effect, which results because the low thermal conductivity in the solid phase damps the heat flux through the solid PCM formed on the salt-side heat-transfer surface, is the primary drawback in using a passive heat exchanger in such a system. If the thermal conductivity of the solid PCM can be cost-effectively increased, performance improvements will result.

The most attractive method of conductivity enhancement appears to be by the addition of higher conductivity materials to the salt in the form of screens, wool, foams, honeycomb matrix, or particles. Several materials were considered for this application. Their relevant properties are summarized in Table 3. Some corrosion tests that were conducted with graphite showed that this material may not be stable in the molten carbonate environment. Dispersed particles do not provide significant heat-transfer enhancement, according to Siegel,[25] so they were not tested.

To obtain relative improvement in heat-transfer rates with the addition of conductivity promoter, we tested some available materials in our laboratory TES system. Figures 7 and 8 show the constructional details, and the locations of thermocouples in the system. A 3-in.-diam, 5-in.-long stainless steel tube with the bottom end sealed, containing 800 g $LiKCO_3$, was heated in an electric furnace with a heat input of 9 A at 115 V (heating rate of approximately 5°C/min). After the carbonate reached the equilibrium temperature, the cooling air (50 ft/s) was fed from the bottom of the 1/2-in.-OD center tube. Testing was conducted with $LiKCO_3$ alone and for $LiKCO_3$ with a) 3% by volume stainless steel screen attached to the center cooling tube, b) 3% by volume aluminum honeycomb matrix immersed in the salt, and c) 3% by volume stainless steel wool immersed in the salt. The results of these tests, summarized in Table 4,

Table 3. PROPERTIES OF MATERIALS CONSIDERED AS CONDUCTIVITY PROMOTERS

Material	Thermal Conductivity, Btu/hr-°F-ft		Heat Capacity Btu/lb-°F		Material Cost,		Remarks
	at 100°C	at 500°C	Room Temp	at 500°C	$/lb	$/ft³	
Type 304 L SS	9.4	12.5	0.12	--	0.948	475	
Type 316 SS	9.4	12.5	0.12	--	1.273	638	
Type 347 SS	9.3	12.9	0.12	--	2.510	1258	Best corrosion resistance of 300 series SS
Type 430 SS	15.1	15.2	0.11	--	0.841	421	
Type 446 SS	12.1	14.2	0.12	--	2.555	1192	
Aluminum	136	127	0.22	0.27	0.792	134	660°C mp; may become soft if temp of system increases accidentally.
Pyrolytic Graphite	300	120	~ 0.2	--	924.00	130,000	As deposit; thermal conductivity was measured parallel to basal plane
Graphite ATJ	65	43	0.2	0.38	4.47	626	Thermal conductivity was measured parallel to grain
Graphite CS	70	44	0.2	0.38	0.50	68	0% porosity

A77020134

ORIGINAL PAGE IS
OF POOR QUALITY

Table 4. COMPARISON OF HEAT-TRANSFER RATES TO COOLING AIR FROM LiKCO$_3$ WITH OR WITHOUT ADDITIVES (Conductivity Promoters and Volume Control Additives)

Description	Air Temp, °C		Air Mass Flow Rate, lb/min	Operating Temp Range, °C	Q_s,[b] Btu	Q_t,[c] Btu	q,[d] Btu/hr-ft²	Q_t/Q_s X %
	T_{in}	T_{out}[a]						
LiKCO$_3$	24	97	0.224	545-450	413	281	9281	68
LiKCO$_3$ with 3 vol % of SS Screen	26	106	0.222	547-450	420	313	10,340	75
LiKCO$_3$ with 3 vol % of Aluminum Honeycomb	27	116	0.222	542-450	412	335	11,060	81
LiKCO$_3$ with 3 vol % of SS Wool	25	119	0.224	548-450	420	365	12,055	87
LiKCO$_3$ with 3 vol % LiAlO$_2$	24	97	0.224	550-450	424	279	--	66

[a] $T_{out} = \frac{1}{\Delta t}\int_{t=0}^{t=40} T(t)\,dt$, where

T_{out} = integrated temperature of exit air

t = time

Δt = period of time.

[b] $Q_s = m_s c_p(s)\,\Delta T + \Delta H \cdot m_s + m_m c_p(m)\,\Delta t$, where

Q_s = theoretical heat that can be extracted from pilot TES unit in the operating temperature range, 450° to 550°C.

m_s = mass of salt, 1.76 lb of LiKCO$_3$

$c_p(s)$ = specific heat of salt (solid or liquid)

ΔT = operating temperature range, °C

ΔH = heat of fusion, 148 Btu/lb for LiKCO$_3$

m_m = mass of conductivity promoter

$c_p(m)$ = specific heat of conductivity promoter.

[c] Q_t = actual heat transferred to cooling air from pilot TES unit in 40 minutes after cooling started.

[d] q = heat flux (cooling tube surface area 6.54 in.²).

B77020145

show that although stainless steel has a low thermal conductivity its conductiivty-enhancing effect is good if used as a wool. We then obtained a relatively fine aluminum wool and tested it at concentrations of 3, 10, and 14 volume percent.

The results of these tests are shown in Figure 13. The $LiKCO_3$ alone shows a uniform heat flux with cycling, whereas the units containing the aluminum wool show an initially higher heat flux, which increases further with continued cycling. As a result of this behavior, a quantitative dependence of the output heat flux on the conductivity-promoter concentration could not be established. Further cycling of the units that contain 10% and 14% aluminum wool is expected to result in steady-state performance (no further change of the heat flux with cycling), as seen in the unit containing only 3% aluminum wool. When all of the containers are operating under this equilibrated condition, the appropriate relationship can be derived. The additional cycling, however, has not been performable because of mechanical problems.

The primary observation to be made, therefore, is that at each concentration of aluminum wool, an increase in the output heat flux was immediately attained and it continued to improve with cycling.

Two possible expanations for the dependence of the output heat flux on cycling are —

1. More intimate contact between the frozen salt and the aluminum wool resulting from slight corrosive reactions on the aluminum (possibly the formation of a thin $LiAlO_2$ surface layer), and
2. A radial movement of the aluminum wool toward the heat exchange surface, resulting from the contraction of the salt as it solidifies.

It is difficult at this time to ascertain which of these mechanisms may be controlling and what contribution each makes toward the observed behavior. However, there is evidence for each, and the lesser dependence of heat flux on cycling observed in the salt containing the least amount of aluminum wool would support either.

One of the primary difficulties in using a wool-type conductivity promoter is obtaining good contact with the heat exchange surface. Therefore, an alternative means of improving the salt conductivity by ensuring good contact between the conductivity promoter and the heat-transfer surface was also tested. A

ORIGINAL PAGE IS OF POOR QUALITY

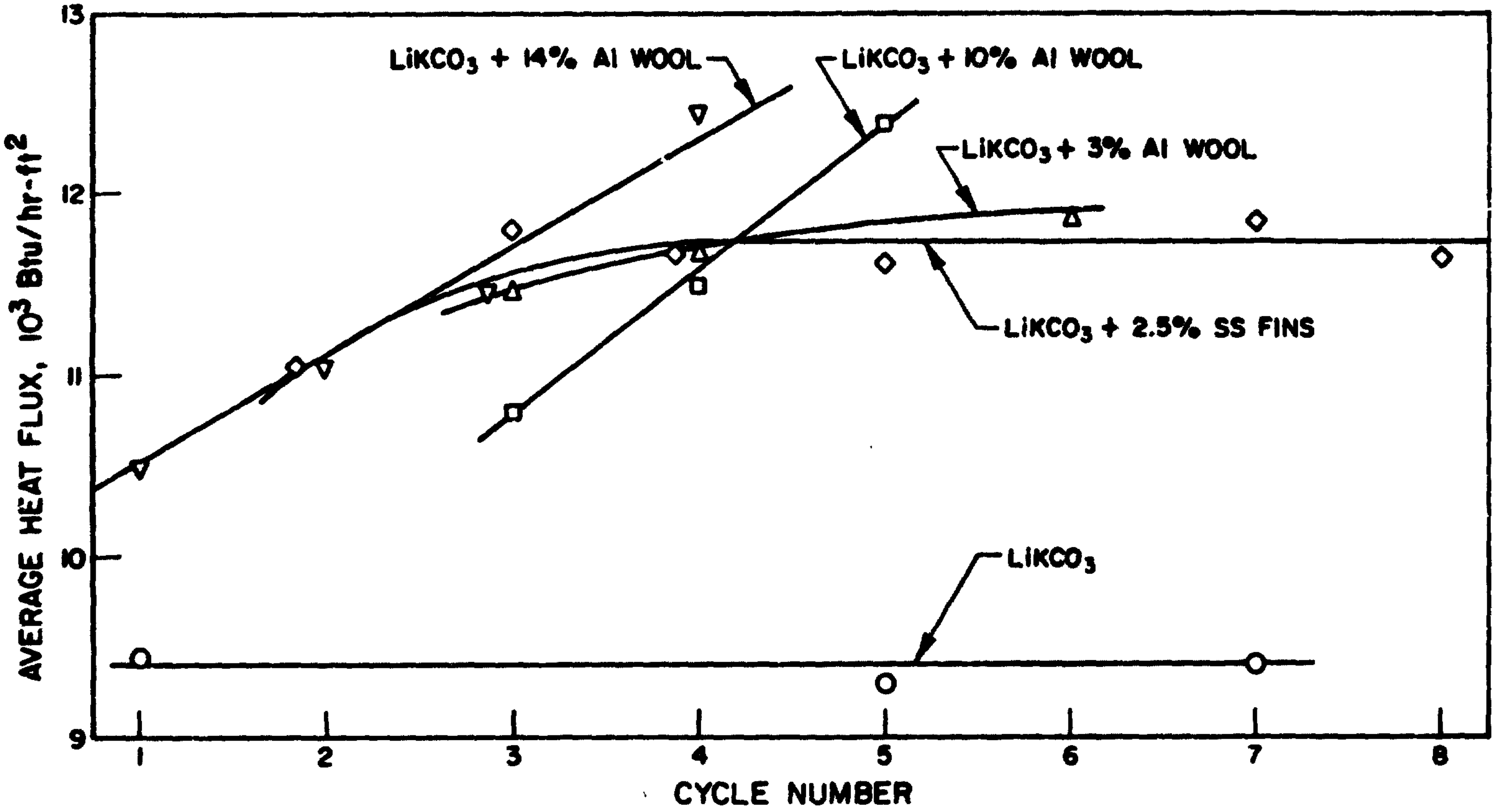

Figure 13. EFFECT OF THERMAL CONDUCTIVITY ENHANCERS

finned-tube heat exchanger was fabricated and tested on the laboratory-scale unit. The eight fins, which were welded to the heat-transfer surface to ensure good contact, displaced ~2.5% of the salt volume and extended midway into the salt. The results obtained from this unit are also shown in Figure 13. The maximum heat flux obtained is about the same as that with 3 volume percent aluminum wool. This results shows that a high-conductivity material distributed evenly through the salt in random orientation is as effective as a lower-conductivity material with a more intimate contact. However, the fabrication costs are a great deal higher for a finned-tube heat exchanger. The aluminum wool is, therefore, as effective in enhancing conductivity, but is more cost effective, and appears to be the most promising conductivity-enhancement concept.

Investigation of Volume-Change Control Additives

The containment of a PCM used as a TES medium is complicated by the differences in thermal expansion between the containment material and the PCM and by the volume change accompanying fusion of the PCM. Differences in thermophysical behavior between storage and containment materials can lead to more complex containment design, increased containment cost, and lower volumetric storage capacity (based on container size). Each of these effects can decrease both the practicality and efficiency of TES that utilizes the heat of fusion of a PCM. The thermophysical properties of a PCM alone cannot be modified or controlled. However, they can be substantially reduced by creating a composite storage material containing both the PCM and an inert volume-control material. This latter material is characterized by its stability, thermal expansion, and particle size and morphology. The material is selected so that its thermal expansion is considerably lower than that of the PCM, thereby producing a composite thermal expansion lower than that of the PCM alone.

Furthermore, the particle size distribution and morphology must be such that loosely packed particles form a tight, continuous capillary network. When the PCM is molten, all of the void space within the volume-control matrix is filled with the liquid. As the PCM solidifies and undergoes the accompanying volumetric contraction, the capillary network serves to localize the resulting voids on a microscopic scale, within the capillaries. The net effect is to distribute the void space (resulting from the PCM volume change on solidification) throughout the composite storage medium. Therefore, on a macroscopic scale, the volume change accompanying a phase change and the void space required to accommodate it are barely detectable. As a result, any void formation or breakaway from the heat-transfer surfaces can be minimized. A closed containment vessel filled with a composite storage medium would not be subjected to the stresses induced by volumetric expansions and contractions accompanying fusion and solidification of the PCM. Therefore, associated complications in containment design and structure are eliminated. On the other hand, the incorporation of a volume-control material into a storage medium is disadvantageous in that the storage capacity lost by the displacement of the PCM is only partially recovered as sensible heat storage in the volume-control material.

We have selected $LiAlO_2$ as a volume-control material because —

- The PCM being studied ($LiKCO_3$) is in the lithium carbonate-potassium carbonate system; the chemical inertness of $LiAlO_2$ to components in this system has already been proven;[3,19]
- The coefficient of thermal expansion of $LiAlO_2$ is approximately one-third that of $LiKCO_3$; and
- The ability of this material to develop the required capillary network has been displayed in past work at IGT.[21]

The effects on storage capacity (Btu/lb) and specific capacity (Btu/ft^3) of lithium aluminate additions to $LiKCO_3$ are shown in Figure 14. Capacity values for the composite storage medium were calculated for a 100°C cycling (505° ± 50°C). Under these conditions, the storage capacity of pure $LiKCO_3$ is 224 Btu/lb (148 Btu/lb as the heat of fusion and 76 Btu/lb as sensible heat). It is estimated that $LiAlO_2$ must be added in excess of 30% by weight to effectively control the volume change of $LiKCO_3$ on fusion. The storage capacity of the composite is reduced to 170 Btu/lb with $LiAlO_2$ added in this amount. This composite represents a 24% decrease in storage capacity and a 17.5% decrease in specific capacity from that of $LiKCO_3$ alone.

More important is the effect of $LiAlO_2$ additions on capacity cost. The capacity cost of $LiKCO_3$ operating under 100°C cycling is $1790/million Btu. A composite storage medium containing 30 weight percent $LiAlO_2$ and 70 weight percen $LiKCO_3$ operating under the same 100°C cycling would have a capacity cost of $6150/million Btu, a 244% increase.

Another anticipated difficulty is maintaining a uniform distribution of the volume-control material throughout the composite. If the volume-control material settles out of the composite, the capillary network needed to control

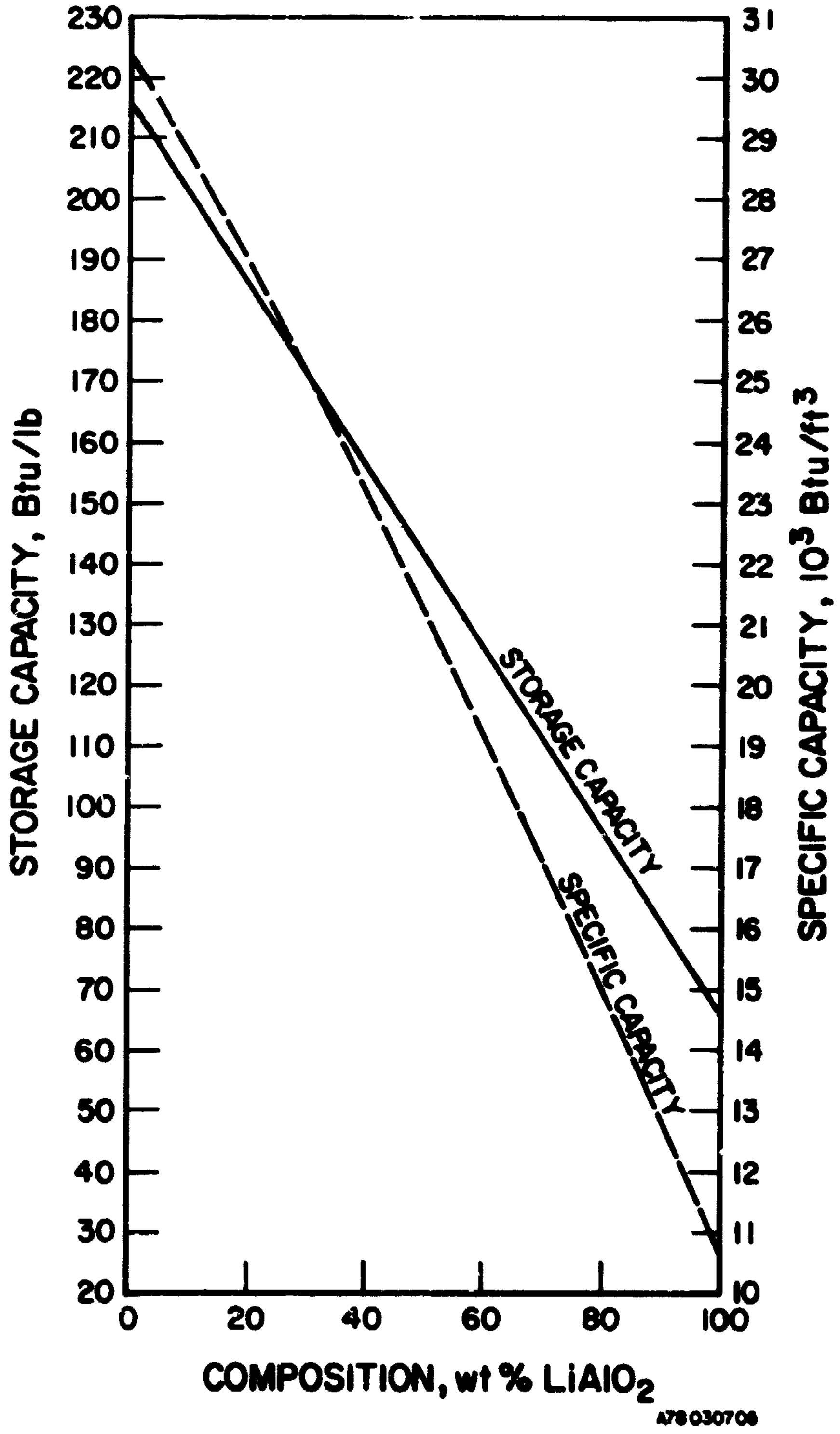

Figure 14. CAPACITY VARIATION WITH COMPOSITION OF $LiKCO_3$-$LiAlO_2$ COMPOSITE STORAGE MEDIUM

the volume change accompanying fusion of the PCM is destroyed. As the additive material settles, the volumetric changes of the composite increase with cycling. This may cause undesirable voids and a safety hazard if the design for storage container expansion assumes that the composite contains an even distribution of the additive material. The particle size and density of the additive material and the viscosity and density of the liquid in which the particles are suspended determine the rate at which the particles will settle through the liquid. $LiAlO_2$ has a density of 2.6 g/cm^3 (primarily β and γ crystalline phases); molten $LiKCO_3$ has a density of 2.0 g/cm^3 and a viscosity of 10 to 15 cP near the melting point.

An analysis was made of this sedimentation effect. The settling rate of $LiAlO_2$ through molten $LiKCO_3$ as a function of $LiAlO_2$ particle size was estimated by Stokes' law and is shown in Figure 15. Sedimentation tests were conducted on a composite mixture containing 83 weight percent $LiKCO_3$ and 17 weight percent $LiAlO_2$ and having a particle size distribution between 0.01 and 0.2μ diameter. The powder was packed into Type 304 stainless steel columns 1-1/4 in. in diameter and 12 in. deep. The columns were then heated to 530°C and air quenched after 300, 700, and 1250 hr at these temperatures. Samples were then taken from the uppermost and lowest centimeter depths, and the $LiAlO_2$ concentration was determined. The results of this test are shown in Figure 16. The settling rate calculated from Stokes' law for the average particle size of the $LiAlO_2$ used in this test was 3 mm/1000 hr. The settling rate determined from this test was 3mm/1000 hr, indicating that sedimentation would be a minor problem in long-term operation.

Besides the problems of high cost and reducing the storage capacity, addition of $LiAlO_2$ to $LiKCO_3$ can also hinder the heat-transfer characteristics. A composite storage medium containing 3 percent by volume $LiAlO_2$ in $LiKCO_3$ was tested in the pilot TES system to study this effect. The results are included in Table 4 for comparison with pure $LiKCO_3$, and $LiKCO_3$ with conductivity promoters added. Taking pure $LiKCO_3$ as a standard for comparison shows the heat recovery (Q_t/Q_s) reduced from 68% to 66% by the addition of $LiAlO_2$ at this level, and the heat flux reduced from 9280 to 9215 Btu/hr-ft^2. Although these changes are small, they indicate the decrease in overall system efficiency resulting from the addition of $LiAlO_2$ to the $LiKCO_3$.

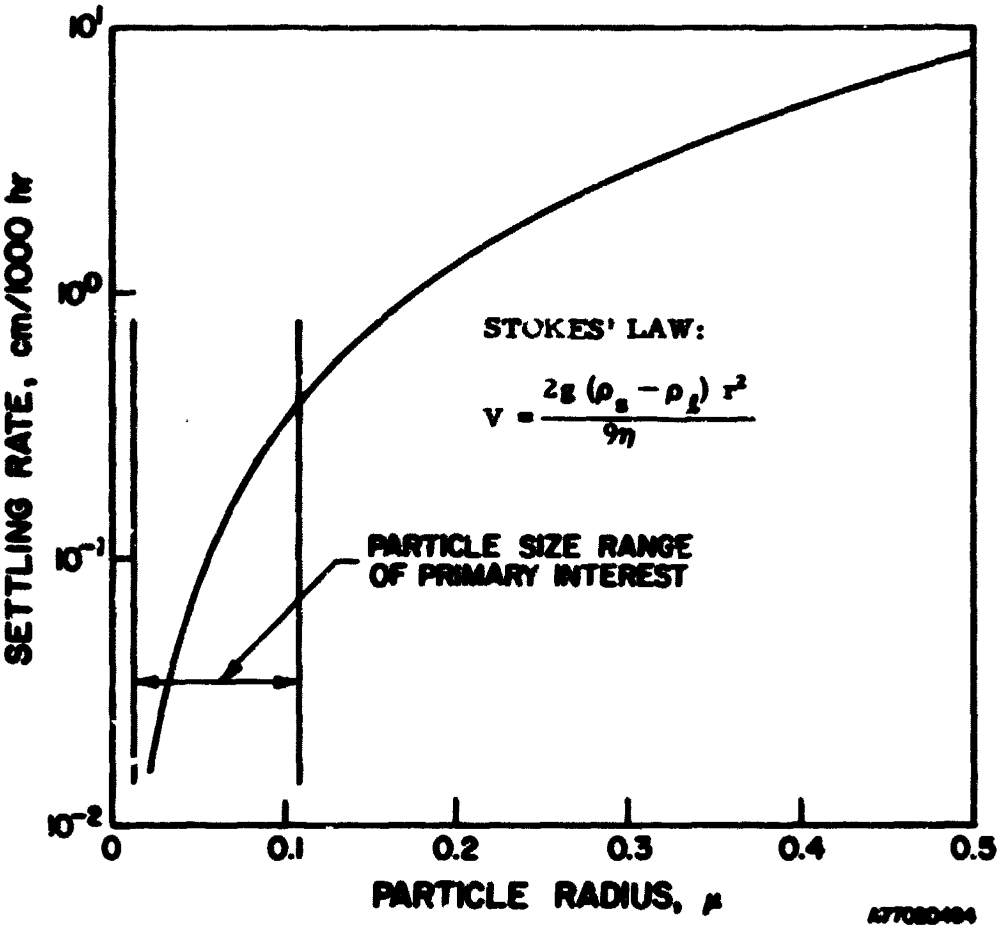

Figure 15. CALCULATED SETTLING RATE OF $LiAlO_2$ IN MOLTEN $LiKCO_3$ AT 525°C

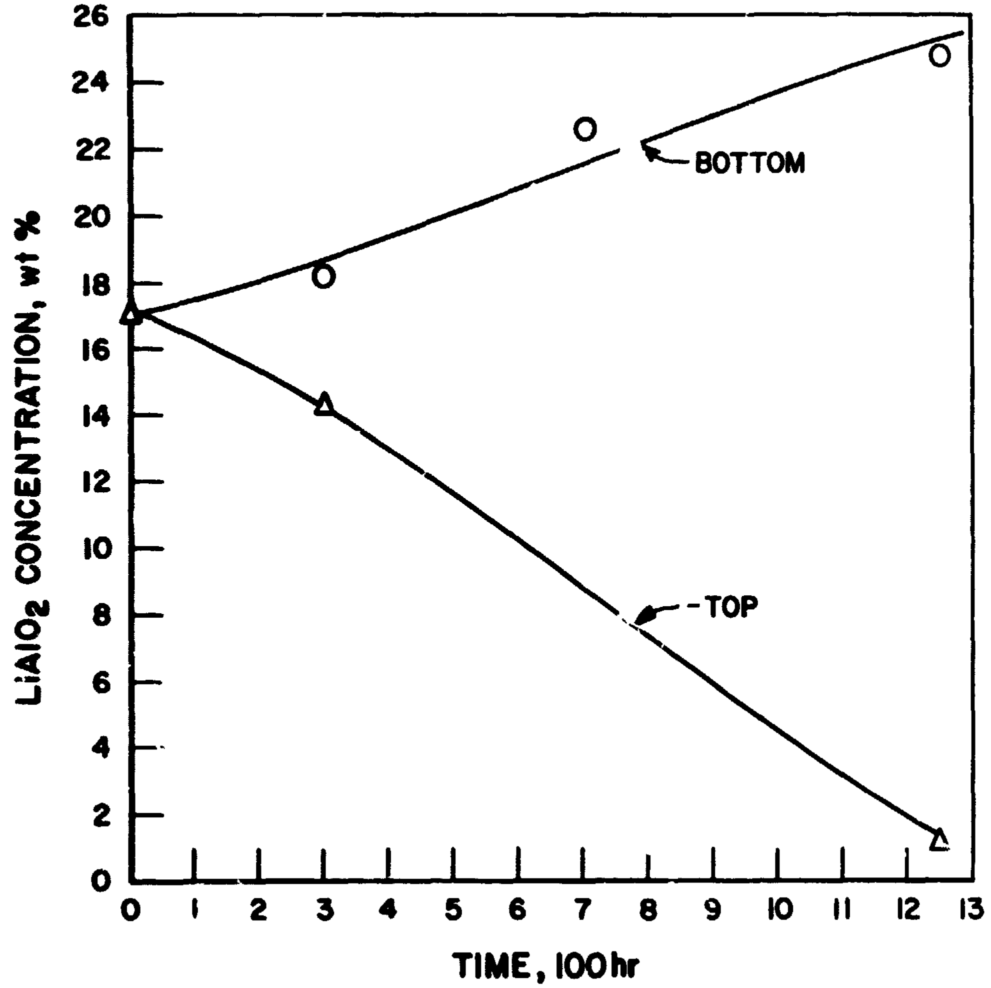

A77020497

Figure 16. OBSERVED SEDIMENTATION OF $LiAlO_2$ IN MOLTEN $LiKCO_3$ AT 530°C

ORIGINAL PAGE IS
OF POOR QUALITY

The decrease in storage capacity and system efficiency and the increase in capacity cost resulting from $LiAlO_2$ additions represent disadvantages of the use of $LiAlO_2$ as a volume-control additive. Because the volume change of $LiKCO_3$ in our system is $< 10\%$, the benefits to be derived from volume-change control additive may be less important than the accompanying disadvantages. However, if a high-volume-change system such as chlorides is used, the volume-control additive may become important.

Construction Materials

The heat exchanger conduits, the construction materials for containment of the salt, and the conductivity promoters must withstand the corrosive attack of the salt. As we briefly described in our Task I Report on Salt Selection,[18] carbonates are relatively less corrosive than chlorides, fluorides, sulfates, and phosphates. Molten carbonates are used in fuel cells,[19] gasification of coal,[1] cleanup of sulfur-containing gases,[7] and other applications. A reasonable amount of corrosion data on molten carbonates is, therefore, available. Although specific data for our PCM, $LiKCO_3$, is scarce, data on other alkali-metal carbonate mixtures have been reported; and we believe that the corrosion behavior of $LiKCO_3$ would be similar to that of the other alkali-metal carbonates.

Corrosion Data

Janz and coworkers[14,15] studied corrosion of Types 304 and 347 stainless steels in the Li_2CO_3-Na_2CO_3-K_2CO_3 ternary eutectic under submerged conditions. From their experiments, the authors concluded that both Types 304 and 347 are passivated under submerged conditions in an oxidizing environment. A corrosion of 10 mils/yr was reported for Type 347 stainless steel in static tests at 730°C. (See Table 5.)

Davis and Kinnibrugh[6] studied corrosion by the Li_2CO_3-Na_2CO_3 eutectic mixture under fully and partially submerged conditions, and reported a greater corrosion attack under partially submerged conditions. This observation is important for our TES system because a partially submerged condition is likely to occur at the liquid-gas interface at the top of the liquid $LiKCO_3$. Differences in the activity of the oxidizing species in the meniscus area and in the bulk liquid are responsible for the higher degree of corrosion. Experimental verification of the expected greater corrosion will be discussed

Table 5. CORROSION RATES OBSERVED BY VARIOUS INVESTIGATORS

Material	Composition of Carbonates	Gas Environment	Temp, °C	Time, hr	Corrosion Rate, mils/yr	Remarks	Reference
1020 Steel	Ternary eutectic^e	Air	500	50	4.84	Static test	1
Type 304 L SS	Ternary eutectic	Air	500	50	0.48	Static test	1
		Air	600	50	-4.8^g	Static test	1
Type 310 SS	52 Li_2CO_3 + 48 Na_2CO_3	O_2 + CO_2 (?)	680	--^{f}	1.5	@ -850 mv, submerged	5
		O_2 + CO_2 (?)	680	--^{f}	4.2	@ -100 mv, submerged	5
	Ternary eutectic	Air	600	50	4.8	Static test	1
Type 321 SS	52 Li_2CO_3 + 48 Na_2CO_3	O_2 + CO_2 (?)	680	--^{f}	6.9	@ -850 mv, submerged	5
		O_2 + CO_2 (?)	680	--^{f}	7.6	@ -100 mv, submerged	5
Type 347 SS	43.5 Li_2CO_3 + 31.5 Na_2CO_3 +25 K_2CO_3	CO_2	730	95	10	Submerged	13
	52 Li_2CO_3 + 48 Na_2CO_3	O_2 + CO_2 (?)	680	--^{f}	2.2	@ -850 mv,^{h} submerged	5
		O_2 + CO_2 (?)	680	--^{f}	1.3	@ -100 mv,^{h} submerged	5
	Ternary eutectic	Air	600	50	2.4	Static test	1
		Air	700	50	3.1	Static test	1
		Air	600	1500	0.3	Dynamic test	1
		Air	700	1500	>90	Dynamic test	1
		Air	500	8000	0.2	Dynamic test	1
Type 430 SS	Ternary eutectic	Air	500	50	2.86	Static test	1
Kanthal A	52 Li_2CO_3 + 48 Na_2CO_3	O_2 + CO_2 (?)	680	--^{f}	0	@ -850 mv^h	5
	53% $LiAlO_2$ + ternary eutectic	Air (?)	700	1000	0	Wires embedded in a paste mixture	5
Kanthal A-1	52 Li_2CO_3 + 48 Na_2CO_3	O_2 + CO_2 (?)	680	--^{f}	0	@ -850 mv,^{h} submerged	5
			700	--^{f}	0.16	@ -100 mv,^{h} submerged	5
Graphite^a	Ternary eutectic	Air	500	50	2.6	Static test	1
Graphite^b	Ternary eutectic	Air	500	50	1.8	Static test	1
Graphite^c	Ternary eutectic	Air	500	50	150	Static test	1
Graphite^d	Ternary eutectic	Air	500	50	6.2	Static test	1
Alumina	Ternary eutectic	Air	500	50	negligible	Static test	1

[a] AGSX graphite #571X.
[b] Carborundum Metal Pumping Service graphite.
[c] K. B. Bonite graphite.
[d] Raschig ring 571 B.
[e] Ternary eutectic composition is 43.5 mol % Li_2CO_3 + 31.5 mol % Na_2CO_3 + 24 mol % K_2CO_3.
[f] Potentiostatic polarization scans.
[g] Negative sign indicates a weight gain during the test.
[h] Working potential with reference to 67 CO_2 + 33 O_2 reference electrode.

B77020136

ORIGINAL PAGE IS
OF POOR QUALITY

in the following section. Davis and Kinnibrugh also noted that ferro-aluminum alloys, such as Kanthal A, Kanthal Al, and Hoskins 815 were more resistant than the 300-series stainless steels.[6] (See Table 5.)

Atomics International[1] has employed molten carbonates for sulfur removal and as reaction media for in situ combustion. They have carried out detailed studies of corrosion by carbonates under static and dynamic conditions; their melts consisted of the ternary eutectic by itself as well as with additions of 20% sulfide or 20% sulfite melts. Some results of their 50-hour static tests and 1500-hour dynamic corrosion tests at 500°C are summarized in Table 5. The Atomics International report contains additional data for various alloys and ceramic materials. Their results suggest that —

1. Up to 600°C, Type 347 stainless steel appears to be satisfactory for containing ternary carbonates in the presence or absence of sulfur compounds. A 1-year dynamic test at 500°C showed a corrosion of only 0.2 mils/yr for this stainless steel.
2. At higher temperatures, containment of these melts requires high-chromium alloys, ceramics, cermets, or a frozen skull of the salt.

Corrosion data on various grades of graphites has also been reported by Atomics International (Table 5). The corrosion rate obtained from 50-hour exposure tests varied from 20 to 150 mils/yr. Graphite is attractive as a conductivity promoter because of its high conductivity, but its corrosion behavior for different grades of interest needs to be investigated.

Aluminum is also a possible candidate for a conductivity promoter because it possesses a high conductivity and can also be considered as a construction material. Aluminum is resistant to carbonates at temperatures[12] up to 600°C; at the Institute of Gas Technology, we have operated molten carbonate fuel cells at 500° to 600°C using aluminum hardware.[12] Noting that the melting point of aluminum is 660°C, the corrosion resistance of aluminum appears remarkable. This is possible because of the formation of a protective alumina layer on the surface, which in turn reacts with carbonates to form a highly protective layer of lithium aluminate.[6]

The TES unit should be designed for periodic (daily) cycles, so data on corrosion of materials under thermal-cycling conditions will be required. Atomics International also studied the effect of thermal cycles on corrosion rates. If the passivated films separate from the substrate during thermal cycles, the corrosion rate is expected to be greater than that found in constant-temperature tests. For Haynes 25 and Hastelloy G and X, the corrosion rate was found to be 5 to 20 times greater under thermal cycling.

Stress-corrosion cracking and the effect of chlorides, sulfides, sulfites, and sulfates under various conditions have also been studied.[7] Sulfur compounds enhanced corrosion, but chloride compounds did not alter the corrosion rate markedly. Therefore, it is desirable to avoid sulfur-bearing impurities in commercial $LiKCO_3$ powder. Higher corrosion rates can be expected if stresses exist in the components.

Corrosion Mechanisms and Thermodynamics

Examination of the outer film of the stainless steels showed[7] that a dense layer of $LiCrO_2$ was formed, which is protective up to 700°C. This conclusion, based on X-ray diffraction and fluorescence studies, is in disagreement with that of Janz and Conte,[14] who reported a $LiFeO_2$ layer as the corrosion product. It is possible that, because the X-ray diffraction patterns of $LiFeO_2$ and $LiCrO_2$ are similar,[1] Janz and Conte could not distinguish between $LiFeO_2$ and $LiCrO_2$. The results of Atomics International in using X-ray fluorescence are therefore more reliable. Note that, in either case, some loss of Li_2CO_3 can be expected from the initial Li_2CO_3-K_2CO_3 mixture. Because of the relatively large quantities of salt mixture compared with the amount of corrosion products formed, the loss of Li_2CO_3 will be insignificant.

Experimental Observations

ORIGINAL PAGE IS OF POOR QUALITY

The corrosion of two materials was measured:

1. Type 304 stainless steel tube used for $LiAlO_2$ settling studies
2. Aluminum honeycomb in the laboratory TES unit.

Type 304 stainless steel tube was used for determining settling rates in a $LiKCO_3 + LiAlO_2$ mixture at 530°C (Figure 16). Two metallographic sections were obtained from the tube heated for 1250 hours: 1) in the meniscus area at the top of the tube, and 2) in the middle of the tube, where the interior wall of the tube is completely surrounded by the molten salt. Figure 17 show a metallograph of the material exposed in the meniscus area, which shows a corrosion of 2 mils in 1250 hours. This is equivalent to 14 mils/yr if a linear corrosion behavior is assumed. However, corrosion behavior is generally

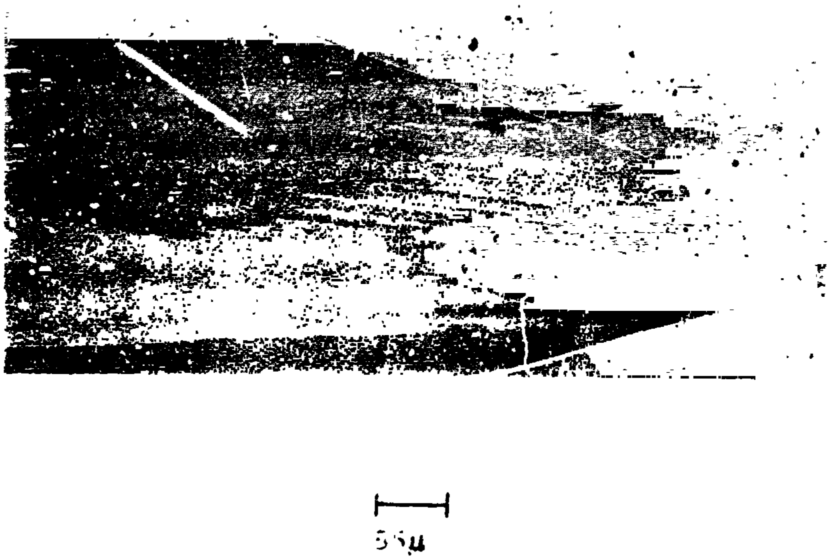

P78051615

Figure 17. METALLOGRAPH OF TYPE 304 SS IN THE MENISCUS REGION EXPOSED AT 530°C FOR 1250 HOURS (180 X)

parabolic [corrosion $\propto$ (time)$^{1/2}$]; thus a long-term corrosion rate much lower than 14 mils/yr can be expected. Compared with the observed corrosion in the meniscus area, the corrosion in the interior region was negligible. The observations confirm the differences in corrosion rates reported by Davis and Kinnibrugh[6] for submerged and partially submerged conditions.

Corrosion of aluminum honeycomb used as a conductivity promoter was observed in a terminated laboratory TES test that underwent 5 cycles between 550°C and room temperature. Because the total exposure time was less than 100 hours, the results are only tentative and cannot be extrapolated to predict long-term corrosion. However, an average corrosion of approximately 0.1 mil was measured.

In summary, 300-series stainless steels (e.g., Types 304 and 347) appear satisfactory under submerged conditions. A somewhat greater amount of corrosion was observed on Type 304 stainless steel in the meniscus region, but additional tests are necessary to obtain long-term corrosion rates in this region. Aluminum is an acceptable material, provided it is used in temperature ranges compatible with the desired mechanical properties.

Task 3. Construct, Operate, and Evaluate the Performance of the Engineering-Scale (8-kWhr$_{th}$) System

System Construction

Based on the design considerations discussed in conjunction with Figure 10, 3 engineering-scale units were constructed of 316 stainless steel. A cross section of one of the units is shown in Figure 18. The container is a Schedule 40 12-in.-diam pipe 18 in. long. The annular central tube, used for heating and cooling purposes, is a Schedule 40 2-in.-diam pipe approximately 24 in. long with welded flanges on both ends. The bottom of the container is a 1/4-in.-thick circular plate. Heli-arc welding was used to secure and seal the bottom plate to both pipes. The thermocouple wells were initially installed by drilling 1/8-in. holes in the container bottom at the appropriate locations, inserting the 1/8-in. tubes to the proper height, and welding around their base. However, this method was later found unsatisfactory due to leaks developing around the welds, and the method was modified. Direct welding of the thermocouple wells was avoided by using butt-weld tube fittings (GYROLOK), which were found to perform satisfactorily. The container lid and outer sealing ring were machined from 3/8-in. plate stock. Sealing of the center tube was accomplished with a flange tightened by eight machine screws. The outer tube was sealed with a two-bolt compression-type flange. Aluminum gaskets were used on both flange arrangements. Standard 2-in. MSS slip-on flanges were used to connect the unit to the TES system. A schematic of the TES system, comprised of the TES unit, an air blower, the heating element, the instrumentation, and the controls, is shown in Figure 19.

A three-station test stand was constructed, with cooling air supplied through 2-in.-diam piping manifolded to each station from a single source. Air flow was adjusted and regulated by a limiting orifice control valve placed in each of the coolant lines. The units were insulated with 7 in. of J-M Cerafelt mineral fiber. The insulation was applied in 1/2-in.-thick layers. Aluminum foil was placed between the layers to reduce radiation losses.

System Operation and Data Collection

The units were filled with approximately 130 lb of salt before mounting and insulation. Filling was accomplished by a two-step procedure. First, the container was filled with powdered $LiKCO_3$, placed in an oven, heated to 580°C in an air/CO_2 atmosphere, held at temperature for 16 hours and then cooled. This step was repeated three times, filling approximately 80% of the

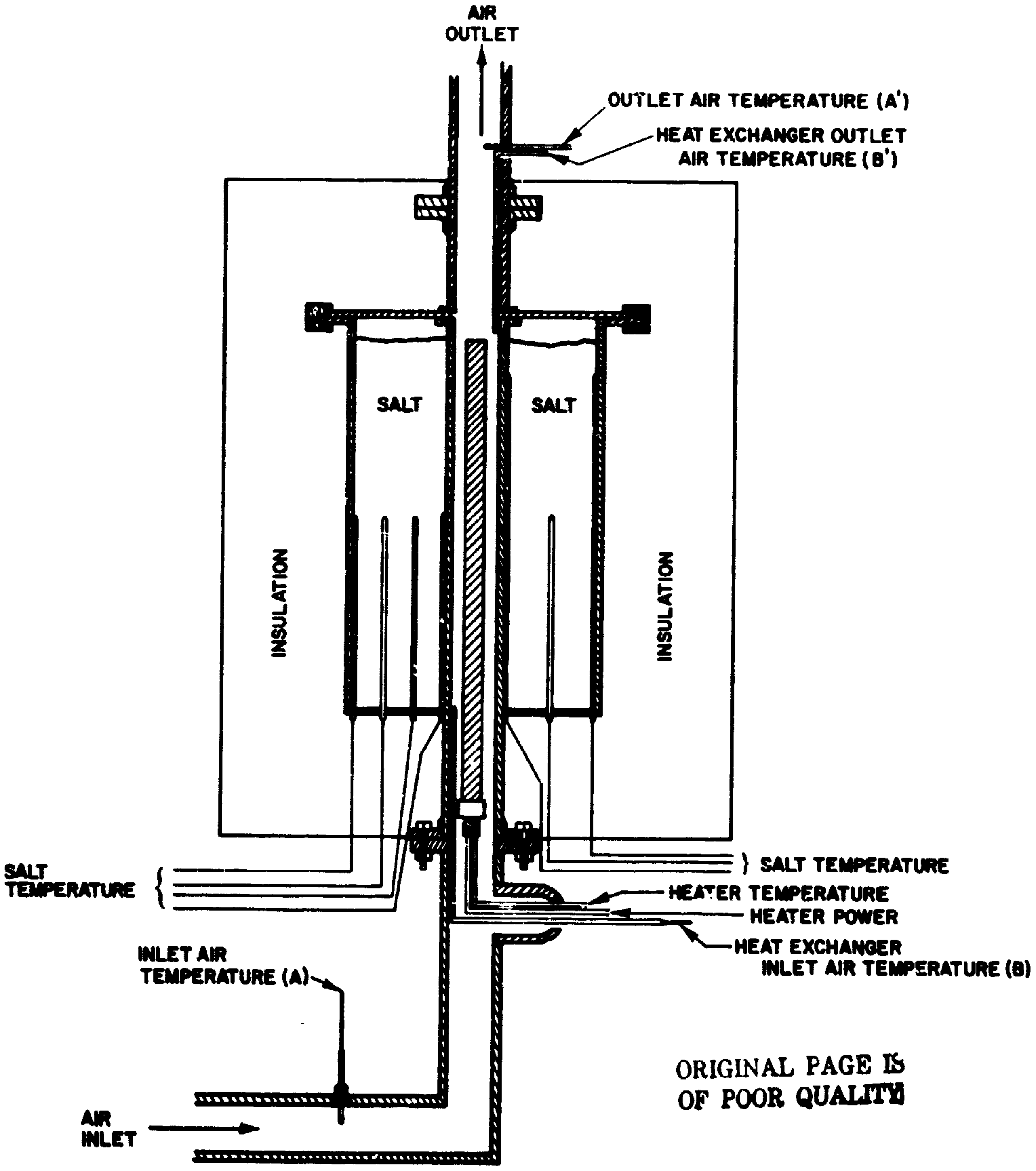

ORIGINAL PAGE IS
OF POOR QUALITY

A78030701

Figure 18. ENGINEERING-SCALE UNIT MOUNTED IN TESTING STATION

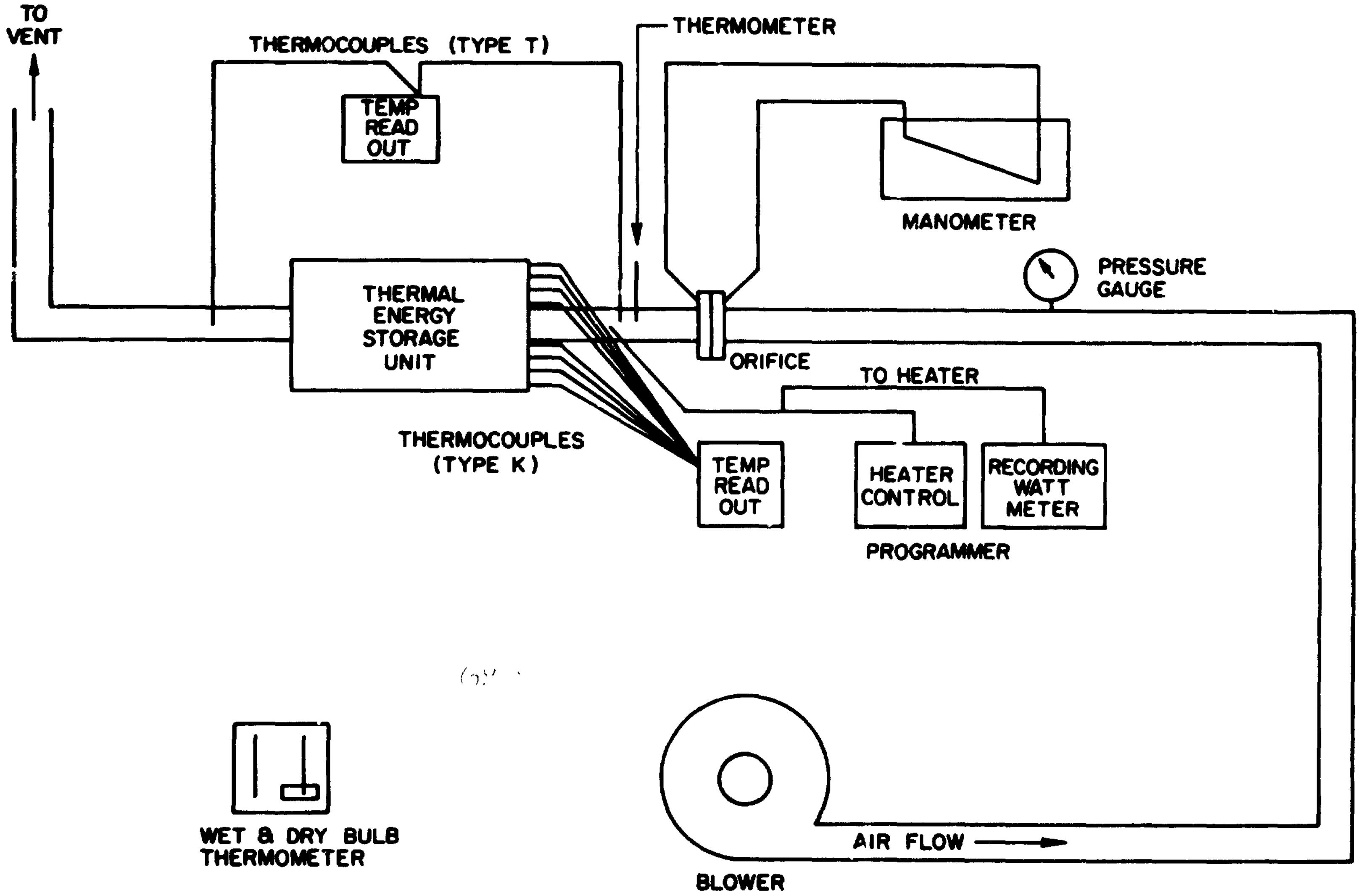

Figure 19. SCHEMATIC DIAGRAM OF THE ENGINEERING-SCALE THERMAL ENERGY STORAGE SYSTEM

container volume. The remaining salt was added by melting it in alumina crucibles, which were subsequently emptied into the container. The filled container was heated to 580°C and then cooled to room temperature.

The units were operated under varying cycle periods (a cycle consisting of charge, holding time, and discharge). The units were charged with a 3/4-in.-diam H-T firerod fixed in the center of the central tube. The heating rate was controlled with a programmable controller, and the power input measured with a time-base recording wattmeter. The units were heated to 530°C and held at this temperature for varying times depending on the cycle period.

The units were discharged with ambient air. Flow rates were determined using an orifice meter, inclined manometer, and an upstream static-pressure tap. Humidity of the air was measured by means of wet- and dry-bulb temperatures. The initial condition for a discharge run was for all thermocouples at salt mid-level to reach 530°C. At the termination of the holding period, power to the heating element was cut, air-temperature thermocouples were inserted where required, and air flow was directed to the station under operation. Air temperatures were recorded continuously on a two-pen strip-chart recorder, and salt temperatures were recorded on a 24-point strip-chart recorder throughout the cycle. Air flow rates were checked and recorded periodically throughout the discharge run and adjusted when necessary to maintain a constant mass flow rate of ~160 kg/hr (≈350 lb/hr).

The discharge run was ended when the slowest-cooling thermocouple at salt mid-level reached a temperature of 482°C.* When this condition was reached, air flow was shut off, air-temperature thermocouples removed, and charging begun.

The charging sub-cycle was controlled from a thermocouple located on the salt-side heat-transfer surface at salt mid-level. The charging program was designed to bring this location to the holding temperature, 530°C, in under an hour and therafter maintain this temperature throughout the charging period. A constant-temperature heat source, similar to that expected in commercial application, could therefore be simulated, allowing qualitative evaluation of

---

* Temperature profiles through the salt obtained during shakedown runs indicated that total solidification was achieved at a slightly higher temperature, 493°C, at the slowest cooling location.

ORIGINAL PAGE IS
OF POOR QUALITY

charging performance. The heater temperature was also recorded during charging in order to estimate the heat flux required to maintain this steady-state condition. Comparison with other temperature and flow requirements could then be made if alternate heat sources (such as high-temperature, high-pressure steam) were used for charging.

Performance Evaluation

Criteria for Performance Evaluation

Several factors must be considered in evaluating the performance of a TES system, each of which has a significant influence on the engineering and economic feasibility of latent-heat energy storage. Although standards for performance evaluation have been established for lower-temperature systems[11] (primarily for solar energy applications), standards are not yet available for high-temperature systems such as that being investigated here. As a result, the evaluation must be based on the factors most influential on the performance of a system in a specific application (such as utility load-leveling). Therefore, we have selected the following parameters to evaluate the performance of the TES system being studied:

- Average discharge heat flux over a discharge run.
- Variation in the discharge heat flux with time during a discharge run.
- Heat extraction efficiency — the percentage of the heat available to the transfer fluid for a given ΔT and salt mass that is extracted by the transfer fluid.
- Storage efficiency — the percentage of the charging energy recovered by the transfer fluid during a discharge run.
- System stability — variations in system and materials behavior resulting from thermal cycling.
- Cyclability, the capability of the system to be charged and discharged in the time period required as dictated by the anticipated duty cycles.

Although other factors related to system performance have been considered and will be discussed briefly, those mentioned above will provide a strong base for TES feasibility assessment and relative evaluation of design modifications (such as conductivity enhancement or alternate heat exchanger designs). Analysis and evaluation of system performance will be concentrated primarily on the discharge mode, because the discharge performance appears to be the determinant when the feasibility of commercial implementation is considered. This conclusion is drawn because the greatest barrier toward cost-effective system designs hinges on the ability to extract the stored energy in a time period which, for most TES applications of primary interest, will be significantly shorter than the time available for charging. Because the charging times are comparatively long and the initial formation of the higher-conductivity liquid phase occurs closest to the heat source during charging, the thermal conductivity of the solid salt (which is rate controlling during discharging) is a less significant factor during charging.

Evaluation of $LiKCO_3$ Without Conductivity Enhancement (Engineering Scale)

Two engineering-scale TES units were operated with $LiKCO_3$ as the PCM without any conductivity or heat exchange enhancement. The primary goals in operating these units were —

a. To establish and verify baseline performance characteristics for relative evaluation of alternate PCM, conductivity-promotion, and heat exchanger concepts.

b. To provide experimental verification of the mathematical heat-transfer models developed in Task 2.

c. To provide first-cut engineering data required for the design of prototype TES hardware.

The two units were operated for a combined total of 50 cycles representing over 2500 hours of operating time. Both units displayed comparable and reproducible performance, and their cooling behavior was in close agreement with that observed in the laboratory TES system and predicted by the heat-transfer model.

Heat fluxes were calculated from experimental data with the equation —

$$q = \dot{m} c_p \, \Delta t / A \tag{36}$$

ORIGINAL PAGE IS OF POOR QUALITY

where —

q = heat flux, kJ/hr-m^2 (Btu/hr-ft^2)

$\dot{m}$ = air mass flow rate, kg/hr (lb/hr)

c_p = heat capacity of the air, kJ/kg-°C (Btu/lb-°F)

Δt = air-temperature differential ($t_{out} - t_{in}$), °C (°F)

A = heat-transfer area, m^2 (ft^2)

The calculated heat flux is therefore directly proportional to the air-temperature differential. The locations at which the air temperature was measured in Unit 1 are shown in Figure 18 as A and A'. The temperature-measurement locations included B and B' in Unit 2, because the heat-transfer area used to calculate the heat flux in both units was defined as the portion of the central cooling tube in direct contact with the salt, i.e., length BB'. Average heat fluxes were calculated to be of the order 6000 Btu/hr-ft^2, using air-temperature measurements taken at A and A'. Similar calculations using air temperatures measured at B and B' in Unit 2 resulted in average heat fluxes of 4000 Btu/hr-ft^2.

The difference in heat fluxes determined from air-temperature measurements made at A and A' and B and B' could result from several factors:

a. Heat transfer occurring in the extended portions of the cooling tube. The heat available for transfer in these regions is that which is stored as sensible heat in the insulation, or that which can be drawn from the unit by conduction through the container walls, top, and bottom. The thermal conductivities of the insulation and steel, and the cross-sectional areas of the unit walls and cooling tube could allow enough heat to be transferred to the extended portions of the cooling tube to account for about two-thirds of the observed heat flux difference.

b. Different radiation effects on thermocouples. Temperature differentials measured between B and B' are not influenced by radiation, because thermocouples at these locations are affected equally by radiant heating. However, a thermocouple located at A' would indicate a temperature higher than the actual air temperature, due to radiant heating, whereas a thermocouple located at A would not be affected by radiation, because it is shielded by the coolant piping. Therefore, higher temperature differential would be measured between A and A'.

c. Inlet air temperature at B is measured with a Type K thermocouple (Chromel-Alumel). Type T thermocouples (copper-constantan), are used at A, A', and B' and are more accurate at lower temperatures. A Type K thermocouple had to be used at B because it remains in position during heating. A Type T thermocouple is not used because of the high temperatures reached (700°C) in the cooling tube during the heating period. Thermocouples located at A' and B' are not subjected to this heat because they are removed during the heating period.

Although each of the last two factors may only make a small difference in the temperatures recorded at the different locations, their combined effect could make a substantial difference in the calculated heat flux. This sensitivity of heat flux is a result of the TES unit design. The heat-transfer area in the heat exchanger portion of the cooling tube (B B') is small (< 1 ft^2), which results in a small air-temperature differential at the air flow rates being used. Temperature differences of 1°C measured between A and B, and B' and A' combined can result in up to a 20% difference in the calculated heat flux during the latter stages of the cooling sub-cycle. This effect is less pronounced (3% to 5%) during the early stages of the cooling sub-cycle when the Δt is large, but compounded over the entire cooling period it can result in substantial differences in the heat flux calculation.

Performance evaluation of Unit 1 is based on air-temperature measurements made only at locations A and A'. Efficiency and heat flux is therefore determined by heat transfer occurring in both the heat exchanger (of primary interest) and in the extended portions of the cooling tube.

The calculated heat flux will be based on the heat exchanger area (BB'), because the temperature distribution along the cooling tube sections away from the heat exchanger is not known. As a result, the heat flux reported for Unit 1 will be an apparent value and not the actual flux occurring in the heat exchanger. The actual heat flux could not be determined for Unit 1 because the appropriate air temperature information was not available. However, both the apparent and actual heat fluxes were determined in Unit 2, allowing verification of the performance observed in Unit 1 and providing accurate heat-transfer information for the TES system.

Unit 1 Performance – Heat Flux and Efficiency

The first engineering TES unit contained 130 lb of $LiKCO_3$ and was cycled 20 times. After the twentieth cycle, the unit was cooled to room temperature, the insulation removed, and the unit inspected. The outside surface of the container was oxidized in the typical fashion consistent with heating stainless steel to about 538°C in air, but no evidence of salt loss by creepage was visible. Slight vapor loss was apparent as indicated by discoloration of the insulation at the junction of the sealing flanges. The unit was only partially sealed with an aluminum gasket, and the low vapor losses observed show a significant advantage of this system over systems using fluorides[23,24] as phase-change materials, where hermetic sealing is required to prevent moisture absorption and vapor losses. A leak was also detected in the container bottom. The exact location of the leak could not be determined, but is strongly suspected to have occurred in the weld around the thermocouple well located near the cooling tube. Approximately 3.5 lb of salt was lost from the container by leakage. The leaks appear to have a self-sealing effect, i.e., as the salt spreads through the insulation it cools and solidifies, preventing more salt from escaping.

The container was opened to inspect the inner surfaces, particularly in the meniscus region where a higher corrosion is expected, and to obtain a salt sample for analysis. The solidified salt upper surface is shown in Figure 20.

P78041009

Figure 20. SOLIDIFIED SALT SURFACE OF TES CONTAINER NO. 1 AFTER 10 CYCLES

A cooling history of the salt can be approximated by examining the relative sizes of the salt crystals on the surface. Near the cooling tube the crystals are fine and numerous, and show a definite orientation with respect to the cooling tube. This type of growth pattern is the result of a very rapid cooling. Midway between the cooling tube and outer wall, the crystals are large and randomly oriented, resulting from a slower cooling. Near the outer edge, the crystals are again somewhat finer, but show no preferred orientation, indicating a cooling rate higher than in the middle, but much slower than that near the cooling tube. These observations are in correspondence with the temperature profile through the salt as a function of cooling time shown in Figure 21. The flat portion of this temperature profile through the still-molten salt also confirms the strong convective mixing effects observed in the pilot TES units.

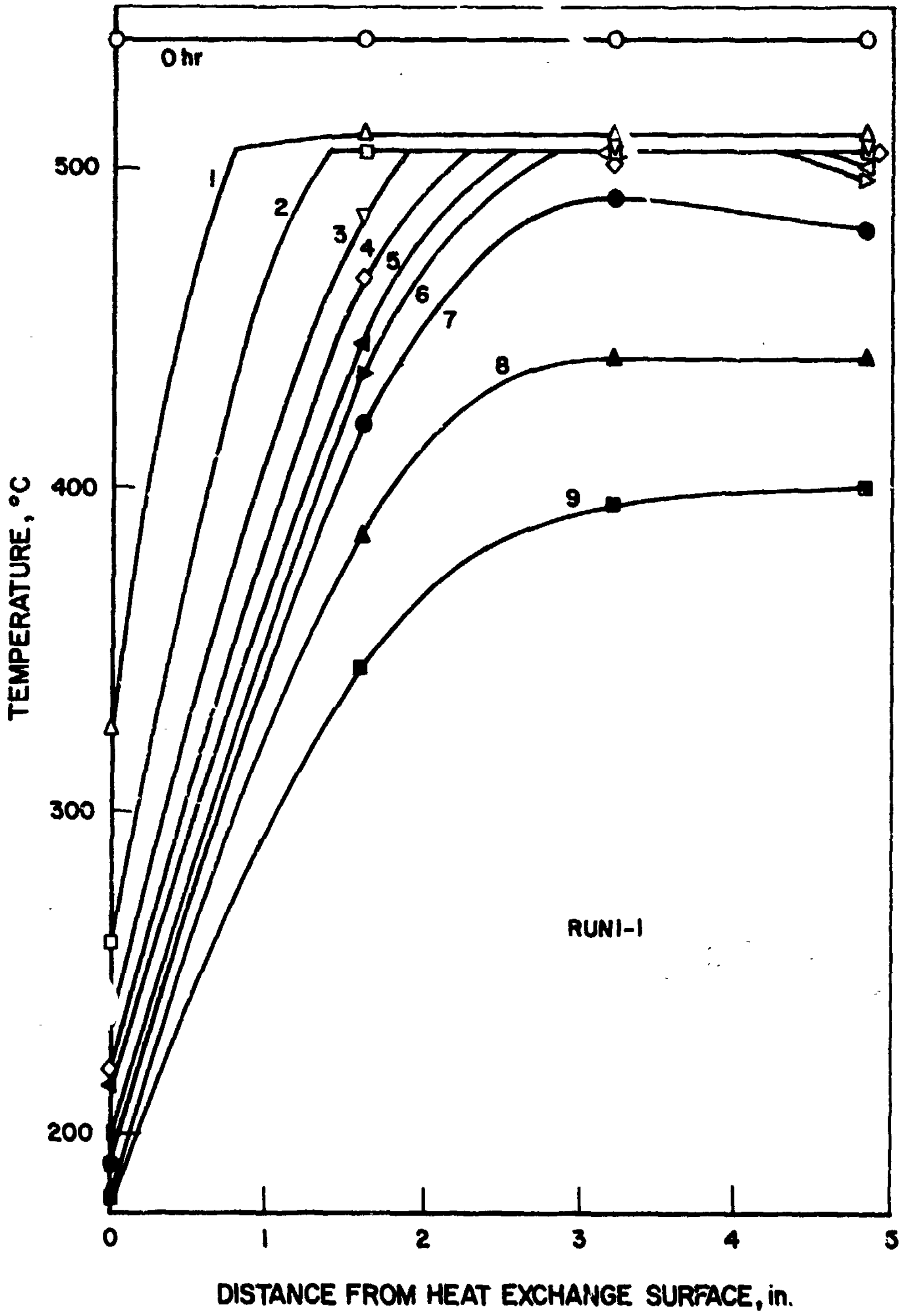

A78030720

Figure 21. TEMPERATURE PROFILE IN THE SALT AT HALF DEPTH DURING THE FIRST CYCLE

When a salt sample was removed, voids were found under the salt surface midway between the cooling tube and the outer wall of the container. It was therefore assumed that a solid "skin" formed on the surface of the molten salt due to heat losses through the insulation. The salt level dropped due to leakage exposing the variable-depth thermocouple wells. It was also observed that the wells were bent, giving further evidence that a solid "skin" forms on the upper salt surface during the earlier stages of cooling. If such a skin did begin to form, it was expected that the solids would settle through the liquid due to the density differences between the two phases. One of the primary reasons incongruently melting compositions were not selected for study was this anticipated phase separation due to sedimentation. However, if this phase separation does not occur when incongruently melting compositions are used as the PCM, the design implications would be strong. This would allow a wider range of compositions within a salt system to be acceptable for TES applications. Thermal energy would then be available over a temperature range (between the solidus and liquidus temperatures for the composition being used), which would allow "tailoring" of the PCM to fit the application and duty cycle of a TES system.

The temperature profiles obtained on cooling during cycles 1, 10, and 20 are shown in Figures 21, 22, and 23. When allowances are made for differences in the initial salt temperatures, three distinct trends as a function of cycle become apparent:

1. The average salt-side heat exchange surface temperature increases for the same cycle period.
2. The variation in the salt-side heat exchange surface temperature decreases for the same cycle period.
3. The salt temperatures at the two locations farthest from the heat exchange surface are substantially lowered for the same cycle period.

Each of these trends results from improved heat transfer both across the heat exchange surface and through the fused salt. The improved heat transfer across the heat exchange surface is brought about by the formation of an oxide corrosion layer on the salt side during cycling. The bonding of the salt to this layer upon solidification is stronger and more intimate than the bond developed between the salt and the uncorroded steel surface. The improved heat transfer through the salt is most likely a result of the elimination of randomly dispersed voids during solidification resulting from controlled cooling.

ORIGINAL PAGE IS OF POOR QUALITY

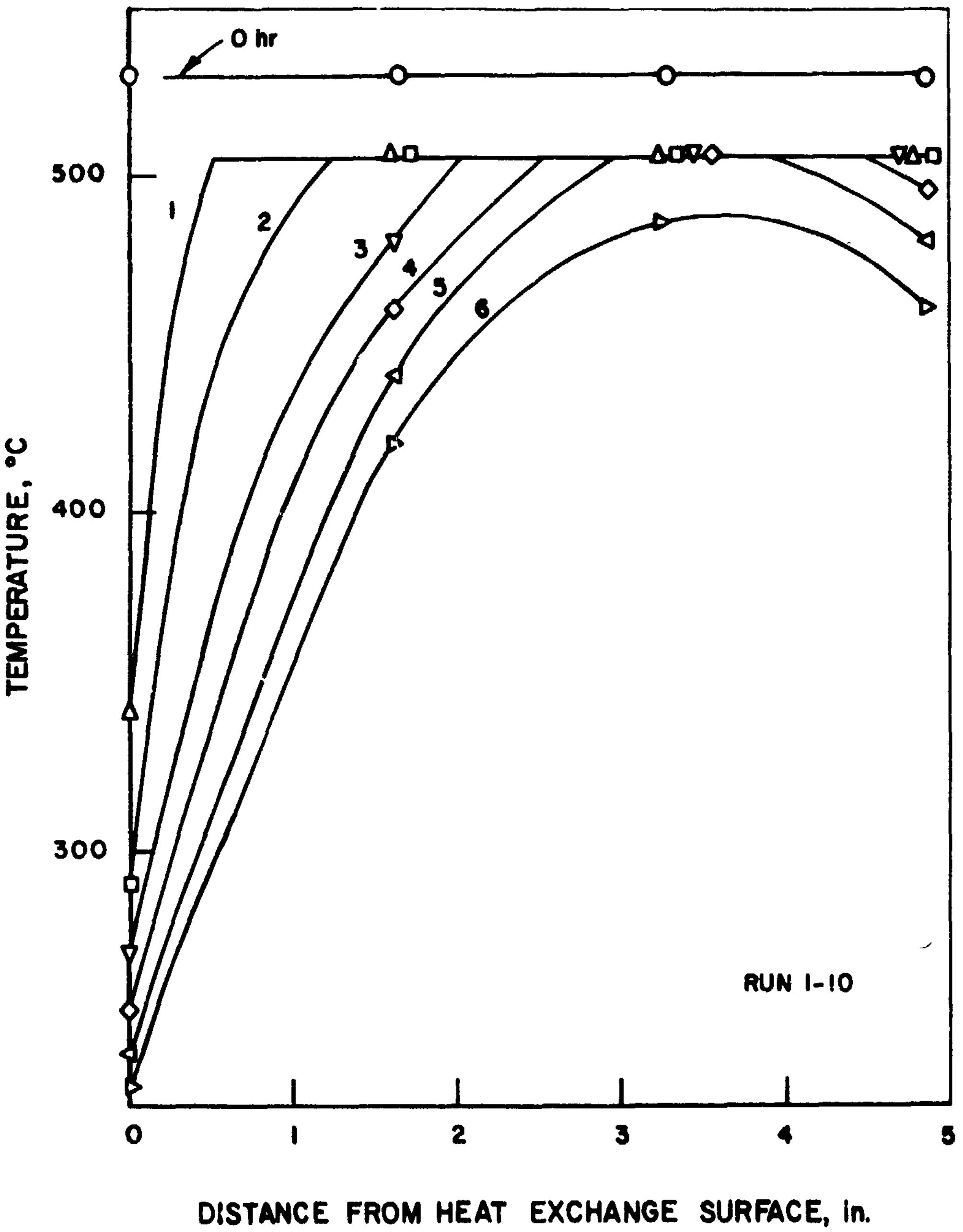

A78030704

Figure 22. TEMPERATURE PROFILE IN THE SALT AT HALF DEPTH DURING THE TENTH CYCLE

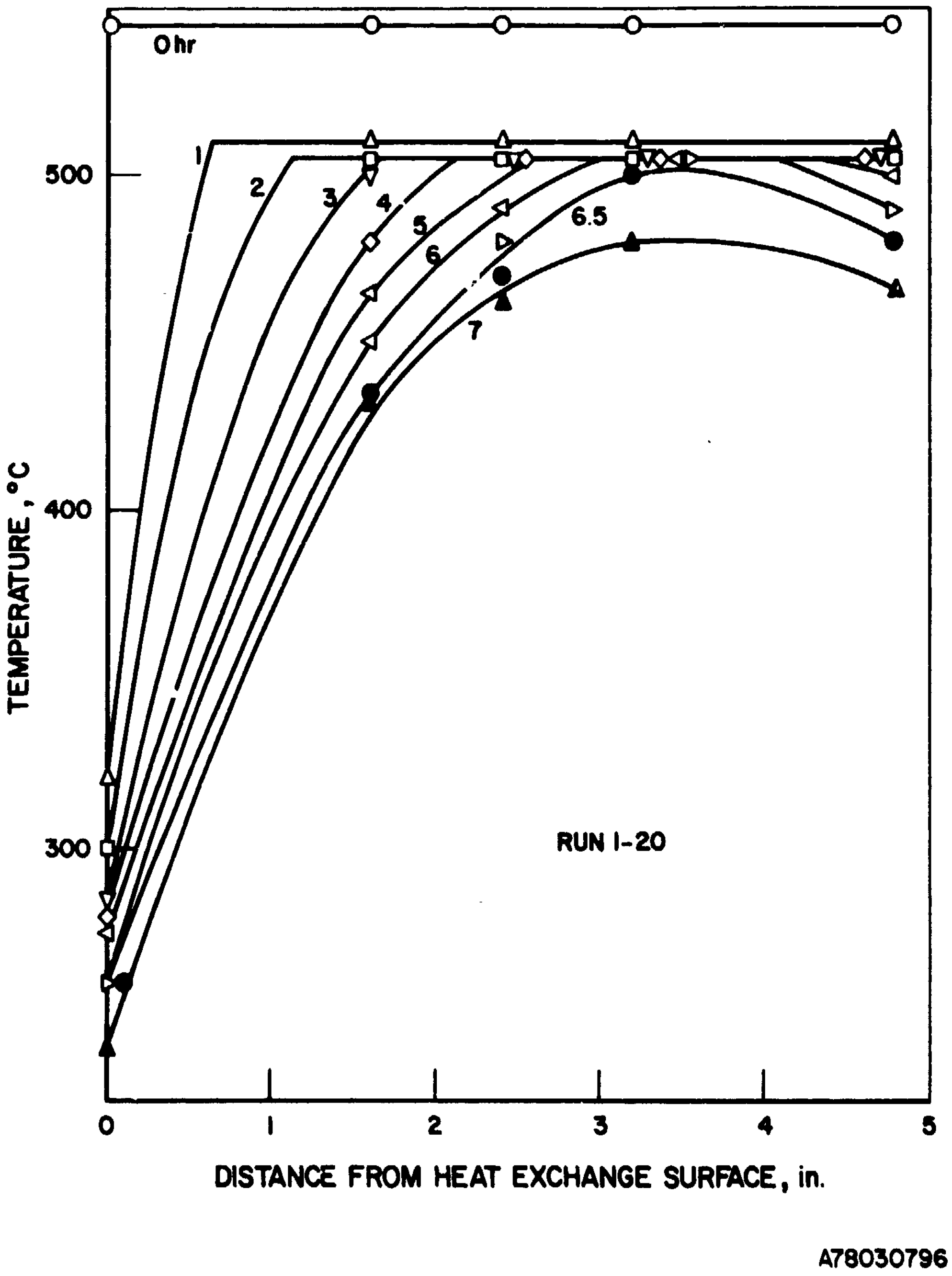

Figure 23. TEMPERATURE PROFILE IN THE SALT AT HALF DEPTH DURING THE TWENTIETH CYCLE

The results of these changes in system thermal behavior are that —

a. More thermal energy is extracted during a given cycle period,

b. Heat is available at a more constant temperature, and

c. Heat is available at a higher temperature.

These results are manifested as overall higher heat fluxes during operation and can be seen qualitatively by examining the coolant differential temperature ($t_{out} - t_{in}$) during different cycles for a constant coolant flow rate. A 5% to 20% increase in the temperature differential is seen between cycles 1 and 10, but there is only slight variation between cycles 10, 15, and 20. We concluded from these results that system equilibration occurred during the first 10 cycles, representing approximately 250 hours of contact between the heat exchange surface and the molten salt.

The performance observed during the tenth cycle, which is representative of Unit 1, is summarized in Table 6.

Table 6. REPRESENTATIVE THERMAL PERFORMANCE OF TES UNIT 1

			Cycle 10
Heat Flow, Btu			
Sensible Heat Removed From the Liquid			2,820
Heat of Fusion Removed			19,240
Sensible Heat Removed From the Solid			4,740
Total Heat Extracted From the Salt			26,800
Sensible Heat Removed From the Container			2,100
Sensible Heat Removed From the Insulation			1,000
Total Heat Lost by the System			29,900
Heat Extracted by the Coolant Air			24,260
Heat Lost to the Ambient			5,640
Charging Energy (Above Ambient Heat Loss),	Btu	=	31,100
	kWe		9.11
Total Energy Input (Charging and Holding),	Btu	=	53,425
	kWe		15.64
Heat Extraction Efficiency, %		=	81
Storage Efficiency (Based on Charging Energy), %		=	78
Storage Efficiency (Based on Total Input), %		=	45
Average Heat Flux, Btu/hr-ft^2		=	6,100

The heat lost to the ambient during discharge corresponds closely to the power drawn during the holding period of the charging sub-cycle (time during which the molten salt is held at a constant temperature, 530°C). This input power demand results from heat loss from the charged unit. Distributing the heat loss (5640 Btu) evenly over the discharge period (5 hr, 20 min) yields an electrical equivalent of 310 watts. The observed power drawn during the holding period varied between 325 and 350 watts.

The storage efficiency here is determined from two values of the energy input to the system. The first, termed the charging energy, consists of all energy input above the ambient heat loss level as determined by the power drawn during the holding period. This is shown schematically in Figure 24 as the shaded portion under the power input curve. The second, termed the total energy input, consists of the charging energy and the heat loss during both the charging and holding periods. This is shown in Figure 24 as the total area under the power input curve (shaded area + crosshatched area). The storage efficiency based on the charging energy is 78%, whereas that based on the total energy input is only 45%. The efficiency based on the total energy input is of primary interest for commercial units, but the value derived here on that basis is not a valid approximation applicable to larger units. This results from the container size and geometry, and the cycle characteristics, as discussed below.

To evaluate the efficiency of the engineering-scale unit on the basis of total energy input is misleading because the ratio of the total surface area of the insulated unit to the volume of the unit is very large. The effect of scale and container geometry on the efficiency can readily be seen from the heat loss information generated from this unit. The observed heat loss to the ambient during the 5.33-hr discharge period totaled 5640 Btu. The total surface area of the insulated container is 25.5 ft^2. This leads to a heat loss rate of 42 Btu/hr-ft^2. Assuming this loss rate to remain constant for the insulation and thickness used, regardless of container size, leads to a total loss during a 24-hr operating period of —

$$\text{ENERGY LOSS} = (42\ \text{Btu/hr-ft}^2)(24\ \text{hr})(A) \qquad (37)$$

where A = total surface area of the insulated container.

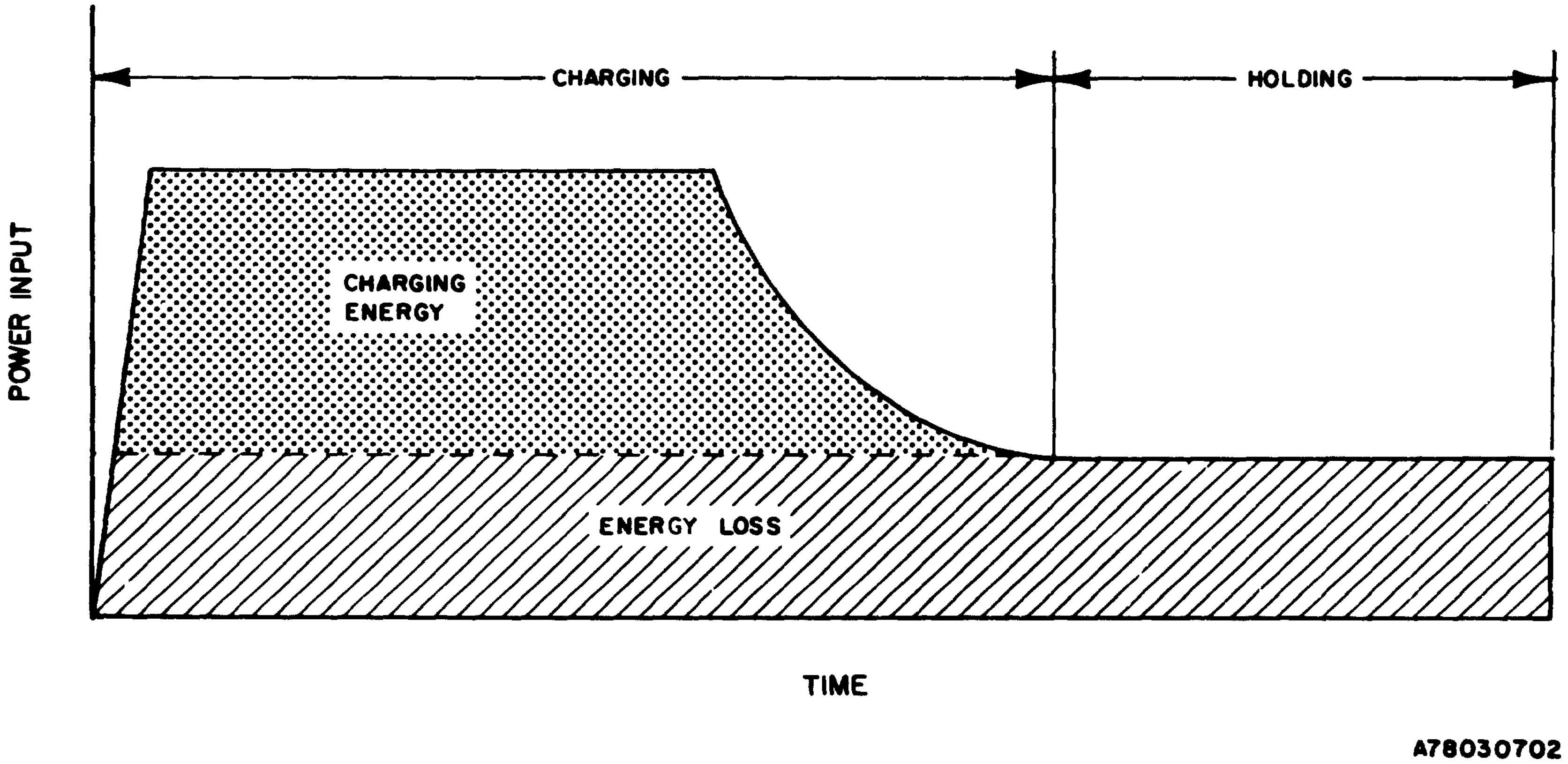

Figure 24. SCHEMATIC ENERGY INPUT PROFILE DURING CHARGING AND HOLDING OF AN ENGINEERING-SCALE TES SYSTEM

ORIGINAL PAGE IS
OF POOR QUALITY

The capacity of a storage unit can be determined from the volume of the PCM, its density, and its heat of fusion by the equation —

$$\text{CAPACITY} = \rho_o \Delta H_f V_s \tag{38}$$

where —

ρ_o = density of the PCM

ΔH_f = heat of fusion of the PCM

V_s = volume of salt

If it is further assumed that some fraction, f_s, of the container volume, V_c, is occupied by the molten PCM, and the remaining volume by heat exchangers and/or void space, Equation 38 becomes —

$$\text{CAPACITY} = V_c \rho_o \Delta H_f f_s \tag{39}$$

The heat loss can then be determined as a percentage of the storage capacity by taking the ratio of Equation 37 to Equation 39:

$$\begin{aligned} \%\ \text{LOSS} &= \frac{\text{ENERGY LOSS}}{\text{CAPACITY}} \times 100 \\ &= \frac{(42\ \text{Btu/hr-ft}^2)(24\ \text{hr})}{(V_c)(\rho_o)(\Delta H_f)f_s} (A) \times 100 \end{aligned} \tag{40}$$

Substituting appropriate values for the experimental PCM (LiKCO$_3$; $\rho_{986°F}$ 128.2 lb/ft^3, ΔH_f = 148 Btu/lb), Equation 40 becomes —

$$\%\ \text{LOSS} = \left(\frac{5.3}{f_s}\right)\left(\frac{A}{V_c}\right) \tag{41}$$

It can be readily seen from Equation 41 that for any given f_s, the % loss during a 24-hr period is directly proportional to the ratio of the surface area to the container volume. The value of V_s for the engineering-scale TES units is 0.83 with V_c = 1.18 ft^3 and A = 25.5 ft^2. The ratio of (A/V_c) = 21.6, and the % loss = $\left(\frac{5.3}{0.83}\right)(21.6)$ = 138%.

The effects of scale on the heat loss are shown in Figure 25. For this diagram, the heat loss during a 24-hr operating period was determined from Equation 41 for storage units with a height-to-radius ratio equal to that of the engineering-scale unit tested here, but with varying radii and with V_s = 0.75. Doubling the size of the container (1-ft radius, 3-ft height) decreases the proportion of capacity lost to about 40%. In the capacity range of commercial interst (1-100 MWhr$_{th}$), this value is reduced to below 10%.

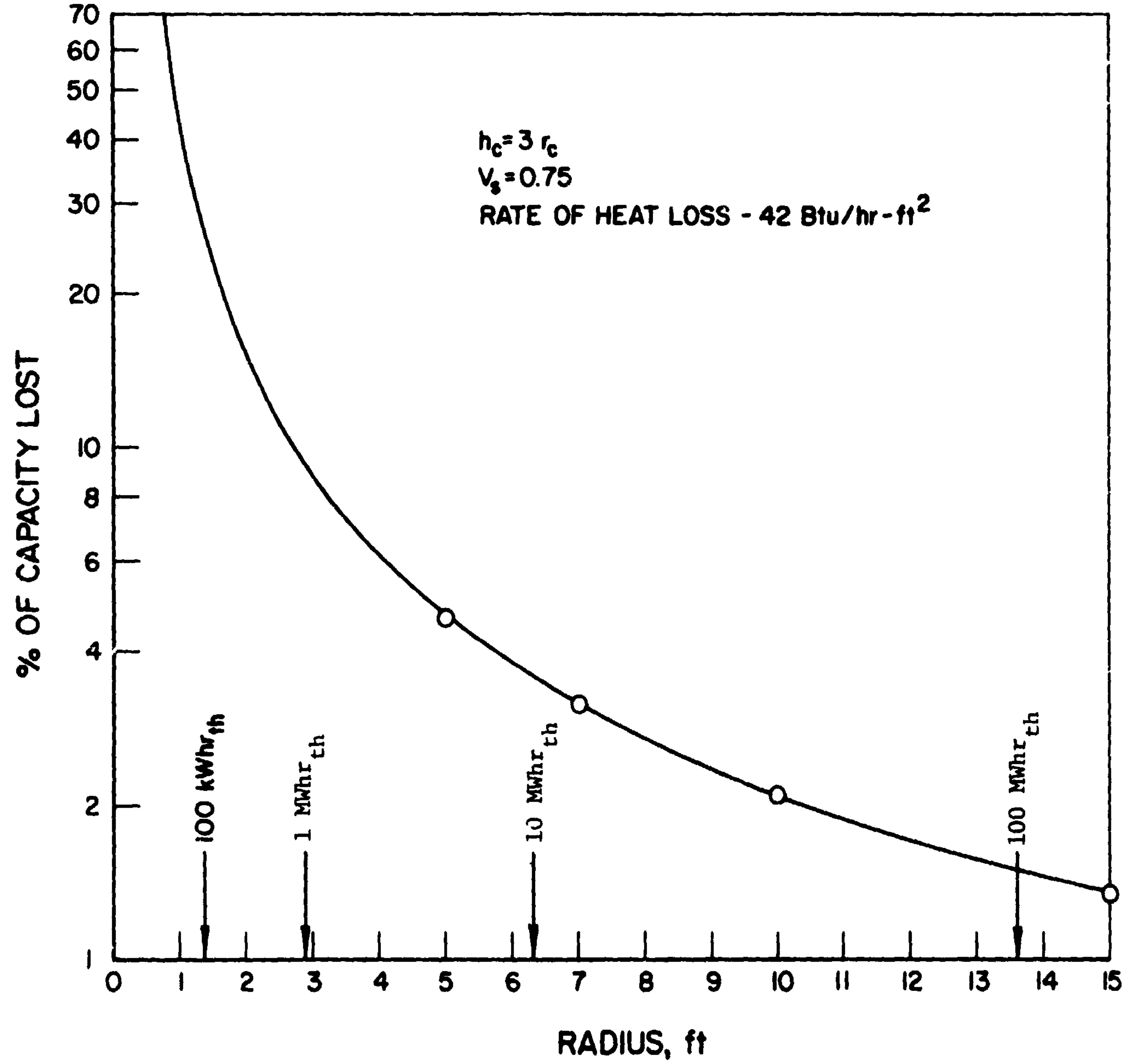

Figure 25. HEAT LOSS DURING A 24-hour OPERATING PERIOD FOR LARGER TES UNITS

As a result of the strong dependence of efficiency on scale, it would be erroneous to judge the performance of a larger-scale unit based on the efficiency found for the engineering-scale unit, if the total energy input is considered. Therefore, efficiencies of other units will be based on the charging energy only. Although this method of evaluation does not consider the heat loss during charging and holding periods, it will still give a conservative approximation of the storage efficiency because the high loss rate is maintained during discharging, thereby limiting the energy recoverable by the heat-transfer medium.

The performance curve obtained from Run 1-20 is shown in Figure 26. One of the primary reasons heat-of-fusion TES is advantageous is that the stored energy is theoretically available at a constant temperature — the PCM melting point. As a result, the temperature differential between the PCM and the heat-transfer fluid would remain relatively constant; and if the mass flow rate and input temperature of the working fluid did not change significantly, the heat flux would remain at or near a constant value throughout the discharge period. The resulting performance curve would, therefore, appear flat. As can be seen from Figure 26, the heat flux decreases from 12,000 Btu/hr-ft^2 at 5 min, to 7000 Btu/hr-ft^2 at 60 min discharge time. The rapid decrease results from the thermal conduction barrier imposed as the salt solidifies on the heat-transfer surface and increases in thickness. The sensitivity of the heat flux on the solid-salt thickness can be examined from Figure 26 and the cooling data obtained at locations 2, 3, and 7* that are summarized in Table 7 from Run 1-20.

Table 7. SUMMARY OF COOLING BEHAVIOR AT LOCATIONS 2, 3, and 7 DURING RUN 1-20

Location	Salt Thickness, in.	Time to Solidify, min	Q, Btu/hr-ft^2 (From Figure 26)
3	1.6	126	5700
7	2.4	200	4900
2	3.2	320	4100

---

* These locations are used because they represent 3 different radial locations isolated from "edge effects" such as heat loss to the ambient.

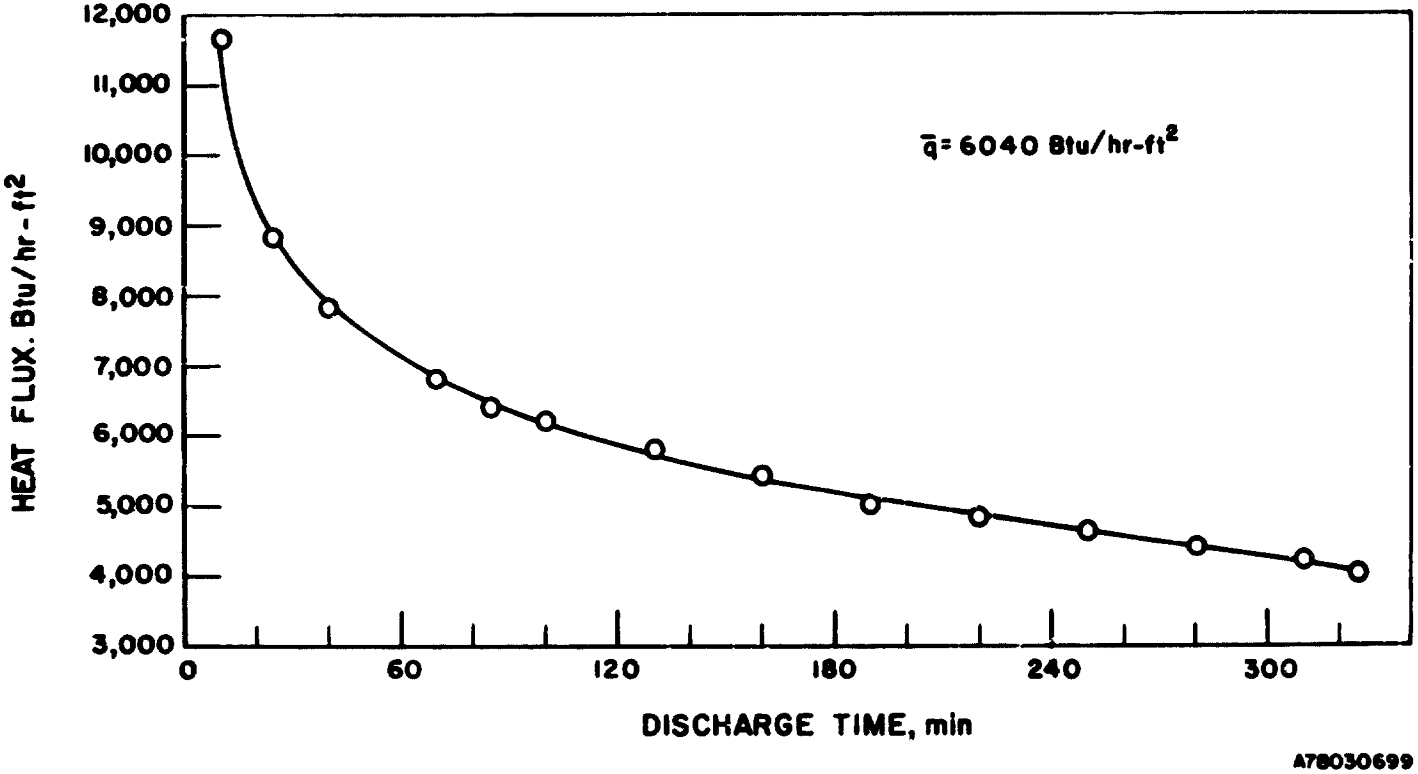

Figure 26. PERFORMANCE OF UNIT 1 (Run 1-20)

ORIGINAL PAGE IS
OF POOR QUALITY

The heat flux is shown in Figure 27 as a function of solid-salt thickness, and shows a linear relationship. The slope of the line shows a decrease in the heat flux of 1000 Btu/hr-ft^2 per inch solid salt. Although the relationship holds true after two hours of cooling, it does not appear accurate during the earlier stages of discharging. Extrapolating to time = 0 would indicate a heat flux of 7300 Btu/hr-ft^2. The observed value, which is > 12,000 Btu/hr-ft^2, indicates an even higher sensitivity during the initial cooling period. These results indicate strongly the need for conductivity enhancement or the development of active heat exchangers. If the performance curve cannot be flattened by one of these methods, steady-state heat transfer can only be achieved by varying the working fluid flow rates or entering temperature, which would lead to more complex and expensive system design.

After establishing baseline performance characteristics, the first unit was operated above the design temperature to evaluate its influence on performance. Operating from a higher starting temperature may be advantageous because of the further utilization of the sensible heat storage capacity of molten salt and the subsequent increase in system capacity. Broadening the system operating temperature range without altering performance would also make the system more compatible with variations in the duty cycle or the amount of energy available for storage. Run 1-15 was initiated from a starting salt temperature of 575°C, approximately 45°C above the design temperature. The storage capacity was increased by about 3400 Btu, or about 12.5%. The performance curve obtained is shown in Figure 28, with the performance curve from Run 1-20 operated from the design temperature for comparison. Operating from the higher temperature resulted in an increase in the discharge heat flux during the first 85 minutes of discharging, after which the performance appears nearly identical to that when the system is operated from the design temperature.

During the first 85 minutes most of the heat removed is sensible; therefore the solid-salt thickness increases only slightly due to latent heat removal. As a result higher heat fluxes are obtained because of the larger driving force due to the higher temperature differential (between the salt and the heat exchange fluid) and a lower resistance due to a thinner solidified salt layer on the salt side of the heat exchanger tube.

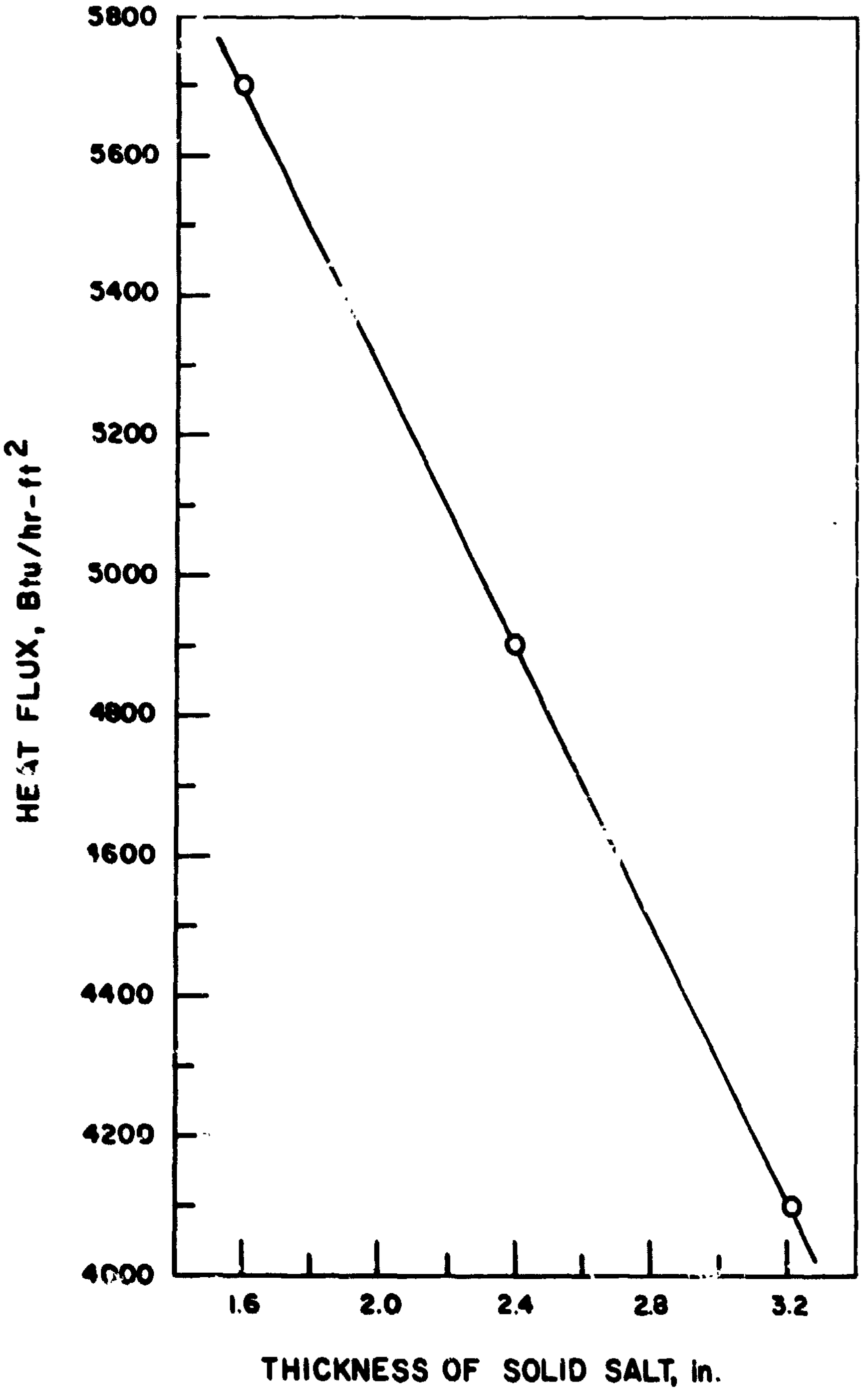

A78030703

Figure 27. INFLUENCE OF SALT THICKNESS ON HEAT FLUX

ORIGINAL PAGE IS OF POOR QUALITY

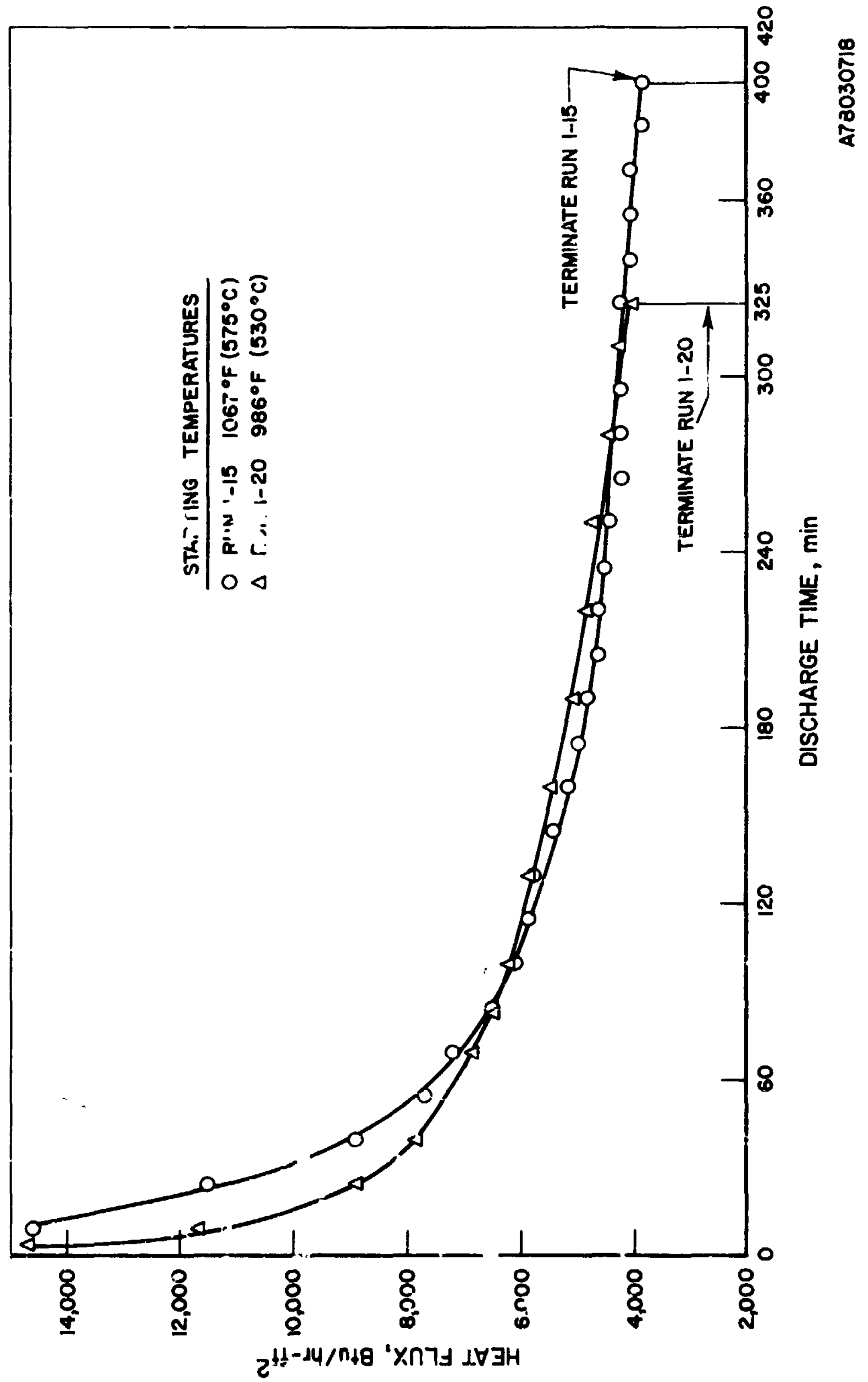

Figure 28. OPERATION AT AND ABOVE DESIGN TEMPERATURE

This hypothesis seems to be supported by the duration of the enhanced heat flux observed in Run 1-15. After 90 minutes of discharging, the molten salt has been cooled to a uniform temperature of 505°C, the melting point. The heat flux enhancement disappears after about 85 minutes of discharging.

The concept that sensible heat "displaces" latent heat and subsequently inhibits interfacial movement during cooling is also supported by these results. Both runs were terminated when nearly identical thermal conditions through the salt were reached. As can be seen in Figure 28, an additional 75 minutes was required in Run 1-15. Since the same amount of energy was extracted in the form of latent heat and sensible heat removed from the solid, the difference in discharge times results from the different quantities of sensible heat stored in the liquid phases. If this "excess" sensible heat delays the removal of latent heat until the end of the cycle, it would be evidenced by a longer discharge time, which is calculable. The heat flux after 325 minutes of discharging (the time required to discharge the unit, starting from the design temperature) is about 4100 Btu/hr-ft^2, which corresponds to energy removal at the rate of —

$$(4100\ \text{Btu/hr-ft}^2)(0.72\ \text{ft}^2) = 2950\ \text{Btu/hr} \qquad (42)$$

The additional 3400 Btu of excess sensible heat in the form of latent heat would require —

$$(3400\ \text{Btu})/(2950\ \text{Btu/hr}) = 1.15\ \text{hr} \qquad (43)$$

or 69 min to be removed. This value agrees well with the 75 min observed.

ORIGINAL PAGE IS
OF POOR QUALITY

Unit 1 Stability and Cyclability

The first unit was in operation for a total of 1100 hours; and although this is a short period with respect to desired system lifetimes (> 44,000 hr), the performance stability observed is encouraging. The effect on the average discharge heat flux of passing through the 20 cycles completed with this unit is shown in Figure 29. As observed in the laboratory unit (discussed under Task 2), the heat flux appears to increase during the initial cycling, but remains relatively constant after 7 cycles have been completed. This effect most likely results from enhanced contact between the salt and the salt-side heat-transfer surface brought about by slight oxidation of the heat-transfer surface during operation. After the completion of 7 cycles, the time required to discharge the unit also stabilized to an average of 5 hours and 40 minutes.

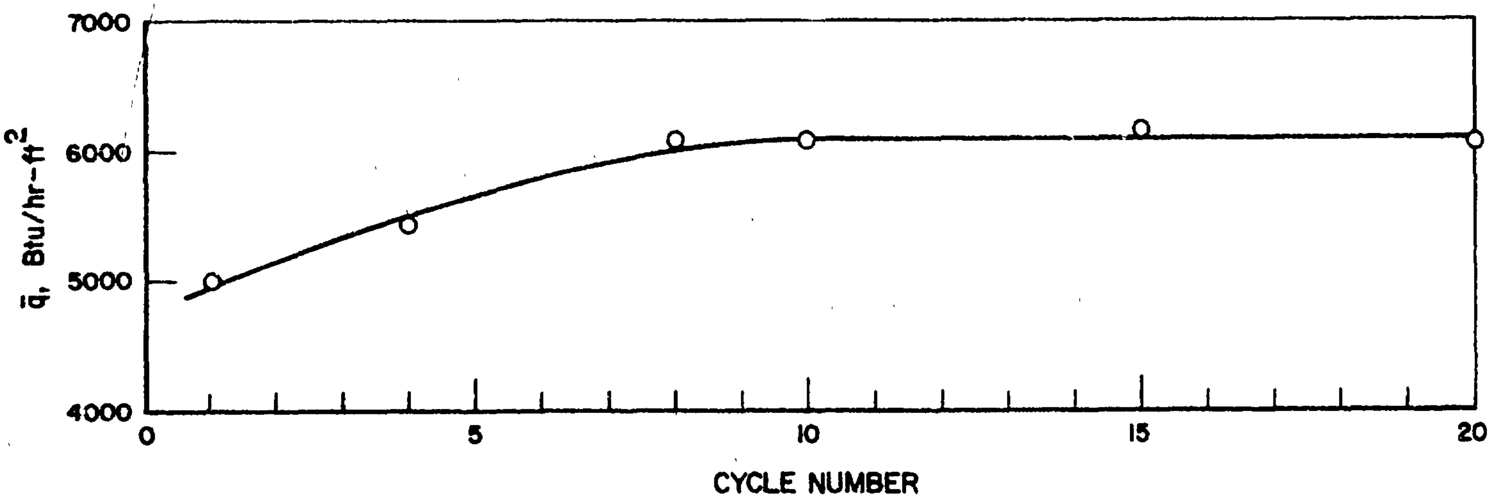

A78030713

Figure 29. UNIT 1 STABILIZATION

The discharge time varied by no more than 20 minutes during the remaining 12 runs, when the system was operated from the design temperature.

Chemical analysis, DTA, and DSC tests on the salt after the twentieth cycle showed no signs of degradation of the salt properties. The salt composition, melting point, and heat of fusion remained constant during the operating period. It is interesting to note that the salt showed discoloration due to corrosion products after the salt filling and shakedown runs, but this was not evidenced in the salt removed from the unit after the twentieth cycle. This observation is important in that it indicates passivation of the container inner surfaces in a relatively short period of time.

The system was readily cyclable in a 24-hour period. Full charging, accomplished in 8 hours, required an average charging flux of about 5450 Btu/hr-ft^2 (based on the charging power). A charging flux of about 3800 Btu/hr-ft^2 was required for a 12-hour charge.

Increasing the holding time did not appear to affect the performance, indicating a good adaptability of the system to variations in duty cycles.

Unit 2 Performance — Heat Flux and Efficiency

Unit 2 is essentially a duplicate of the first unit, but incorporates improvements in temperature measurement and insulating techniques. The primary purpose for operation was to verify the system performance characteristics observed in the first unit and to study the heat exchanger performance in greater detail. The unit was operated in the same manner as Unit 1, but was discharged using higher coolant flow rates. A total of 30 cycles were completed, representing 1400 hours of operation. Cycle periods were varied by increasing holding and charging times, and the unit was discharged from both initially fully charged and undercharged states. Stable performance comparable to that of Unit 1 was observed under all of the operating conditions. The system yielded average discharge fluxes of 6300 Btu/hr-ft^2 with system efficiencies of 75% to 85% with air temperatures measured at A and A' (Figure 18). However, when air temperatures were measured at B and B', the heat flux was found to be about 4000 Btu/hr-ft^2, which more accurately describes the heat exchanger performance. Strong convective mixing, which was also observed during discharging, enhanced the heat-transfer rates during the initial discharging periods. Detailed discussion of these results follows.

To verify the performance observed in the first engineering-scale unit, several discharge runs were made on the second unit, with inlet and outlet coolant temperatures recorded at locations away from the system (A and A' in Figure 18) as was done with the first unit. Run 2-20 is representative of the observed performance and is summarized in Table 8. The designation indicates that Unit 2 was operated for 20 cycles.

Table 8. "APPARENT" THERMAL PERFORMANCE OF TES UNIT 2

	Run 2-20
Heat Flow, Btu	
Sensible Heat Removed From the Liquid	2,457
Heat of Fusion Removed	18,944
Sensible Heat Removed From the Solid	4,220
Total Heat Extracted From the Salt	25,621
Sensible Heat Removed From the Container	2,100
Sensible Heat Removed From the Insulation	1,100
Total Heat Lost by the System	28,821
Heat Extracted by the Coolant Air	24,550
Heat Lost to the Ambient	4,271
Charging Energy, Btu	30,260
kWhr$_e$	8.86
Heat Extraction Efficiency, %	85
Storage Efficiency, %	81

The performance curves of Runs 1-10 and 2-20, based on air-temperature measurements made at A and A' in both units, are shown in Figure 30. The average heat fluxes were determined from graphical integration to be 6300 Btu/hr-ft^2 for Run 2-20 and 6080 Btu/hr-ft^2 for Run 1-10. The difference between the heat fluxes for these runs can be accounted for by the difference in flow rates. Unit 2 was operated with an average air flow rate of 355 lb/hr, approximately 7% higher than the flow rates used in Unit 1. Theory predicts a 4.5% increase in heat flux with a 7% increase in the flow rate. The observed difference, 3.6%, agrees well with the predicted value and indicates that performance is affected by the flow rates being used for testing. The higher observed efficiencies result primarily from better insulation of the second unit, which decreases the heat loss during discharging. However, we concluded from the close agreement in heat flux between Units 1 and 2 that the observed performance is reproducible.

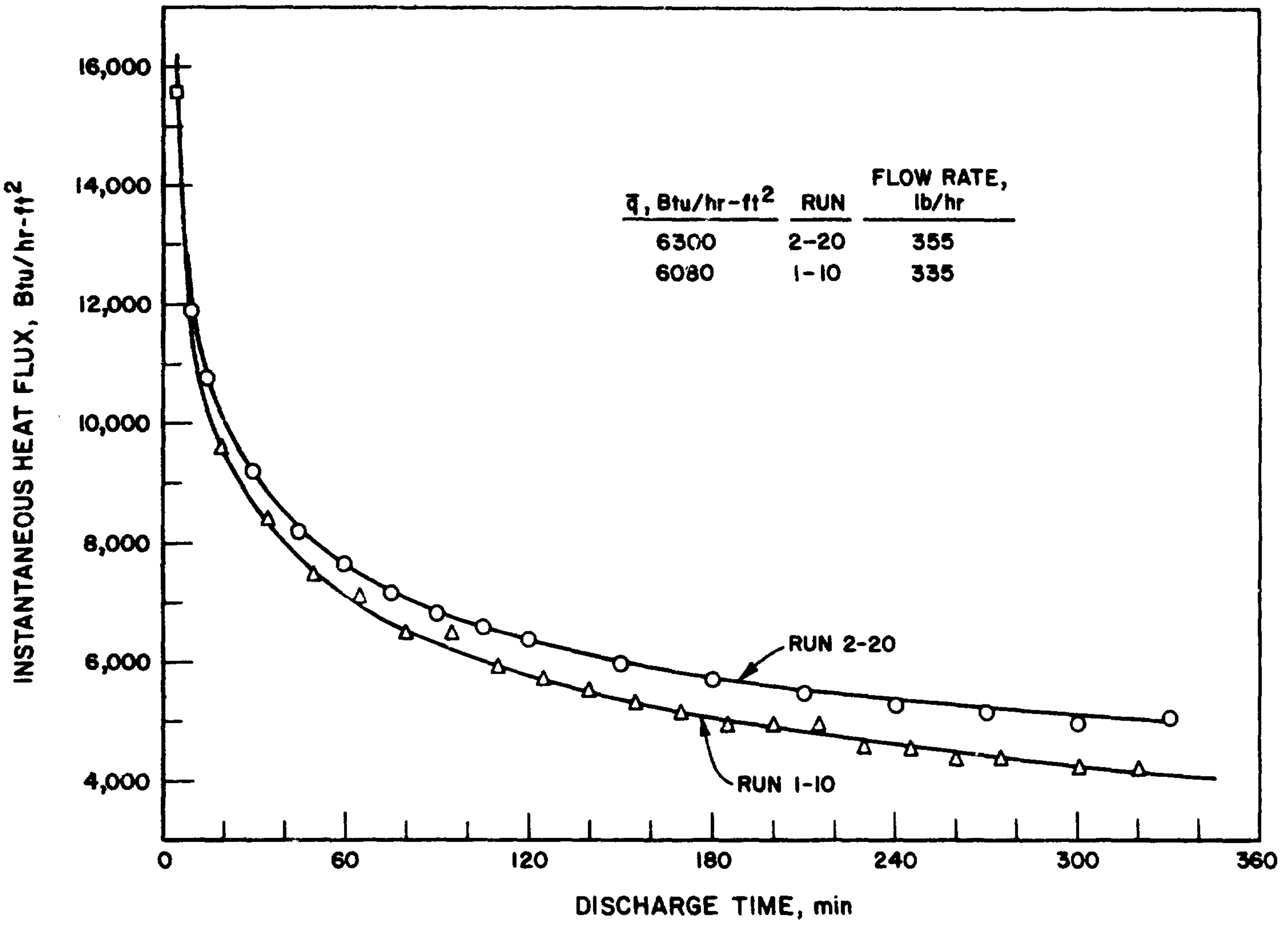

A78030716

Figure 30. PERFORMANCE COMPARISON BETWEEN UNITS 1 AND 2; AIR TEMPERATURES MEASURED AT A AND A' ("Apparent" Performance)

As previously mentioned, the performance discussed above is an "apparent" performance for the system. Although the values derived here are valid for comparison between the first two units, they do not represent the true performance. A better evaluation is obtained by measuring the coolant temperatures at the inlet and outlet of the heat exchanger (B and B' in Figure 18).

The height of the molten salt was determined by an electrical conductivity method developed at IGT to verify the heat-transfer area used in the heat flux determination and to determine the precise locations for the outlet thermocouples. The measured salt height was found to agree within 1% of the value predicted from density-temperature relationships[26] and the thermal expansion properties of the containment materials, and the outlet thermocouples were located accordingly.

Several runs from Unit 2 that were analyzed on this basis showed average heat fluxes varying over a narrow range between runs. The performance curves for two consecutive runs, which were made on a fully charged unit (2-15) and a partially charged unit (2-16), are shown in Figure 31. Run 2-15 results, representative of Unit 2 performance, are shown in Table 9.

Table 9. REPRESENTATIVE THERMAL PERFORMANCE OF TES UNIT 2

	Run 2-15
Heat Flow, Btu	
Sensible Heat Removed From the Liquid	2,312
Heat of Fusion Removed	18,944
Sensible Heat Removed From the Solid	3,727
Total Heat Extracted From the Salt	24,983
Sensible Heat Removed From the Container	2,000
Sensible Heat Removed From the Insulation	1,050
Total Heat Lost by the System	28,033
Heat Extracted by the Coolant Air	15,191
Charging Energy, Btu	30,600
kWhr_e	8.96
Heat Extraction Efficiency (Heat Exchanger Only), %	54
Storage Efficiency (Heat Exchanger Only),%	50

The overall average heat flux for this run was determined by graphical integration from Figure 31 to be 4024 Btu/hr-ft^2.

The efficiency evaluation is complicated by the heat transfer that occurs in the extended portions of the cooling tubes. When an energy balance is made

ORIGINAL PAGE IS
OF POOR QUALITY

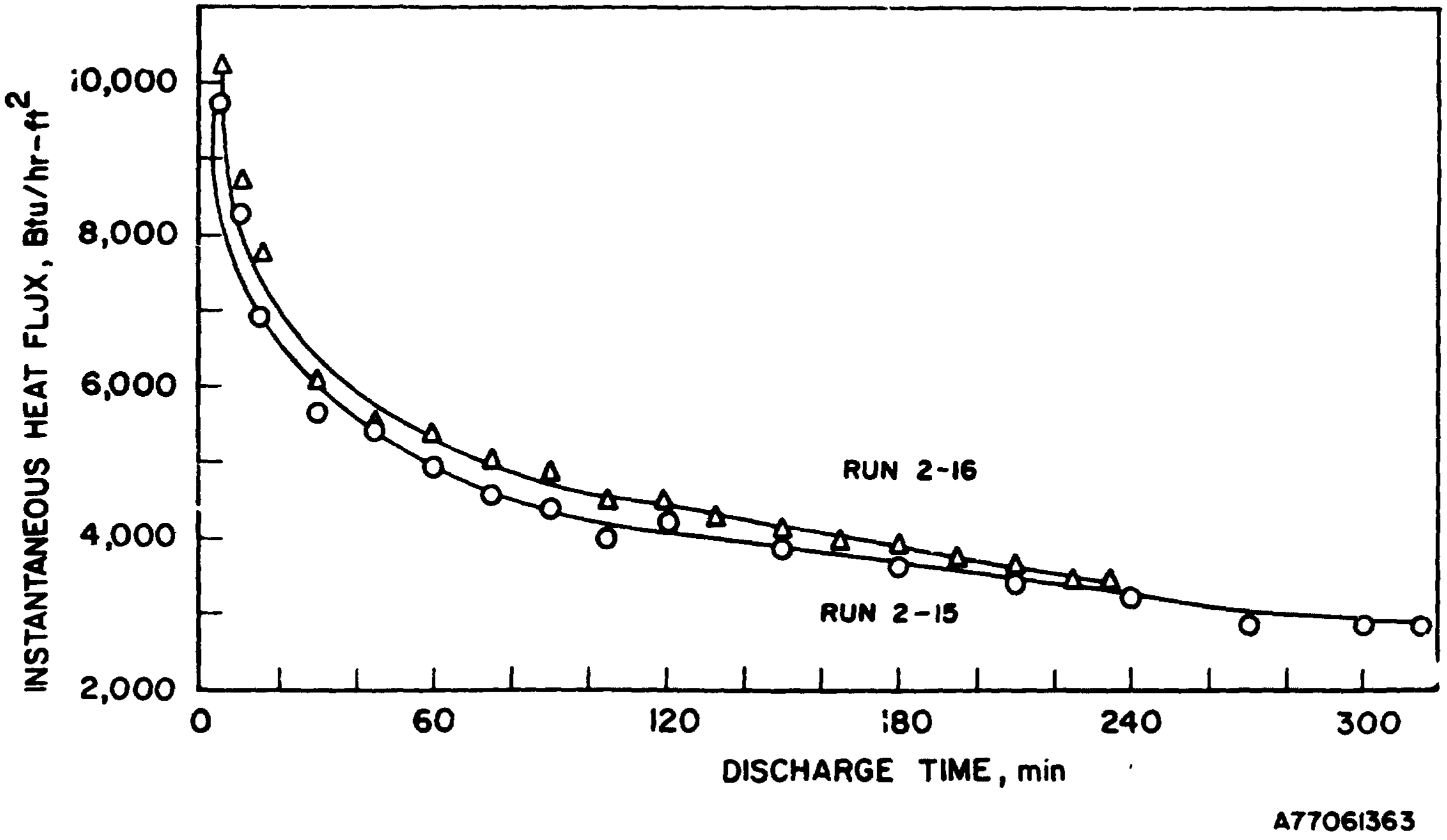

Figure 31. EFFECT OF UNDERCHARGE ON HEAT FLUX

on a run using air-temperature information collected at the heat exchanger inlet and outlet (BB'), 40% to 50% of the stored heat is shown to be not recovered by the heat-transfer fluid, and therefore lost to the ambient. Similar calculations made with air temperatures measured at the system inlet and outlet (AA') show losses to the ambient to be half as large. These values correspond more closely to the heat losses predicted by input power drawn during holding periods. Although only 50% to 60% of the energy is recovered in the heat exchanger, it must be noted that about 70% of the stored energy not recovered in the heat exchanger is composed of heat transferred to the coolant outside of the heat exchanger, as evidenced in the first unit and shown in Run 2-20. Since no approximation can be made as to where this heat would have gone if the system were designed differently, it will not be considered in evaluating efficiency. As a result, the efficiencies will appear low, but should be used for comparative purposes only.

An energy balance cannot be made on Run 2-16 because the exact charged capacity cannot be determined. A capacity value can be approximated, however, by comparing the total energy input during charging for Runs 2-15 and 2-16. The energy absorbed by the system during the charging sub-cycle of Run 2-15 totaled 15.4 kWhr. This is the energy required to supply the sensible heats, heat of fusion, and heat losses to the ambient during the charging period. The energy absorbed in Run 2-16 during the charging period totaled 13.33 kWhr, or 86.5% of the energy drawn in Run 2-15. Assuming the charged capacity of Unit 2 in Run 2-16 to be 86.5% of that in Run 2-15, the following analysis can be made:

	Run 2-16
Heat Available for Extraction [(0.865)(28,033)], Btu	24,248
Heat Extracted by the Coolant Air, Btu	13,326
Heat Extraction Efficiency (Heat Exchanger Only), %	55

Graphical integration of the performance curve for Run 2-16 shown in Figure 31 yields an overall average heat flux of 4732 Btu/hr-ft^2. A similar measurement made for Run 2-15 over the same discharge period as for Run 2-16 (0-235 minutes) yields an average heat flux of 4382 Btu/hr-ft^2. We concluded from the close agreement in average heat fluxes and heat extraction efficiencies found between Runs 2-15 (fully charged) and 2-16 (partially charged) that operation of the system below rated capacity does not alter the system heat fluxes.

This is an important observation when the periodic nature of TES system operation is considered. Radial temperature profiles through the salt obtained during a 14-hour charging period are shown in Figure 32. The salt closest to the heat exchanger begins to thermally respond to charging within a half hour after the charging is initiated. However, the bulk of the salt continues to cool throughout the first 3 hours of charging. If in this case only 11 of the required 14 hours was available for charging, the system would only be charged to about 60% capacity. Although the discharging time would be decreased, stable performance would still be obtained. This factor would become even more important if demand dictated increased utilization of the sensible heat stored in the solidified salt because of the lowered salt temperature at the completion of the discharge. The subsequent charging time would, therefore, be increased.

One of the considerations made in selecting $LiKCO_3$ as an experimental PCM was the low liquid-phase viscosity at and above the melting point. This low viscosity enhances convective mixing in the molten salt, which improves the overall heat-transfer characteristics of the system. A strong mixing effect was indicated by the inability of a thermal gradient to be sustained through the molten salt as evidenced by the flat radial temperature profiles observed during discharge. The convective effects were also indicated from axial temperature profiles obtained during discharging, shown in Figure 33. During the first half hour of discharging, the mean temperature in the upper two-thirds of the molten salt has decreased while the lower third has increased, after which a steadily decreasing flat profile is maintained to the melting point. The shape of the axial profiles also verifies the formation of a solid skin on the upper salt surface (discussed under "Unit 1 Performance — Heat Flux and Efficiency") and indicates simultaneous solidification from the bottom and top. We anticipated the solid phase to form around the heat exchanger in a conical geometry based at the container bottom. However, the combined radial and axial profiles indicate an "hour glass" geometry that results from heat loss through the top of the unit.

Unit 2 Stability and Cyclability

Stable performance was observed in Unit 2 throughout the 1400 hours of operating time. The average heat fluxes observed during discharging as determined by air-temperature information collected from around the heat

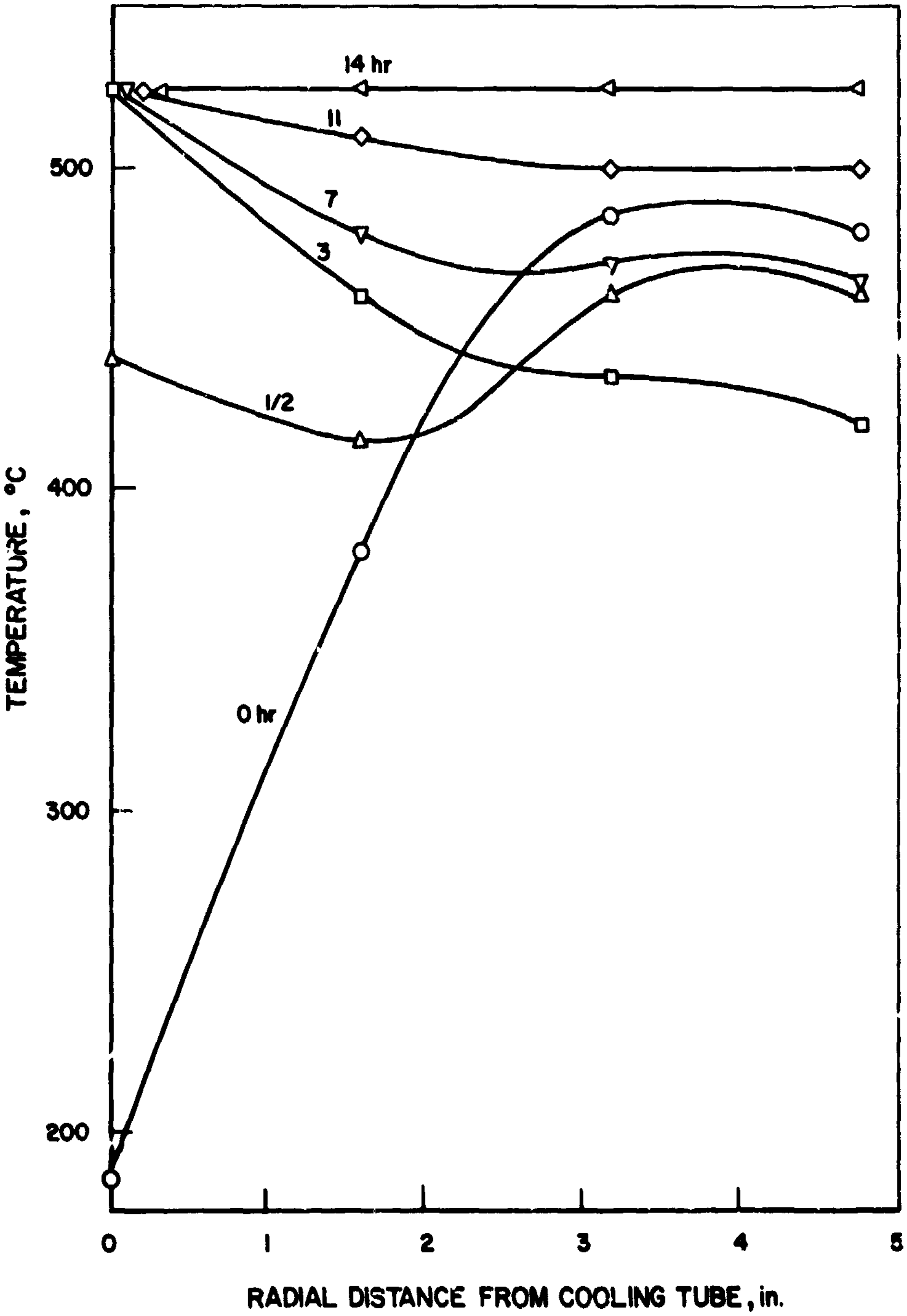

Figure 32. SALT RESPONSE DURING CHARGING

ORIGINAL PAGE IS
OF POOR QUALITY

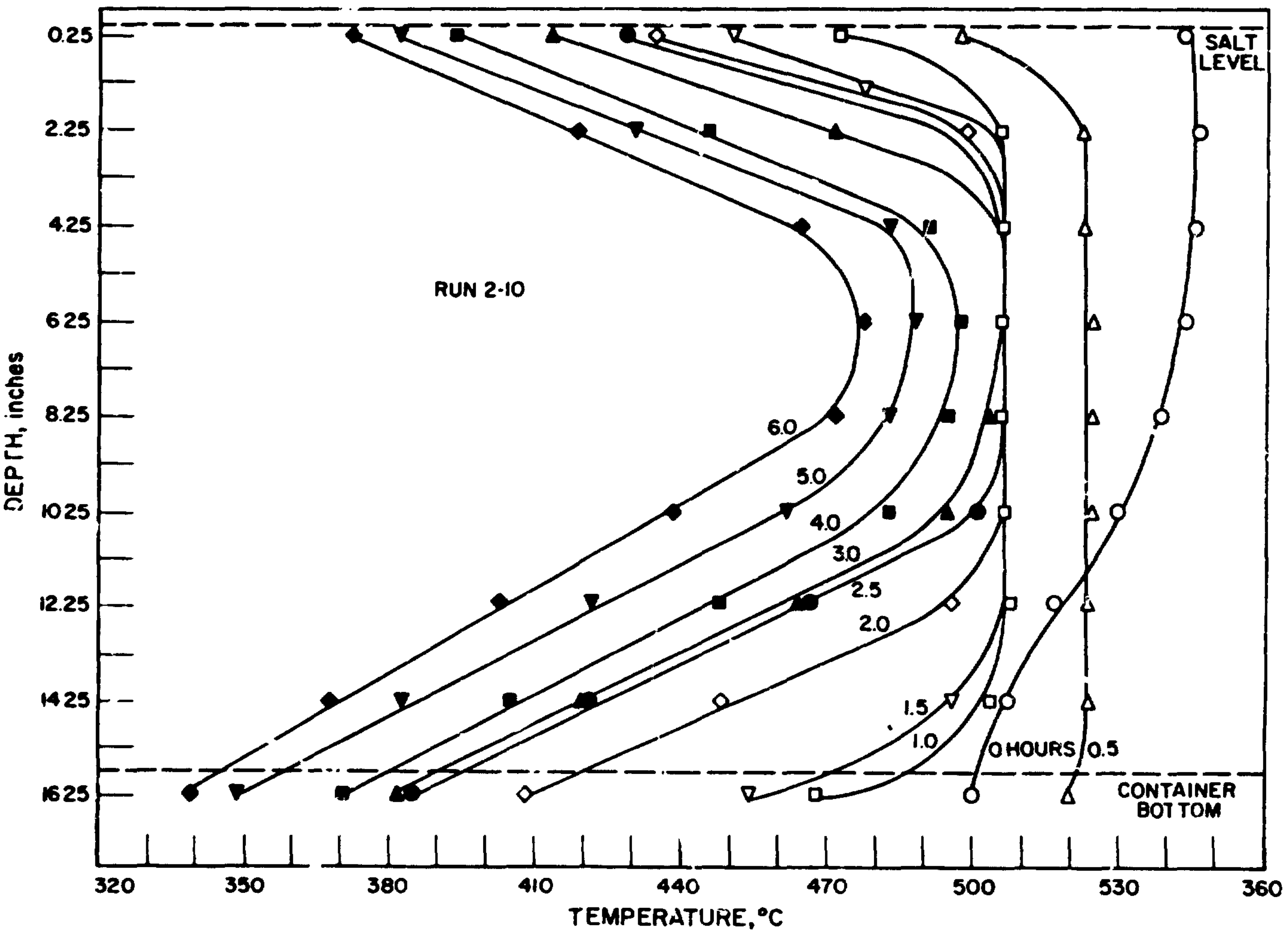

Figure 33. VERTICAL TEMPERATURE PROFILE AS A FUNCTION OF TIME AT A MIDRADIAL PLANE

exchanger varied over a narrow range between 3900 and 4100 Btu/hr-ft^2 when discharging was accomplished from and to design conditions. The discharge time required for each run is shown in Figure 34. The time required for discharge of the 15 runs, which started from design conditions, remained relatively constant, averaging 5 hours and 15 minutes, about 25 minutes faster than for the first unit, due to the higher flow rates. The charging performance was similar to that observed in the first unit; however, charging and holding times were varied over a wider range. No difficulties in completing a cycle were found if a minimum of 8 hours was allowed for charging. Charging in less than 8 hours required salt temperatures in excess of 593°C in some locations during the charging period, thereby increasing the possible corrosive reactions and vapor loss due to local overheating.

All materials in the system also performed well throughout the operating period. Corrosion was light on the interior of the unit, and no leaks were found. Slight vapor losses were indicated at the sealing flange junctions as in Unit 1, but no weight loss could be detected. The salt showed no signs of discoloration after 30 cycles, and chemical analysis showed no change in the salt composition within limits of detection (±0.5%). DTA and DSC testing of salt samples taken from six different locations in the unit indicated well-defined fusion characteristics with melting points of 505° to 506°C and heats of fusion between 152 and 155 Btu/lb. No secondary compounds could be detected from thermal effects.

Evaluation of $LiKCO_3$ With a Finned Tube

Unit 3 Operation — Finned-Tube Heat Exchanger Design

A third engineering-scale unit was constructed and operated as were the first two units, but it contained a finned-tube heat exchanger to evaluate the effects of heat-transfer enhancement. The fins were constructed of 304 stainless steel flat stock, 15 inches long, 3 inches wide, and 1/8 inch thick. Eight grooves spaced every 45° were milled into the cooling tube. The fins were placed in the grooves, and each was heli-arc welded around its entire base to ensure good heat transfer. They were spaced 3/4 inch from the bottom of the unit and 2 inches from the top to avoid increased losses to the ambient. The relative radial spacing of the fins can be seen in Figure 35. They increase the salt-side surface area of the cooling tube from about 100 to 705 square inches.

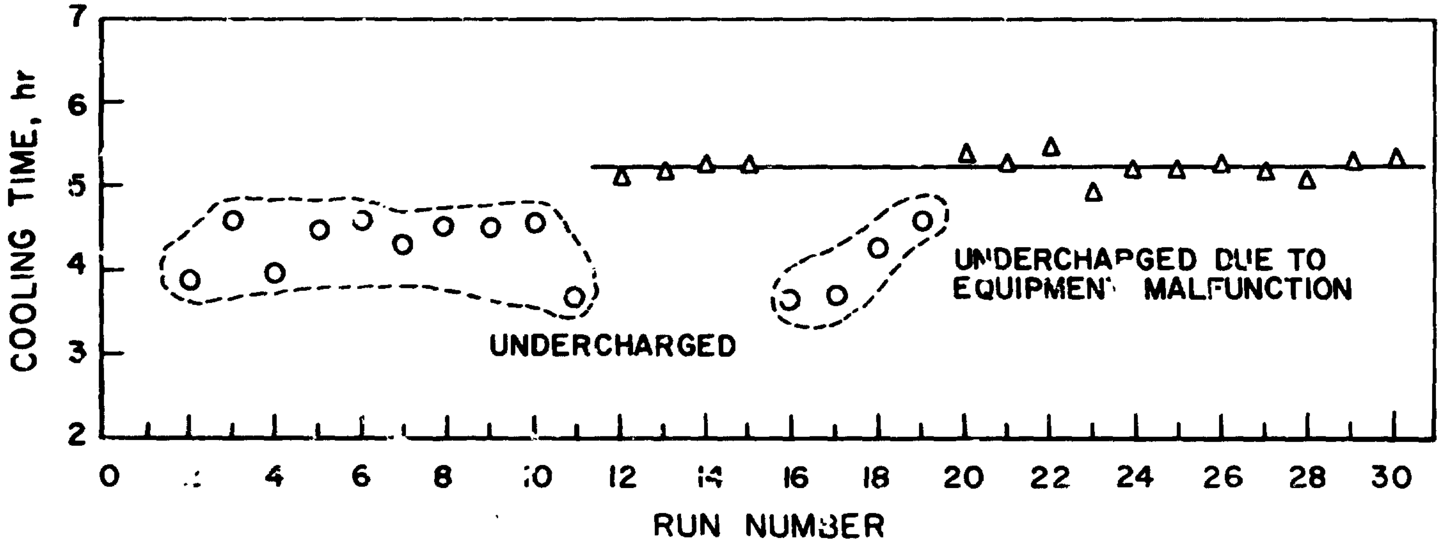

A78030719

Figure 34. UNIT 2 STABILITY WITH CYCLING

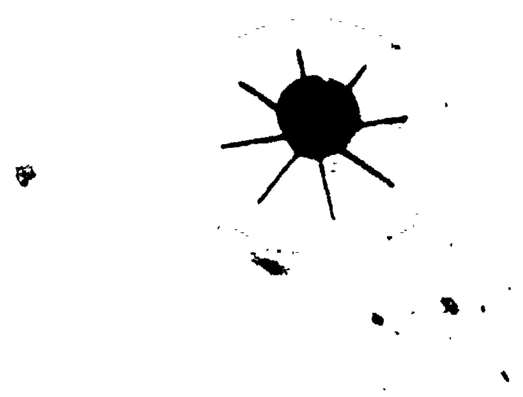

Figure 35. FINNED-TUBE HEAT EXCHANGER LOCATED IN THE ENGINEERING-SCALE TES UNIT

Unit 3 Performance — Heat Flux and Efficiency

The third TES unit was cycled 11 times, representing 650 hours of operation. Performance evaluation made on this unit was based on air-temperature information collected at the heat exchanger inlet and outlet only (B-B' in Figure 18). The performance observed in Run 3-10 is summarized in Table 10.

The overall average heat flux for this run was determined by graphical integration to be 5250 Btu/hr-ft^2 during discharging.

The influence on performance of the finned heat exchanger is summarized in Table 11, where average performance statistics for Units 2 and 3 are compared. The resulting performance improvements are best explained by differences in the heat exchanger thermal state induced by the addition of fins. The average salt-side heat exchanger surface temperature and surface temperature differential from top to bottom for Units 2 and 3 are shown as a function of discharge time in Figure 36. The use of fins (Unit 3) results in improved conduction through the solid salt and produces a higher average surface temperature distributed more evenly along the entire length at the

C-8

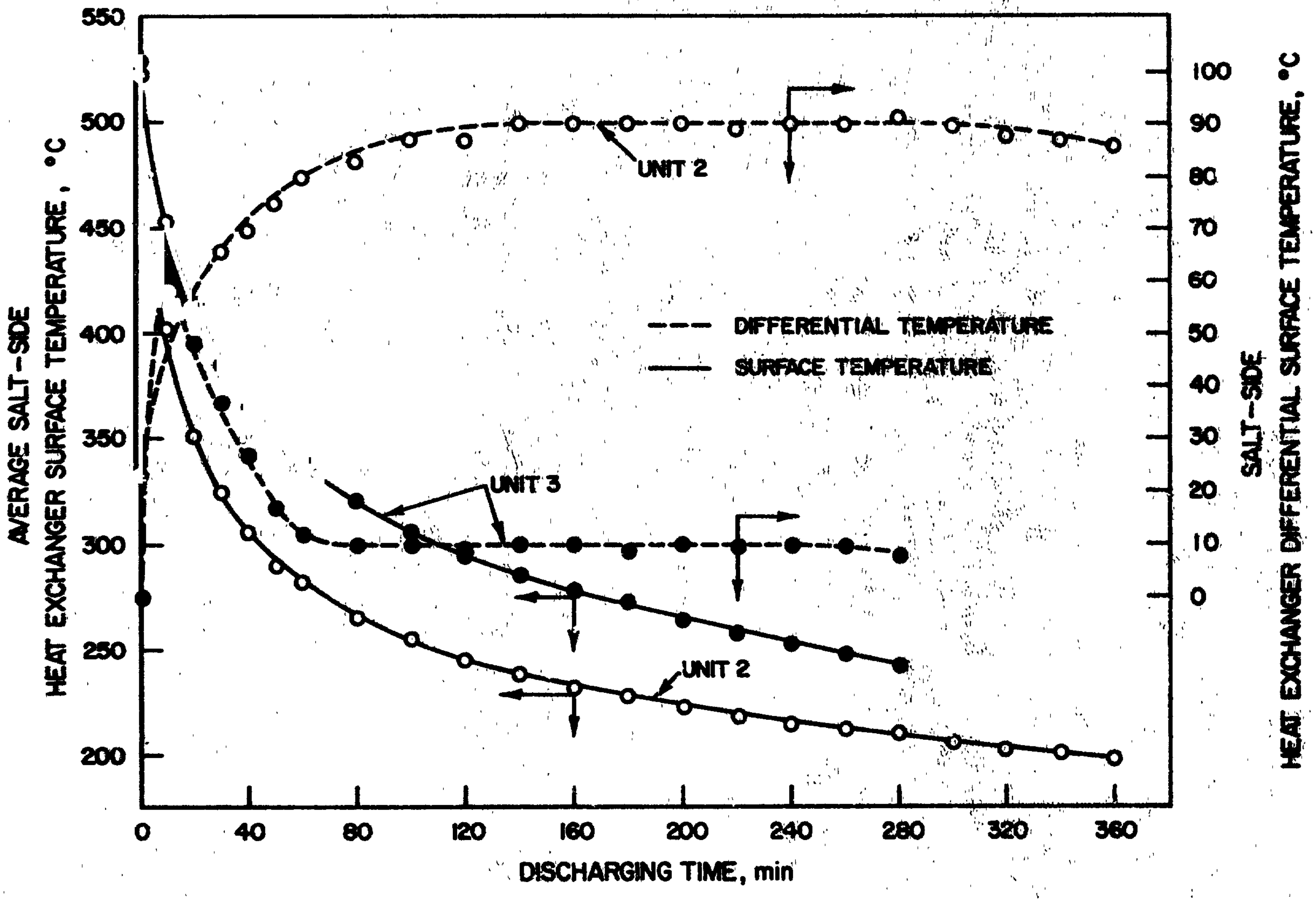

A78030711

Figure 36. EFFECT OF FINS ON TEMPERATURE AT THE SALT-SIDE HEAT-TRANSFER SURFACE

Table 10. REPRESENTATIVE THERMAL PERFORMANCE OF TES UNIT 3

	Run 3-10
Heat Flow, Btu	
Sensible Heat Removed From the Liquid	2,204
Heat of Fusion Removed	18,944
Sensible Heat Removed From the Solid	4,326
Total Heat Extracted From the Salt	25,474
Sensible Heat Removed From the Container	2,000
Sensible Heat Removed From the Insulation	1,050
Total Heat Lost by the System	28,524
Heat Extracted by the Coolant Air	17,170
Charging Energy, Btu	28,938
kWhr$_e$	8.47
Heat Extraction Efficiency (Heat Exchanger Only), %	60
Storage Efficiency (Heat Exchanger Only), %	59

Table 11. PERFORMANCE CHANGES RESULTING FROM ENGINEERING-SCALE OPERATION WITH HEAT-TRANSFER ENHANCEMENT

	Unit 2	Unit 3	Change With Fins
Discharge Heat Flux	4000 Btu/hr-ft^2	5300 Btu/hr-ft^2	+32%
Heat Extraction Efficiency	56%	61%	+9%
Storage Efficiency	53%	60%	+13%
Discharge Time	315 min	230 min	−27%

heat exchanger. Because the heat-transfer rate is directly dependent on the temperature difference between the heat-transfer surface and the coolant, a more efficient utilization of the heat-transfer area results; and subsequently a higher heat flux is attained. The improved thermal conduction resulting from the addition of the fins is also evidenced by a flattening of the radial temperature distribution (Figure 37) when compared to units without fins (Figure 38). The resulting increase in the rate at which the solid-salt layer increases in thickness is shown in Figure 39. The increased storage efficiency is primarily a result of the shorter discharge time, decreasing heat losses.

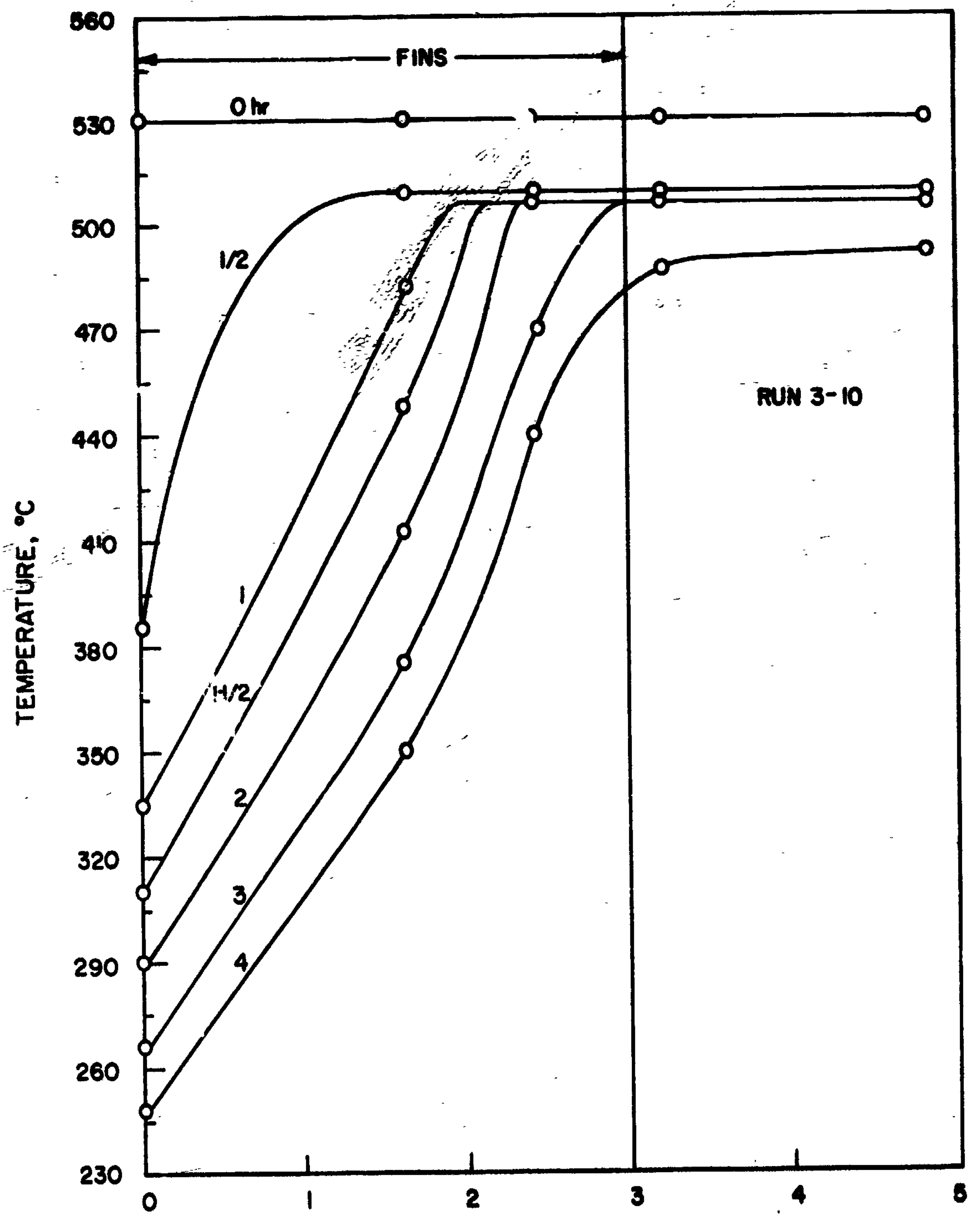

A78030797

Figure 37. SALT TEMPERATURE PROFILE AT HALF DEPTH DURING DISCHARGING WITH A FINNED-TUBE HEAT EXCHANGER

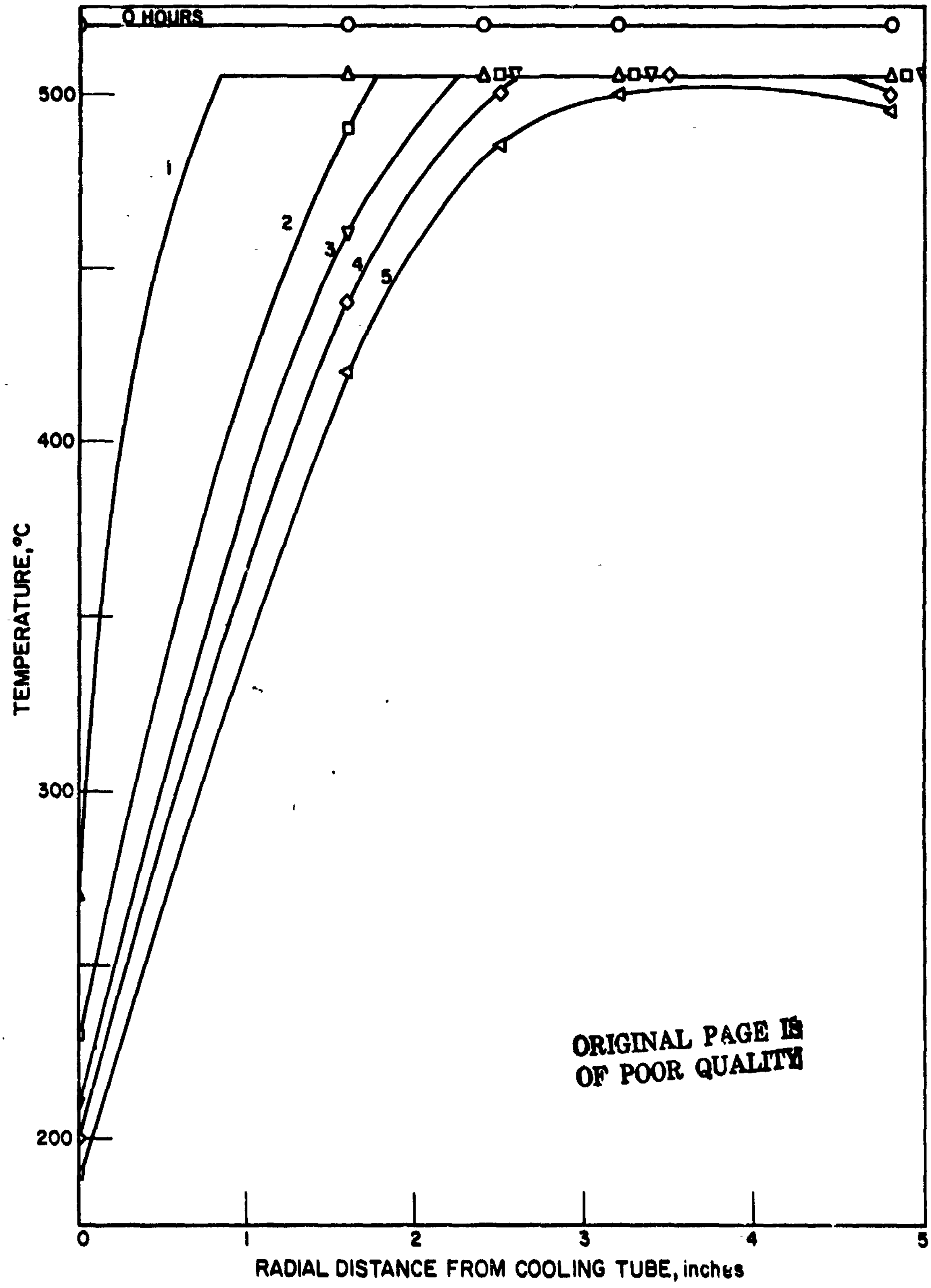

ORIGINAL PAGE IS
OF POOR QUALITY

Figure 38. SALT TEMPERATURE PROFILE AT HALF DEPTH DURING DISCHARGING; $LiKCO_3$ ALONE

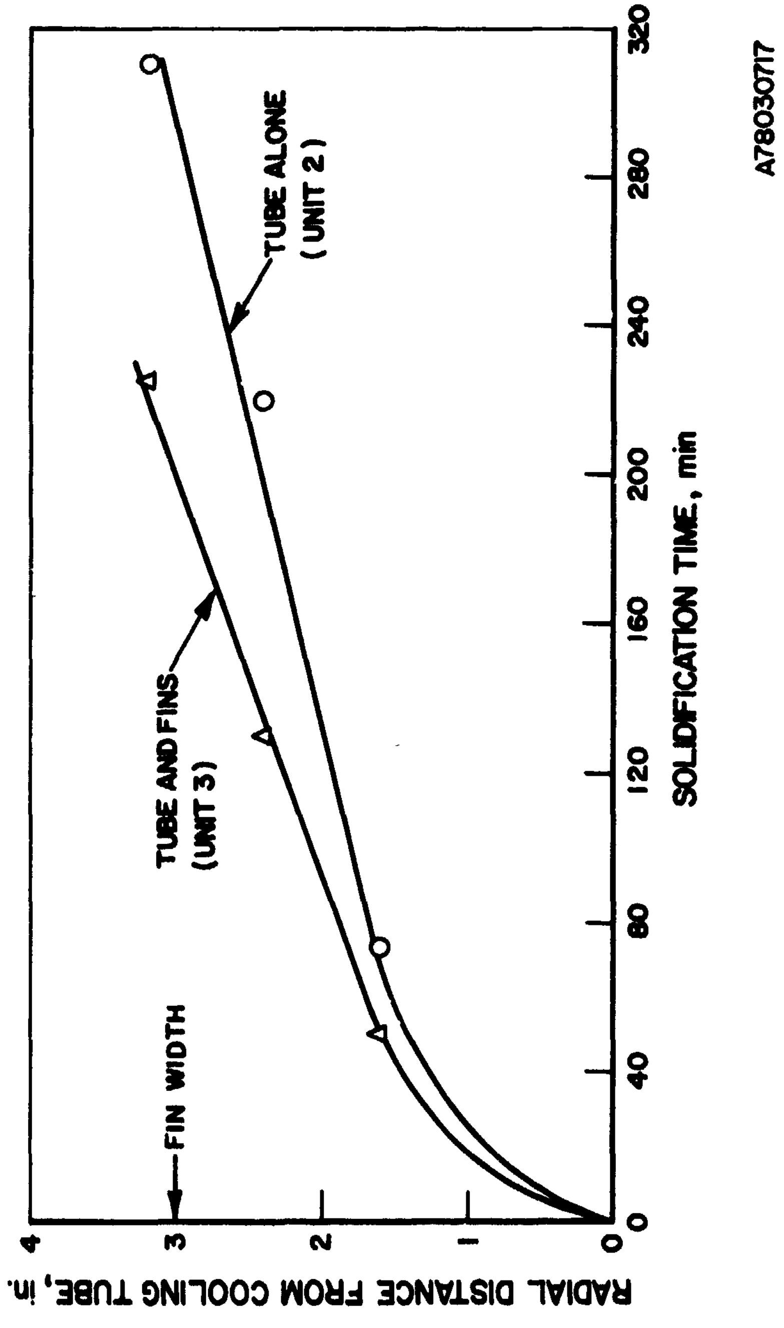

Figure 39. EFFECT OF FINS ON SOLIDIFICATION RATE

The 32% improvement in the heat flux corresponds closely to the 25% improvement observed in the laboratory TES system (Figure 13 and discussion) when a finned-tube heat exchanger was used. As a comparison of the performance curves for Units 2 and 3, the averages of the last two runs made on each unit are presented in Figure 40. The goal of conduction enhancement is to both increase and stabilize the heat flux during discharging. The performance in Unit 3 indicates the heat flux improvement, but shows a more rapid change in the flux with time after the bulk of the molten salt has been cooled to the melting point. This effect results from the diminishing influence of the dimensions and spacing of the fins as the solid salt increases in thickness, and is intensified by the shorter discharge time.

The influence of the fins is much less pronounced during charging. The radial temperature distribution during charging is shown for Unit 3 in Figure 41. Comparison with temperature profiles observed without any conduction enhancement (Figure 32) makes it evident that the fins improve the charging characteristics only during the first 2 to 3 hours, or until enough molten salt has been formed to provide its own conduction enhancement. The net result is a 7% decrease in the time required for charging.

Unit 3 Stability and Cyclability

Because of the short operating time, a quantitative assessment of the unit stability was not practical. However, a qualitative indication of the system stability was found by the uniform discharge time per cycle shown in Figure 42. As previously discussed, both the charging and discharging times were reduced by the use of the finned-tube heat exchanger; and cycling in 24 or 48-hour periods was achieved, although it required longer holding periods. This unit was not disassembled after completing operation; therefore materials performance was not established.

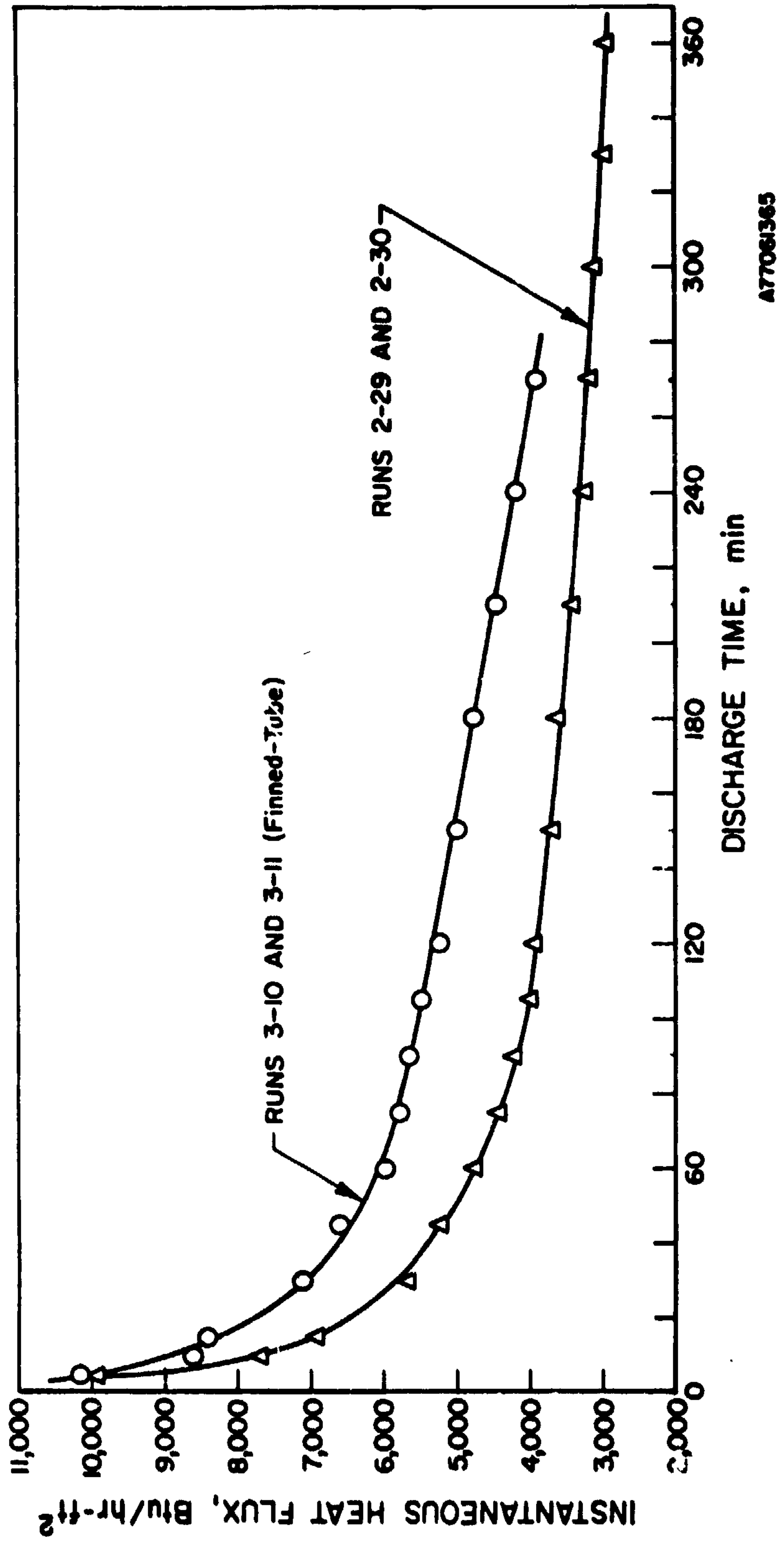

Figure 40. EFFECT OF FINS ON HEAT FLUX

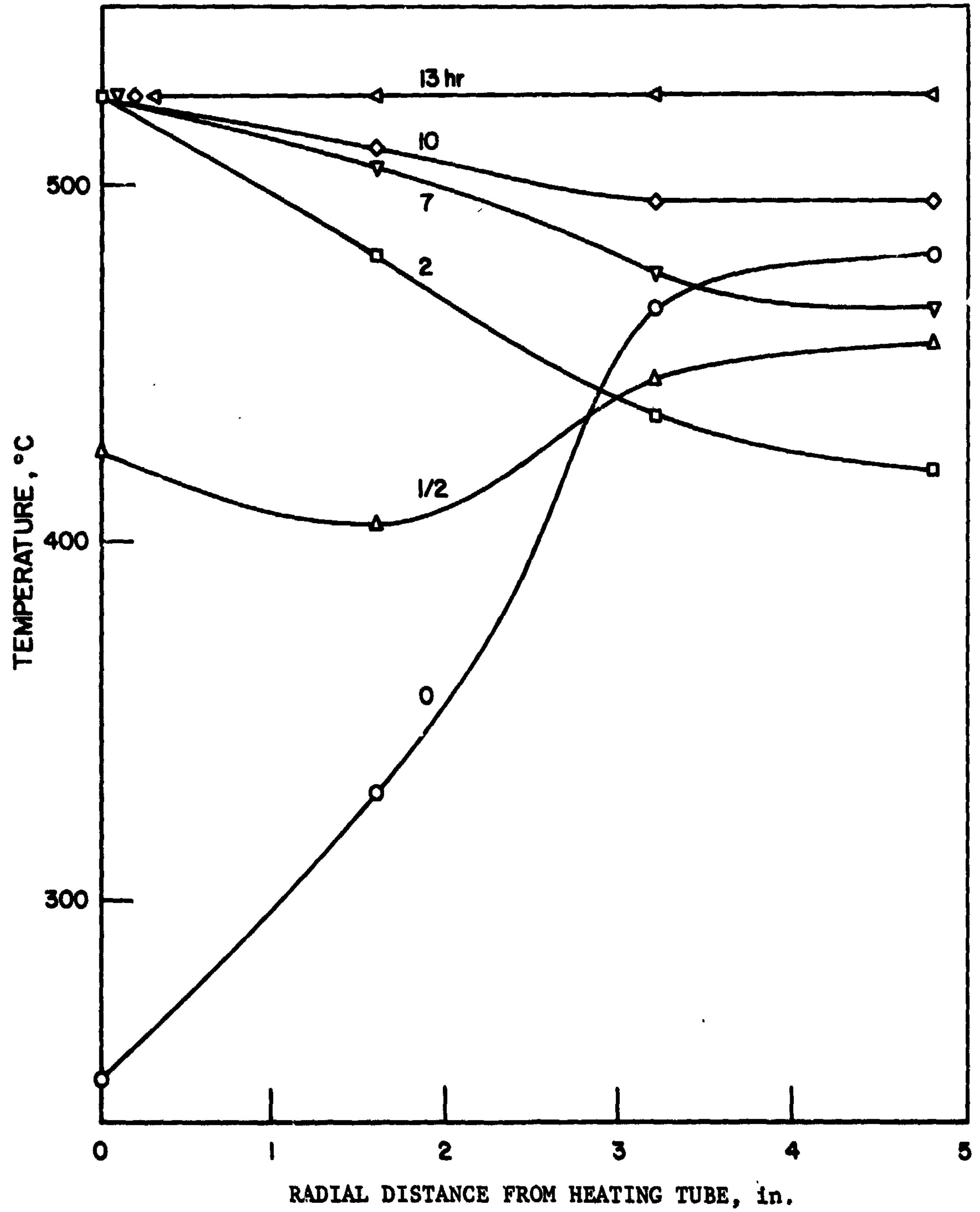

Figure 41. SALT RESPONSE DURING CHARGING WITH FINNED-TUBE HEAT EXCHANGER

ORIGINAL PAGE IS OF POOR QUALITY

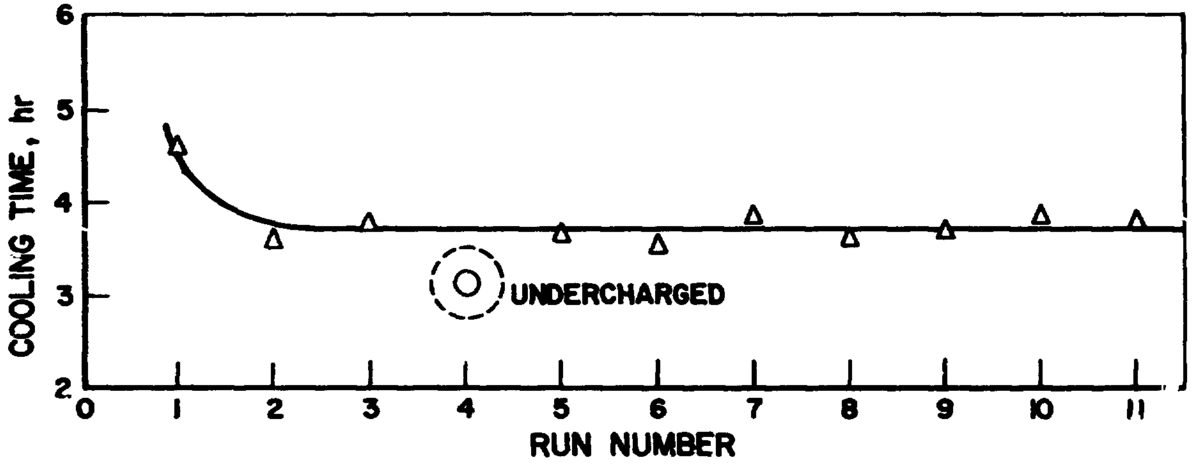

A78030715

Figure 42. CYCLE STABILITY OF UNIT 3

Task 4. Compare Experimental Performance of Engineering-Scale System With Its Predicted Performance

Introduction

One of the primary goals of this program was to develop a heat-transfer model capable of predicting the thermal behavior of a TES system in terms of its method of operation and the properties of the storage material. Because phase change is employed as the storage mechanism, a moving-boundary solution governed by heat-transfer characteristics was needed. Solutions of this type derived by various investigators were examined for their thoroughness and applicability to the problem at hand as determined by the system under investigation here. (See section covering Task 2.) One such solution of phase-change heat flow proposed by Megerlin[22] was found to meet the criteria. In his solution, Megerlin derived an equation giving the dimensionless velocity of a solid-liquid interface with respect to a heat-transfer surface in terms of the system design with suitable constraints. We converted this solution to a more usable form to give the dimensionless time (N_{FC}) needed to solidify a molten material to a dimensionless thickness ($R-1$), and then evaluated it numerically for the conditions under which the experimental TES system was to be operated. The experimental system was designed to generate the information required to verify Megerlin's solution in our form. The results of this effort are discussed here.

Solidification of $LiKCO_3$ Alone; Movement of the Solid-Liquid Interface During System Discharge

An annular arrangement was selected for the unit design for ease of comparison with the theoretical model. Thermocouples were located at half depth in the salt at various radial locations (0.25, 1.6, 2.4, 3.2, and 4.8 inches from the heat exchanger), and their response with time was recorded during discharging. A typical discharge trace is shown with the unit design in Figure 43. The time required for the freezing front to reach the location of a thermocouple was determined from the traces as the point where that thermocouple began to indicate a temperature below the melting point and subsequently yielded a descending cooling curve characteristic of a solid being cooled. The times required for the solid front to reach thermocouples isolated from edge effects (such as heat loss) are summarized in Table 12 for several standard runs made on Unit 2. The averages of these times are summarized in

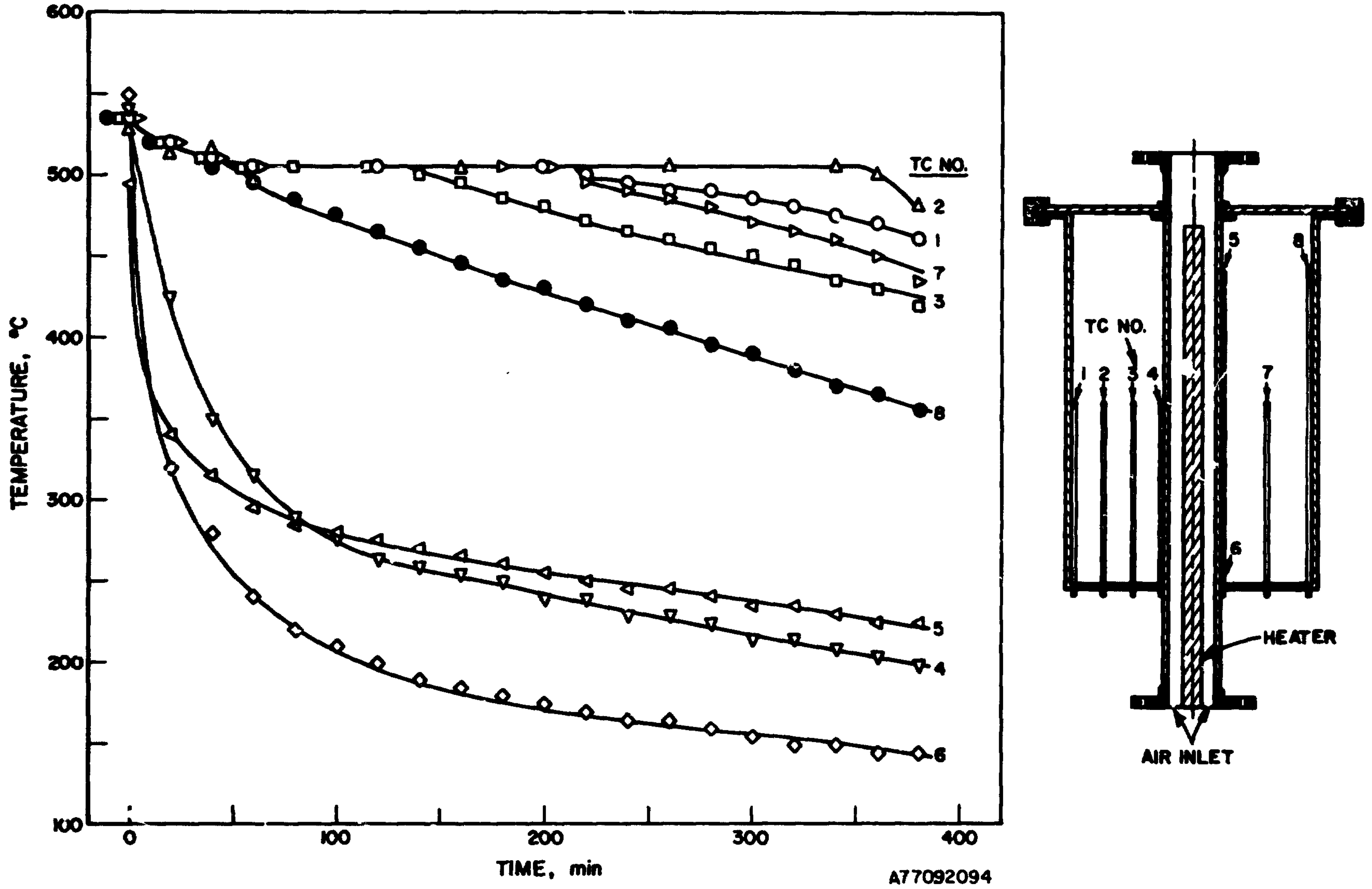

Figure 43. TYPICAL TEMPERATURE RESPONSE AT VARIOUS LOCATIONS IN THE ENGINEERING-SCALE UNITS DURING DISCHARGING

Table 12. INTERFACIAL MOVEMENT IN ENGINEERING-SCALE UNIT 2

Run No.	Starting Temperature, °C	Time to Cool Liquid, min*	Time Required for Interface to Reach Radial Locations (R–1) of 0.25	1.6	2.4	3.2
			min			
2-15	525	65	4-6	105	215	300
2-21	525	60	4-6	100	220	310
2-22	525	63	4-6	90	208	314
2-23	525	63	4-6	90	218	300
2-24	525	65	4-6	85	210	295
2-26	525	60	4-6	85	223	310
2-27	527	63	4-6	85	205	295
2-28	530	60	4-6	90	220	280
2-29	525	62	4-6	95	220	303
2-30	527	65	4-6	90	225	300

*Time required to cool the bulk of the molten salt from the starting temperature to the melting point (505°C).

Table 13 with the radial locations of the thermocouples and the calculated Fourier numbers. The theoretical solidification profile determined by numerical evaluation of the Megerlin solution for our system ($N_{ph} = 0.57$, $N_{Bi} = 0.75$) is shown in Figure 44 with the experimental profile. The observed behavior is in good agreement with the predicted behavior during the early stages of discharge ($N_{Fo} < 4$), but is only fair during the remainder of the discharge period, which shows the solidification proceeding slower than predicted.

The sources of deviation between the theoretical and experimental behaviors become apparent when the differences between the physical model and the idealized description given by the Megerlin solution are examined, as in Table 14. The primary source of error appears to be in the excess enthalpy or superheat stored as sensible heat in the molten salt and container at the operating temperature (~20°C above t_m). The superheat may be considered in the model two ways as follows.

In the first treatment, the superheat is considered to affect the system behavior as if its source were the heat of fusion of the PCM. The sensible heat contained in the salt over the 20°C superheat amounts to ~17 Btu/lb. Adding this heat to the heat of fusion of $LiKCO_3$ results in an "apparent" heat of fusion of 165 Btu/lb (148 Btu/lb + 17 Btu/lb). Recalculating the phase-change number on this basis leads to an apparent N_{ph} of 0.63, shifting the theoretical curve ($N_{ph} = 0.57$) in Figure 44 to the right and yielding closer agreement with the experimental curve. If the heat content of the container above t_m is included, the apparent $N_{ph} \cong 0.7$, which brings the theoretical and experimental curves even closer together.

In the second treatment, the concept of sensible heat displacing the heat of fusion is considered, as discussed under "Unit 1 Performance — Heat Flux and Efficiency." It has been calculated, from the knowledge of the average heat fluxes and the heat contents of the steel can and the insulation, that the loss of the specific superheat plus the loss of the can-and-insulation heat content in time, decoupled from the solidification process, amounts to about 34 minutes, or 0.56 hour. If it is assumed that little or no solidification occurs until the superheat is removed, the solidification time scale is shifted by 0.56 hour, representing a correction on N_{Fo} of 2.31 ($N_{Fo}' = N_{Fo} - 2.31$). Applying this correction to the calculated Fourier numbers shown in Table 13 (where applicable) almost brings the experimental and predicted curves in

Table 13. COMPARISON OF THEORETICAL AND OBSERVED SOLIDIFICATION BEHAVIOR

Radial Location (R-1)	Average Time, min	N_{Fo} Observed	N_{Fo} Theoretical
0.25	5	0.4	0.35
1.6	91.5	6.3	4.0
2.4	216.4	14.9	9.0
3.2	300.7	20.7	15.5

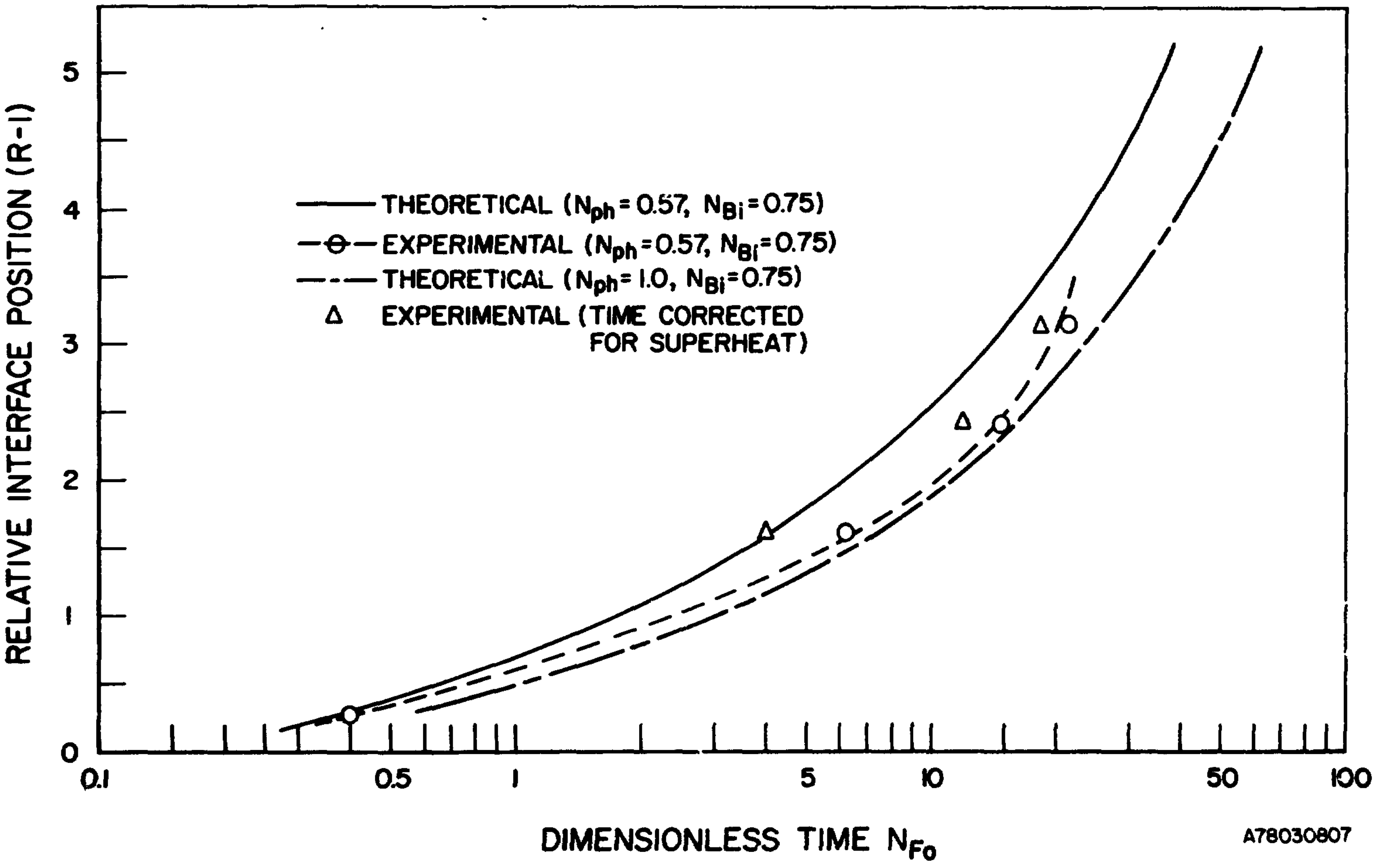

Figure 44. COMPARISON OF SOLIDIFICATION PROFILES

Table 14. COMPARISON OF MEGERLIN SOLUTION AND PHYSICAL MODEL

Condition	Mathematical Description	Physical Model
The Arrangement	Cylindrical, circular, axisymmetric	Cylindrical, circular, axisymmetric
Internal Radius	r_o	r_o = 1 in.
External Radius	Infinite	Finite, r = 6 in.
Axial Dimension	Infinite	Finite, L = 18 in.
Initial Temperature	At melting point t_m	Above melting pt
Excess Enthalpy Above t_m	0	(0.42)(40) ≅ 17 Btu/lb
Misc Losses	0	Via insul, supports, etc.
Heat Content of Containers and Insul	0	12 Btu/°F for the can 22 Btu/°F insulation

Figure 44 together. Other variations, which, if corrected for, would tend to bring the curves even closer together are —

a. The finite axial dimension of the physical model as opposed to the infinitely long analytical solution suggests that, at the radius nearest to the entry of the coolant, the freezing front would form faster. (The coolant enters at 49°C, is about 62°C in the middle at the thermocouple level, and leaves, on the average, at 77°C.)

b. The convective currents in the liquid phase (left out of account completely in the analytical model) would tend to slow down the solidification process.

With these considerations in mind, the agreement between the observed and predicted behavior appears good throughout the entire solidification period.

Use of the Heat-Transfer Model in Large-Scale System Design

Introduction

The phase-change heat flow model developed by Megerlin[22] and evaluated at IGT during the course of this project can be used in large-scale system design. In the IGT form, Megerlin's solution determines the extent of thickness around a cylindrical internal well (tube) carrying a cooling fluid to which a PCM will solidify as a function of the time it has been cooled from its melting point, measured in terms of the radius of the internal well. The model accounts for the flow and thermal properties of the working fluid and the thermophysical properties of the PCM (heat of fusion, heat capacity, melting point, thermal conductivity, and density). It yields the amount of a PCM that is solidified with respect to the system design and mode of operation and, therefore, indirectly gives a measure of the energy transferred from the storage material to the working fluid under the same constraints.

If the conceptual system is a large molten salt bath with a number of pipes running parallel to each other in a well-formed matrix carrying the working fluid through the salt bath, the model will determine the pipe spacing, the number of pipes required, and their length (given the pipe radius) for a particular storage requirement. Consequently, the model relates the energy discharged from a system to the physical design of the system, allowing a balance to be made between the energy required as determined by the working fluid conditions and the energy discharged that results from the system design.

TES System for Steam Upgrading

To show how the heat-transfer model may be used in system design, we will apply it to a storage system in which high-temperature, high-pressure steam is the working fluid. In this system, $LiKCO_3$ will be used as the PCM for the purpose of superheating the steam at 1000 psi from 550°F (288°C) to 900°F (482°C) over a 6-hour period during which the steam flow will be 5.0×10^5 lbm/hr. The enthalpy change in the steam is 249.2 Btu/lbm (from the Steam Tables), so the total system capacity must be —

$$(249.2 \text{ Btu/lbm})(5 \times 10^5 \text{lbm/hr})(6 \text{ hr}) = 7.48 \times 10^8 \text{ Btu} \qquad (44)$$

which represents —

$$(7.48 \times 10^8 \text{ Btu})/(148 \text{ Btu/lb}) = 5.05 \times 10^6 \text{ lb} \qquad (45)$$

of salt (heat of fusion only). The volume of salt that must be solidified (using the room-temperature density for a first approximation) is —

$$(5.05 \times 10^6 \text{ lb})/(141 \text{ lb/ft}^3) = 3.58 \times 10^4 \text{ ft}^3 \qquad (46)$$

This sets the "fixed volume" requirement that the heat-transfer model will be applied to solving. The phase-change number determined for a mean steam temperature of 725°F (385°C) is —

$$N_{ph} = \frac{\Delta H_f}{c_p(t_m - t)} = \frac{(148 \text{ Btu/lb})}{(0.32 \text{ Btu/lb-°F})\ (941\text{°F}-725\text{°F})} = 2 \qquad (47)$$

The Megerlin plots for $N_{ph} = 2$ and a range of Biot numbers are shown in Figure 45.

In this example, we have chosen to use pipes with a 2.5-in. diameter, and need to determine the number of pipes required, their spacing, and their length. The Fourier number corresponding to a 1.25-in. (0.104-ft) radius and a 6-hr discharge time is —

$$N_{Fo} = \frac{\alpha\ \tau}{r_o^2} = \frac{(0.0287 \text{ ft}^2\text{/hr})(6 \text{ hr})}{(0.104 \text{ ft})^2} = 15.9 \qquad (48)$$

Given the pipe diameter, $2\,r_o$, the Biot number N_{Bi} need only be specified now to use the Megerlin plots in Figure 45 to determine r_1, which will yield the thickness of the solidified salt $(r_1 - r_o)$ and the pipe spacing $(2\,r_1)$. The pipe length is determined from the fixed volume requirement:

$$L_1 = (3.58 \times 10^4 \text{ ft}^3)/(r_1^2 - r_o^2)\, n\pi \qquad (49)$$

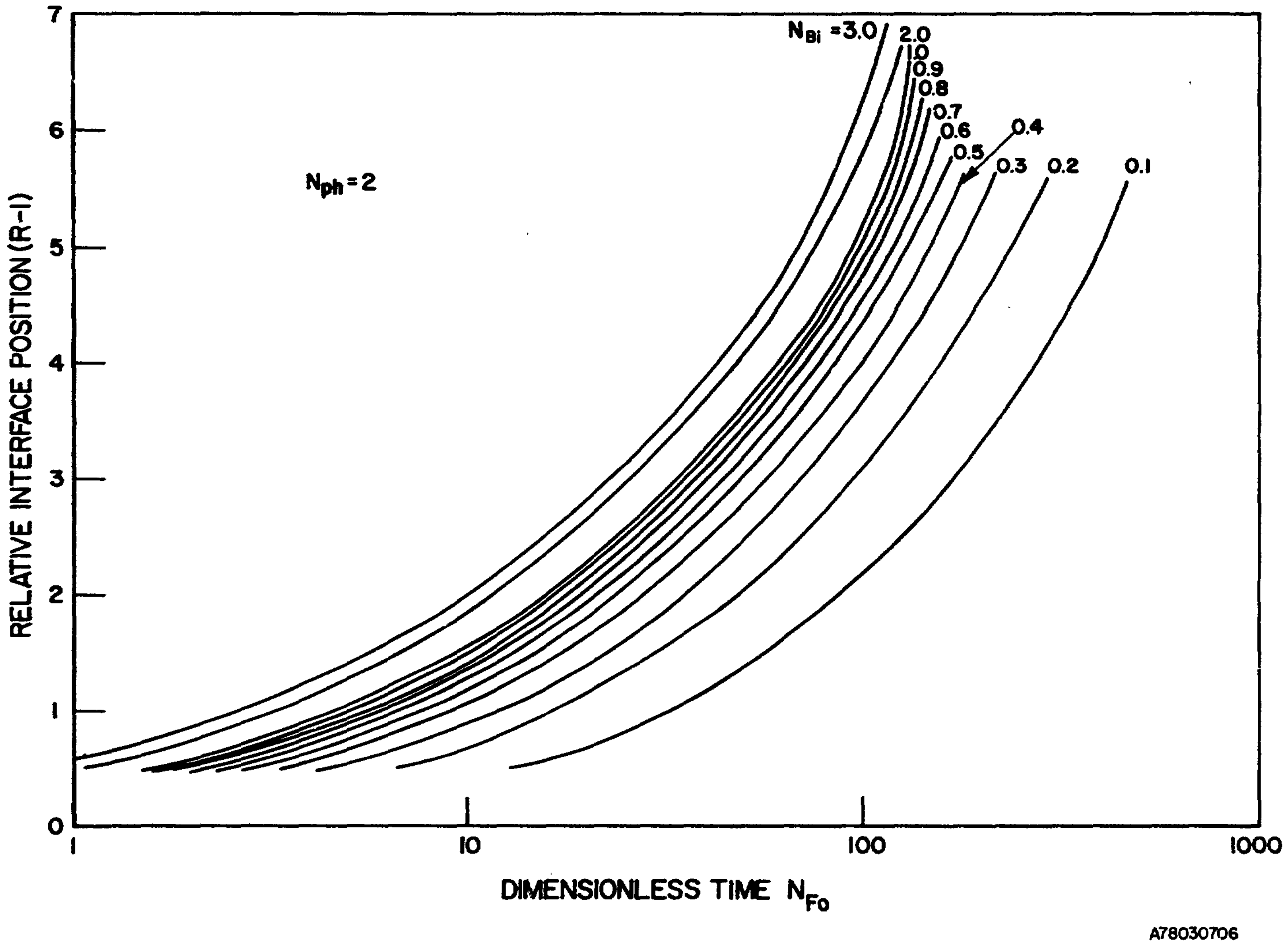

Figure 45. MEGERLIN PLOTS TO DETERMINE SOLIDIFIED FCM THICKNESS

The Biot number is given by —

$$N_{Bi} = hr_o/k_s \tag{50}$$

so that an expression for the steam-side heat-transfer coefficient, h, must be derived. In this example, we will first assume fully turbulent flow in the steam pipes that allows the use of the Nusselt equation —

$$N_{Nu} = 0.023\ N_{Re}{}^{0.8}\ N_{Pr}{}^{0.2} = \frac{hd}{k} \tag{51}$$

to derive the expression for h. Solving Equation 51 for h yields —

$$h = 0.02\ N_{Pr}{}^{0.2}\ k\ \left(\frac{\dot{m}}{\pi\mu}\right)^{0.8} n^{-0.8}\ r_o{}^{-1.8} \tag{52}$$

where n = number of pipes with radius r_o. Substituting in Equation 52 the appropriate properties for steam at 725°F (385°C) and 1000 psi, and setting $r_o = 1.25$ in. and $\dot{m} = 5 \times 10^5$ lbm/hr yields —

$$h = 5968/n^{0.8}\ \text{Btu/hr-ft}^2\text{-°F} \tag{53}$$

It can be seen from Equation 53 that L_1 and r_1 are both dependent on the number of steam pipes to be used ($N_{Bi} \propto n^{-0.8}$, r_o fixed). The pipe length, L_1, can be determined for any number of pipes by selecting n and calculating h from Equation 53, determining N_{Bi} and using it to find r_1 from the Megerlin plots, then substituting r_1 and n into Equation 49 and solving for L_1.

Now that we have calculated a pipe length consistent with a given number of tubes, n, that are sufficient to remove the heat from the salt volume, we must consider if sufficient heat-transfer surface is present to heat the steam to the required outlet temperature.

If it is assumed that the PCM remains at its melting point, the enthalpy change in the steam as it progresses through the pipe is described by —

$$\frac{\dot{m}\ c_p}{n\pi d}\ \frac{dt}{dL} = h\ (t_m - t) = h\ (941\text{°F} - t) \tag{54}$$

Rearranging Equation 54, integrating, and evaluating, given that at L = 0, t = 550°F (288°C) and at L = L_2, t = 900°F (482°C) leads to —

$$L_2 = \frac{(2.255)\ \dot{m}\ c_p}{n\pi hd} \tag{55}$$

The heat-transfer requirements will be satisfied when n is selected so that $L_1 = L_2$, which meets both the fixed-volume and steam-temperature requirements.

The solution will be obtained graphically here using Equations 49, 53, and 55, and the Megerlin plots in Figure 45 to derive Table 15.

Table 15. DESIGN PARAMETERS FOR STEAM UPGRADING, WITH $N_{ph} = 2$, $N_{Fo} = 15.9$, $r_o = 1.25$ in., AND $\dot{m} = 5 \times 10^5$ lb/hr, USING $LiKCO_3$ AS THE PCM

n	h, Btu/hr-ft²-°F	N_{Bi}	r_1, in.	L_1, ft	L_2, ft
3,000	9.87	0.79	3.56	49.3	38.4
5,000	6.56	0.53	3.25	36.5	34.7
7,000	5.01	0.40	3.00	31.6	32.4
10,000	3.77	0.30	2.75	27.4	30.2
15,000	2.72	0.22	2.50	23.4	27.9
20,000	2.16	0.17	2.31	21.8	26.3

The values of L_1 and L_2 are shown as a function of n in Figure 46. The intersection of the two curves, representing the design solution, occurs at n = 6000 and $L_1 = L_2 \equiv 33.5$ ft. Substituting n = 6000 into Equations 49, 53, and 55 yields h = 5.67 Btu/hr-ft²-°F, $r_1 = 3.13$ in., and $L_1 = L_2 = 33.4$ ft. The design conditions for the TES operation can be met by solidifying 5 million lb of $LiKCO_3$ cylindrically around 6000 2.5-in.-diam by 33.4-ft-long pipes (spaced 6.25 in. apart) over a 6-hr period. As a check, the total area open to steam flow is –

$$A = n\pi r^2 = (6000)\ (\pi)\ \left(\frac{1.25}{12}\right)^2 = 204.5\ \text{ft}^2 \qquad (56)$$

The linear steam velocity is –

$$v = \frac{(5 \times 10^5\ \text{lb/hr})\ (\text{hr}/3600\ \text{s})\ (0.6285\ \text{ft}^3/\text{lb})}{204.5\ \text{ft}^2} = 0.43\ \text{ft/s} \qquad (57)$$

where the specific volume of steam at 100 psi, 725°F (385°C) is 0.6285 ft³/lb. The Reynolds number is –

$$N_{Re} = \frac{dv\rho}{\mu} = \frac{(2.5\ \text{in.}/12\ \text{in./ft})(0.43\ \text{ft/s})(0.6285\ \text{ft}^3/\text{lb})^{-1}(3600\ \text{s/hr})}{0.0575\ \text{lb/hr-ft}} = 8900 \qquad (58)$$

which indicates fully turbulent flow and verifies the use of the Nusselt equation to derive the steam-side heat-transfer coefficient.

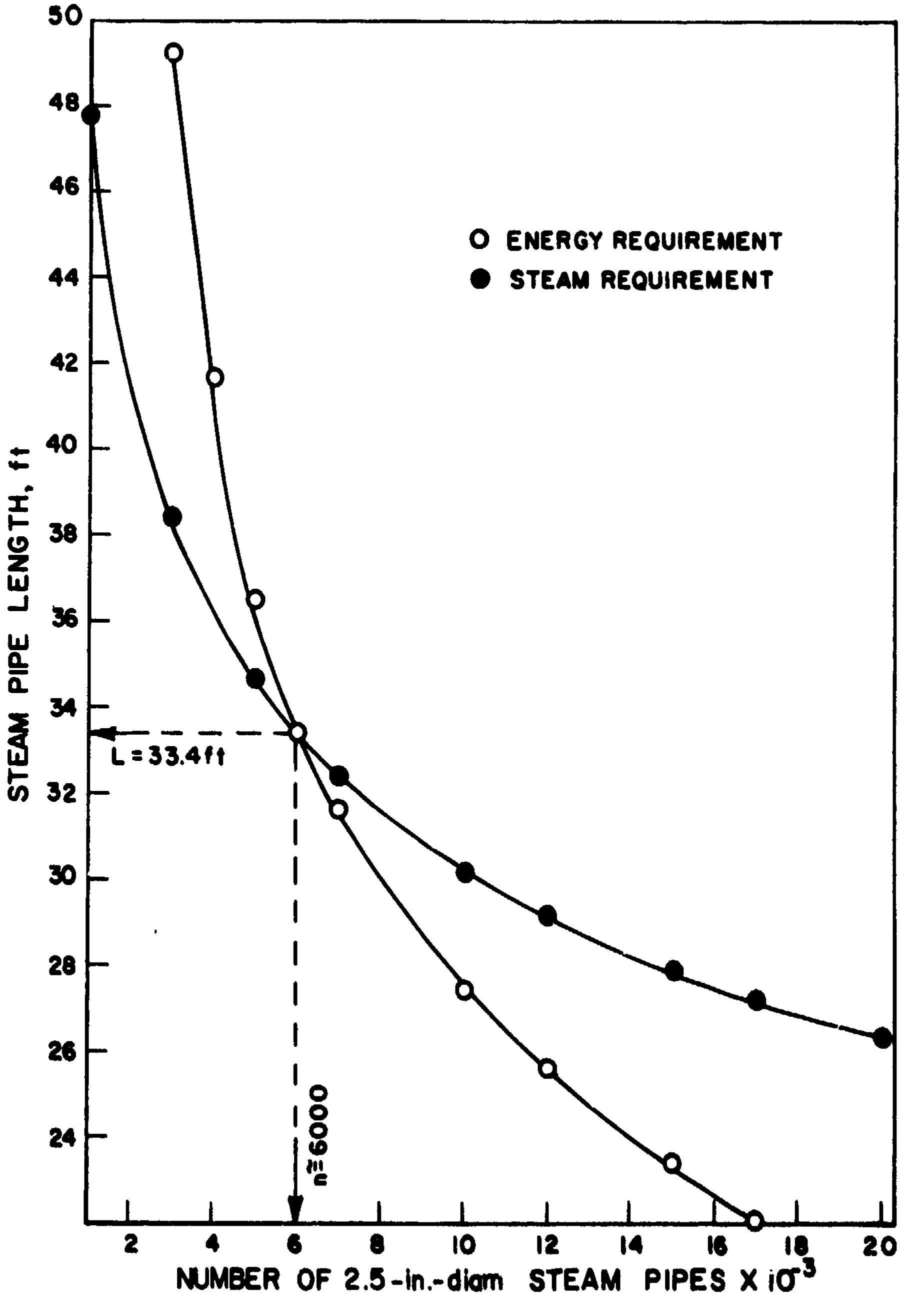

A78030700

Figure 46. GRAPHIC SOLUTION FOR NUMBER OF PIPES AND THEIR LENGTH

Although the above provides the design of a TES system capable of meeting the performance requirements, it is not necessarily the optimum system design. The use of different steam pipe sizes and the effects of conduction enhancement on the solidification process must be studied before an optimum performance design could be established. Such optimization must also include the determination of the cost-effectiveness of the possible designs, but is at present beyond the scope of this project. The example presented here does, however, show the importance of the heat-transfer model in determining key parameters for any latent-heat TES system.

Task 5. Conclusions and Recommendations

Conclusions

1. Salts

- Carbonates appear most attractive from thermal, chemical, and physical properties; $LiKCO_3$ selected as model system.

- Chlorides appear most attractive from cost considerations.

2. Heat-Transfer Modeling

- Megerlin's solution gives good agreement between predicted and observed interfacial location during heat removal phase from PCM.

- Model can be used for determining key design parameters for large-scale systems.

3. Inert Additives to Control Volume Change ($LiAlO_2$)

- Small volume change observed with model system does not require their use.

- Sedimentation does present a problem at concentrations of 20 volume percent.

- Performance is affected; heat flux lower.

- Inerts increase system cost substantially while lowering specific capacity.

4. Conduction Enhancement

- Additions of stainless steel screen, fins, and wool, and aluminum wool (3-14 volume percent) increase performance by 25%-32%.

- Wools appear most attractive of the enhancement concepts tested, particularly aluminum wool.

5. Containment

- Low corrosion of 304 and 316 SS with carbonates.

- Carbonates show no creepage, little vapor loss.

- Aluminum appears stable in the carbonate environment.

6. Engineering Performance

- Cycling easily accomplished within a 24-hour period.

- Stable performance through 1400 hours of operation.

- Cycling has no apparent influence on the salt properties.

ORIGINAL PAGE IS
OF POOR QUALITY

- Performance unaffected by degree of superheating.
- Performance was improved 30% by the addition of conductivity enhancement in the form of eight fins.
- Conduction enhancement provides more efficient utilization of heat-transfer area.
- Established baseline average discharge heat fluxes for comparative testing:

  No Enhancement: 4000 Btu/hr-ft^2

  With Enhancement by Fins: 5300 Btu/hr-ft^2
- Strong convective mixing effects identified.
- Low coefficient of expansion and related volume change on fusion of $LiKCO_3$ verified.
- Strong dependence of heat flux on solid-salt thickness.
- Heat fluxes as high as 40,000 Btu/hr-ft^2 observed, representing an upper performance limit.

7. Overall Conclusion

- Alkali carbonates are suitable for high-temperature TES applications from a performance, thermal, and chemical behavior standpoint.
- Economic feasibility can now be studied.

Recommendations for Further Research

1. Salts

- Study of lower-cost salts (commercial grade)
- Wider range of melting temperatures
- Incongruent compositions

2. Modeling Studies

- More detailed study of superheating and convective mixing effects on solidification and melting behavior.
- Model verification with different sizes and shapes of containers
- Model verification using a higher-temperature working fluid (higher N_{ph})
- Model verification using an alternative PCM

3. Inert Volume-Change Control Additives

- No further study recommended at this time for carbonates

4. Conduction Enhancement

- Further investigation of SS or aluminum in various forms, primarily wool or fixed-structure configurations
- Corrosion testing of promising materials in different carbonate mixtures

5. Containment

- Long-term corrosion testing of current containment materials in several salt mixtures under cycling conditions
- Identification and/or development of lower-cost containment materials
- Compatibility testing under thermal-cycling conditions of other candidate materials

6. Performance Testing

- Use of higher-temperature working fluids
- Alternate passive heat exchanger configurations (multiple type) to establish performance in a more "commercial" system design
- Larger-scale testing of systems designed from the heat-transfer model
- Long-term endurance testing (>10,000 hr)
- Long- and short-term testing with alternate PCM's
- Long- and short-term testing with most promising conductivity promoters

7. TES System Development

- System studies to determine design constraint to be placed on systems in various uses
- Cost and energy-saving analyses for promising concepts and economic feasibility

NOMENCLATURE

A = heat-transfer area, ft^2, in.^{2}

A_o = constant (Equation 14)

a = characteristic thickness, ft, in.
(half-thickness of a slab, radius of a cylinder or a sphere)

c_p = heat capacity, Btu/lbm-°F

D = differential operator $\equiv \frac{\partial}{\partial \tau} + v \frac{\partial}{\partial x}$

d = wall thickness, ft
tube diameter, ft, in.

f_s = volume fraction of container occupied by molten salt

G = mass velocity, lbm/hr-ft^2

g = acceleration due to gravity; $g = 9.807$ m/s^2

h = surface heat-transfer coefficient, Btu/hr-ft^2-°F

ΔH_f = heat of fusion, Btu/lbm

i = $\sqrt{-1}$

k = thermal conductivity, Btu/hr-ft-°F

K = wave number, ft^{-1}

L = significant dimension, ft

L_1 = pipe length to meet fixed volume requirement, ft

L_2 = pipe length to meet energy transfer requirement

M = dimensionless frequency; $M = \sqrt{\frac{\pi a^2 \nu}{\alpha}} = \sqrt{\frac{\pi}{N^0_{Fo}}}$

m = total mass, lbm

$\dot{m}$ = mass flow rate, lbm/hr

n = number of heat exchange pipes

N_{Fo} = Fourier number (dimensionless time); $N_{Fo} = \alpha\tau/a^2$

N^0_{Fo} = dimensionless period; $N^0_{Fo} = \alpha\tau_0/a^2$

N_{Nu} = Nusselt number (ratio of surface conductance to fluid conductance);
$N_{Nu} = ha/k_f$

ORIGINAL PAGE IS
OF POOR QUALITY

N_{ph} = phase-change number (ratio of heat of fusion to the sensible heat between the melting point and a reference temperature); $N_{ph} = \Delta H_f \rho_\ell / c_{ps}(t_m - t_a)\ \rho_s$

N_{Pr} = Prandtl number (ratio of kinematic viscosity to thermal diffusivity); $N_{Pr} = \nu/\alpha$

N_{Ra} = Rayleigh number (ratio of buoyant to thermal forces)

N_{Re} = Reynolds number (ratio of inertial to viscous forces); $N_{Re} = vd/\nu$

N_{Bi} = Biot number (ratio of surface conductance to interior solid conductance); $N_{Bi} = ha/k_s$ or Ua/k_s

p = perimeter, ft, in.

R = r/r_o, radius ratio

r = radial coordinate, ft

r* = radial integration variable

Q = quantity of heat, Btu

q = heat flux, Btu/hr-ft^2

t = temperature, °C, °F

Δt = temperature gradient, °C, °F

T = absolute temperature, °R

U = overall heat-transfer coefficient, Btu/hr-ft^2-°F

V = fluid volume, ft^3

v = velocity, ft/hr

X = moving length coordinate, ft

x = length coordinate, ft

z = longitudinal coordinate, direction of fluid flow, ft

Greek Letters

α = thermal diffusivity, ft^2/hr; $\alpha = k/c_p\rho$

β = coefficient of volume expansion, °R^{-1}; $\beta = (\rho_\infty - \rho)/\rho\Delta T$

δ = a finite difference operator

Δ = same as δ

NOMENCLATURE, Cont.

λ = wavelength, ft

μ = dynamic viscosity, lbf-hr/ft^2, cP

ν = kinematic viscosity, ft^2/hr
frequency, cps

ρ = density, lbm/ft^3

ρ_0 = density of PCM, lbm/ft^3

ρ_∞ = density of liquid salt far away from heat-transfer surface

τ = time

τ_0 = period

ω = circular frequency, rad/s; $\omega = 2\pi\nu$

Subscripts

a = ambient

c = container

app = apparent

f = fluid

in = initial

ins = insulation

ℓ = liquid (phase)

m = melting

s = solid (phase)

surf = surface

w = wall

Superscripts

$\dot{}$ = per unit time

$\bar{}$ = average quantity

REFERENCES CITED

1. Atomics International, "Development of a Molten Carbonate Process for Removal of Sulfur Dioxide From Power Plant Stack Gases," Progress Report No. 2 to U.S. Public Health Service Contract No. PH 86-67-128. Canoga Park, Calif., 1968.

2. Bramlette, T. T. et al., "Survey of High Temperature Thermal Energy Storage," SAND 75-8063. Livermore, Calif.: Sandia Laboratories, 1976.

3. Broers, G. H. J. and Van Ballegoy, H. J. J., "Phase Equilibria in Li-Na-K Carbonate-Aluminate Systems." Paper presented at the 3rd International Symposium on Fuel Cells, Brussels, June 1969.

4. Carslaw, H. S. and Jaeger, J. C., Conduction of Heat in Solids, 2nd Ed., 282-91. London: Oxford University Press, 1959.

5. Chandrasekhar, S., Hydrodynamic and Hydromagnetic Stability. London: Oxford University Press, 1961.

6. Davis, H. J. and Kinnibrugh, D. R., "Passivation Phenomena and Potentiostatic Corrosion in Molten Alkali Metal Carbonates," J. Electrochem. Soc. 117 (3), 392-96 (1970).

7. Grantham, L. F. and Ferry, P. B., "Corrosion in Alkali Carbonate Based Melts," Abstract No. 391 in Extended Abstracts, Vol. 76-1, for the 149th Meeting of the Electrochemical Society, Washington, D.C., May 2-7, 1976.

8. Groeber, H., Forschungsarb, Heft 300, V.D.I., Berlin, 1928.

9. Hatch, J. E. et al., "Graphical Presentation of Difference Solutions for Transient Radial Heat Conduction in Hollow Cylinders with Heat Transfer at the Inner Radius and Finite Slabs with Heat Transfer at One Boundary," NASA TR R-56, 34, 1960.

10. Hausz, W. and Meyer, C. F., "Energy Conservation: Is the Heat Storage Well the Key?" Public Utilities Fortnightly, 34-38 (1975) April 24.

11. Hill, J., Streed, E., Kelly, G., Geist, J. and Kusuda, T., "Development of Proposed Standards for Testing Solar Collectors and Thermal Storage Devices," NBS Technical Note 899. Washington, D.C.: U.S. Department of Commerce/ National Bureau of Standards, February 1976.

12. Institute of Gas Technology, "Development of Molten Carbonate Fuel Cells," Final Report, A.G.A. Project DC-4-1. Chicago, 1967.

13. Janz, G. J., Lorenz, M. R., "Solid-Liquid Phase Equilibria for Mixtures of Lithium, Sodium, and Potassium Carbonates," J. Chem. Eng. Data 6 (3), 321-23 (1961) July.

14. Janz, G. J. and Conte, A., "Corrosion of Gold-Palladium, Nickel and Type-347 Stainless Steel in Molten Alkali Carbonates," Corrosion 20, 237t-238t (1964).

REFERENCES CITED, Cont.

15. Janz, G. J. and Conte, A., "Potentiostatic Polarization Studies in Fused Carbonates, II. Stainless Steel," Electrochim Acta 9, 1279-87 (1964).

16. Kardas, A., "On a Problem in the Theory of the Unidirectional Regenerator," Int. J. Heat Mass Transfer 9, 567-79 (1966).

17. Kreith, F., Principles of Heat Transfer, 347. Scranton, Pa.: Intern. Textbook Co., 1959.

18. Maru, H. C., Dullea, J. F. and Huang, V. M., "Molten Salt Thermal Energy Storage Systems: Salt Selection," Topical Report, ERDA Contract No. E(11-1)-2888. Chicago: Institute of Gas Technology, August 1976.

19. Maru, H. C. et al., "Fuel Cell Research on Second-Generation Molten Carbonate Systems, Vol. II: Characteristics of Carbonate Melts," Quarterly Progress Report, Argonne National Laboratory Contract No. 31-109-38-3552. Chicago: Institute of Gas Technology, July 1-September 30, 1976.

20. Maru, H. C., Kardas, A., Huang, V. M., Dullea, J. F., Paul, L. and Marianowski, L. G., "Molten Salt Thermal Energy Storage Systems: System Design," Topical Report, ERDA Contract No. EY-76-C-02-2888. Chicago: Institute of Gas Technology, February, 1977.

21. Mason, D. M. and Van Drunen, C. J., "Production of Beta-Lithium Aluminate," U.S. Patent 3,998,939 (1976) December 21.

22. Megerlin, F., "Geometrically One-Dimensional Heat Conduction During Melting and Solidification," Forsch. Ingenieurwes. 34 (2), 40-46 (1968) (German text).

23. Meijer, R. J. and Spigt, C. L., "The Potential of the Phillips Stirling Engine for Pollution Reduction and Energy Conservation." Paper presented at the 2nd Symposium on Low Pollution Power Systems Development, Organized by the Committee on the Challenges of Modern Society, NATO, Dusseldorf, Germany, November 4-8, 1974.

24. Schroder, J., "Thermal Energy Storage and Control." Paper No. 74-WA/OTD-1, presented at the 95th Winter Annual Meeting of the American Society of Mechanical Engineers, New York, November 17-22, 1974.

25. Siegel, R., "Solidification of Low Conductivity Material Containing Dispersed High Conductivity Particles," Int. J. Heat Mass Transfer 20, 1087-89, 1977.

26. Spedding, P. L., "Densities and Molar Volumes of Molten Alkali Carbonate Binary Mixtures," J. Electrochem. Soc. 117 (2), 177-83 (1970) February.

LS/DG